Evolution of single-particle states outside $N = 126$ using the ^{212}Rn$(d,p)^{213}$Rn reaction in inverse kinematics

A thesis submitted to The University of Manchester for the degree of Doctor of Philosophy in the Faculty of Science and Engineering

2024

Daniel J. Clarke

Department of Physics and Astronomy in the School of Natural Sciences

Blank page

Contents

List of figures 9

List of tables 11

Abbreviations 14

Abstract 15

Declaration of authorship 17

Copyright statement 19

Acknowledgements 21

1 Evolution of single-particle states and shell structure in nuclei 23
1.1 The nuclear shell model . . . 24
1.1.1 Mean-field potential . . . 24
1.1.2 Residual interactions and configuration mixing . . . 27
1.2 Shell evolution . . . 30
1.2.1 Monopole shift . . . 31
1.2.2 Tensor interaction . . . 32
1.2.3 Light and medium mass neutron-rich systems . . . 33
1.2.4 Trends in heavier stable nuclei . . . 36
1.3 Aims of this work . . . 40

2 Probes of single-particle structure 45
2.1 Reaction mechanisms . . . 45
2.1.1 Reaction cross sections . . . 47
2.1.2 Theory of single-nucleon transfer reactions . . . 47
2.1.3 The DWBA . . . 49
2.2 Modelling a transfer reaction . . . 52
2.2.1 Optical model . . . 52
2.2.2 Bound-state parameters . . . 53

2.3 Spectroscopic information . . . 54
2.3.1 Sum rules . . . 55
2.3.2 Energy centroids . . . 56

3 The $d(^{212}\mathrm{Rn},p)^{213}\mathrm{Rn}$ reaction at ISOLDE 57
3.1 The ISOLDE RIB facility . . . 57
3.1.1 Isotope production . . . 58
3.1.2 Element selection . . . 59
3.1.3 Post acceleration . . . 59
3.1.4 Beam properties . . . 63
3.1.5 Timing . . . 63
3.2 Transfer reaction kinematics . . . 66
3.2.1 Relativistic effects . . . 67
3.2.2 Two-body kinematics . . . 68
3.2.3 Challenges in inverse kinematics for a (d,p) reaction . . . 71
3.2.4 Transfer reactions in a solenoid . . . 74
3.2.5 Finite size of the array . . . 77
3.3 ISS . . . 80
3.3.1 On-axis Si array . . . 80
3.3.2 Downstream detectors . . . 83
3.3.3 Detector positions . . . 85
3.3.4 Electronics . . . 86
3.3.5 Targets . . . 88

4 Analysis of data from the $d(^{212}\mathrm{Rn},p)^{213}\mathrm{Rn}$ reaction 91
4.1 Detector calibration . . . 91
4.1.1 Array calibration . . . 92
4.1.2 Luminosity detector calibration . . . 94
4.2 Timing conditions . . . 94
4.2.1 Coincidence time window for p sides and n sides . . . 95
4.2.2 Background subtraction . . . 96
4.3 Excitation energies . . . 97
4.3.1 Beam-energy losses . . . 99
4.3.2 Pulse-height corrections . . . 99
4.3.3 Iterative calculations . . . 100
4.3.4 Additional cuts . . . 103
4.3.5 Uncertainties in centroids of excited states . . . 104
4.3.6 Contributions to excitation energy resolution . . . 107
4.4 Cross sections . . . 108

4.4.1 Absolute normalisation using the luminosity detector 109
4.4.2 Pile-up corrections 111
4.4.3 Geometric efficiency corrections 116
4.4.4 Solid angles 119
4.5 Angular momentum assignments and spectroscopic factors 119
4.5.1 Comparing optical models 120
4.5.2 Dependency of absolute spectroscopic factors on optical-model parameters 122
4.5.3 States in ^{213}Rn 124

5 Discussion 131
5.1 Uncertainties in spectroscopic factors 131
5.2 Spectroscopic factors of $\nu 2g_{9/2}$ and $\nu 1i_{11/2}$ orbitals along $N = 126$. 132
5.2.1 Two-body matrix element calculations 134
5.3 Comparison to shell-model calculations 135
5.4 Future work and outlook 138

A Table of cross sections 141

Bibliography 147

Blank page

List of figures

1.1 Examples of different mean-field potentials . . . 26
1.2 Orbitals in the shell model using a harmonic oscillator potential and a Woods-Saxon potential . . . 28
1.3 A schematic showing an example of the choice of model space used in shell-model calculations . . . 31
1.4 Schematic showing the tensor interactions . . . 34
1.5 Neutron separation energies at different neutron numbers and proton excesses . . . 35
1.6 First-excited 2^+ states in C, O, Ne and Mg isotopes . . . 35
1.7 Energies of first-excited 2^+ in Ca isotopes and along the $N = 30$, 32 and 34 isotonic chains . . . 36
1.8 Experimental data showing the binding energy of the lowest lying $7/2^+$ and $11/2^-$ states in Sb isotopes . . . 38
1.9 Experimental data showing neutron occupancies in $^{112-124}$Sn . . . 39
1.10 Experimental data showing the energy difference between $\nu 1i_{13/2}$ and $\nu 1h_{9/2}$ orbitals for $N = 83$ nuclei . . . 39
1.11 Experimental data showing proton occupancies across $N = 50$ isotopes and energy differences between $\nu 1g_{9/2}$ and $\nu 4s_{1/2}$ centroids for $N = 51$ nuclei . . . 40
1.12 Reduced radial wave functions and probability densities for orbitals for an $A = 213$ nucleus . . . 41
1.13 Relative spectroscopic factors for states in ^{207}Hg, ^{209}Pb and ^{211}Po . . . 43

2.1 An illustration of a (d,p) direct transfer reaction. . . . 49
2.2 Components of the optical potential for the $d(^{212}\text{Rn},d)^{212}\text{Rn}$ reaction at 7.63 MeV/u. . . . 54

3.1 Schematic of the ISOLDE facility layout . . . 58
3.2 In-target production yields per µC of proton beam for elements in the mass region around ^{212}Rn . . . 60
3.3 Drawing of REX-ISOLDE, the HIE-ISOLDE superconducting LINAC and ISS in ISODE . . . 61

3.4 A schematic of REX-ISOLDE . . . 62
3.5 A schematic showing how REXTRAP accumulates, bunches and cools ion beams . . . 62
3.6 Integrated cross section as a function of incident beam energy for the ^{212}Rn(d,p)^{213}Rn reaction . . . 64
3.7 Angular distributions of different angular momentum transfers in the ^{212}Rn(d,p)^{213}Rn reaction at different beam energies . . . 64
3.8 Schematic of the timing of different components at ISOLDE . . . 65
3.9 Diagram of a fixed-target transfer reaction in the CM frame and lab frame . . . 69
3.10 Transformations of angles between the lab frame and CM frame . . . 72
3.11 Kinematic compression and kinematic shift of inverse kinematics compared to normal kinematics . . . 73
3.12 The trajectory of a proton in ISS . . . 75
3.13 Kinematic lines from the d(^{212}Rn,p)^{213}Rn reaction for a proton populating different excited states . . . 77
3.14 The trajectory of a proton with a finite sized detector in ISS . . . 78
3.15 Kinematic lines for detectors with different detector radii . . . 79
3.16 The layout of elements in ISS . . . 81
3.17 A map of axial and radial magnetic field strengths in ISS . . . 82
3.18 A photograph taken from the downstream end of the on-axis Si array . 84
3.19 Cross-sectional schematic of the on-axis Si array. . . . 85
3.20 Images of the luminosity detector . . . 86
3.21 Schematic of detectors and example trajectories . . . 87
3.22 A block diagram of signal processing in an ASIC . . . 88
3.23 Diagram of data acquisition parameters for the luminosity monitor . . 88
3.24 A photograph of target ladder used to hold CD_2 targets . . . 90

4.1 α particle data used to calibrate a p-side channel in the Si array . . . 93
4.2 Calibrated p-side channels of α particle data at two distances from the target . . . 93
4.3 α particle data used to calibrate the luminosity detector . . . 94
4.4 Time difference between p-side and n-side channels as a function of p-side energy for data from the Si array . . . 95
4.5 Measured proton energy against z with p-side and n-side timing cuts . 96
4.6 Counts in the luminosity detector as a function of time from the EBIS trigger signal for fast extraction and slow extraction . . . 97
4.7 EBIS time window background subtractions . . . 98
4.8 The energy loss of ^{212}Rn in CD_2 . . . 99

4.9 Pulse-height correction calculations for protons and α particles 101
4.10 Proton energy loss in CD_2 as a function of proton energy and θ_{lab} . . . 102
4.11 Proton energy loss in the Al as a function of proton energy and θ_{lab} . . 103
4.12 Data from the Si array that have been transformed to show the excitation energy of ^{213}Rn as a function of z with z and θ_{cm} cuts applied. . 104
4.13 Excitation energy spectrum of ^{213}Rn with and without cuts 105
4.14 The difference of ground state centroids using different parameter values in excitation energy calculations 106
4.15 Excitation energy spectrum of ^{213}Rn fitted with Gaussian peaks and a linear background 108
4.16 The FWHM of the ground state at different distances from the target . 109
4.17 Energy spectrum using data from the luminosity detector 111
4.18 Elastic scattering calculations 112
4.19 Energy spectra in the luminosity detector gated on different EBIS beam-on time windows. 114
4.20 Observed rate in the luminosity detector for fast and slow extraction . 116
4.21 A map showing disabled channels in Module 1 for each sub-run during the experiment 117
4.22 Angular distributions using different combinations of optical-model parameter sets for the ground state in ^{213}Rn 122
4.23 Experimentally measured angular distributions of states observed in ^{209}Pb fitted to DWBA calculations 123
4.24 Comparison of absolute SFs for states in ^{213}Rn using different optical-model parameter sets 124
4.25 Comparison of relative SFs for states in ^{213}Rn using different optical-model parameter sets 125
4.26 Angular distributions of states observed in ^{213}Rn 127

5.1 Calculations of the difference binding energies for $\nu 2g_{9/2}$ and $\nu 1i_{11/2}$ orbitals compared to experimental data of energy differences of the ground state and the lowest-lying $\ell = 6$ state in $N = 127$ isotones . . . 135
5.2 Experimental spectroscopic factors compared to shell model calculations 137

Blank page

List of tables

3.1 Radial distances from the beam axis for n-side strips 83
3.2 Relevant distances and detector dimensions of the luminosity monitor . 84
3.3 Data acquisition parameter settings for the luminosity detector 89

4.1 Table of α-particle energies used to calibrate detectors 92
4.2 Optical-model parameters used to calculate elastic scattering cross sections of deuterons on ^{212}Rn at 7.63 MeV/u 113
4.3 Efficiencies of ASICs in each module due to disabled channels 118
4.4 Optical model parameters for ground state cross section calculations in the $d(^{212}\mathrm{Rn},p)^{213}\mathrm{Rn}$ reaction at 7.63 MeV/u 121
4.5 The variation of absolute and relative SFs for strong states in ^{213}Rn that could be assigned an ℓ-transfer 124
4.6 States in ^{213}Rn populated in the $d(^{212}\mathrm{Rn},p)^{213}\mathrm{Rn}$ reactions at 7.63 MeV/u 126
4.7 Comparison of excitation energies and angular momentum assignments to states observed in the EC/β^+ decay of ^{213}Fr 129

5.1 Absolute spectroscopic factors of the ground state and the observed lowest-lying $\ell - 6$ state in ^{209}Pb using data from a range of studies . . 133
5.2 Excitation energies, spectroscopic factors and excitation energy centroids for $\nu 2g_{9/2}$ and $\nu 1i_{11/2}$ states from shell-model calculations 136

A.1 Cross sections measured from the $d(^{212}\mathrm{Rn},p)^{213}\mathrm{Rn}$ reaction at 7.63 MeV/u 145

Blank page

Abbreviations

ADC **A**nalogue-to-**D**igital **C**onverter

ASIC **A**pplication-**S**pecific **I**ntegrated **C**ircuit

CERN European Organisation for Nuclear Research

CM **C**entre of **M**omentum

DAQ **DA**ta ac**Q**uisition

DWBA **D**istorted-**W**ave **B**orn **A**pproximation

EBIS **E**lectron **B**eam **I**on **S**ource

ESPE **E**ffective **S**ingle-**P**article **E**nergy

FWHM **F**ull **W**idth at **H**alf **M**aximum

GPS **G**eneral **P**urpose **S**eparator

GSI GSI Helmholtz Centre for Heavy Ion Research

HIE-ISOLDE **H**igh **I**ntensity and **E**nergy-**ISOLDE**

IH **I**nterdigital **H**-type

IPM **I**ndependent-**P**article **M**odel

ISOL **I**sotope **S**eparator **O**n**L**ine

ISOLDE **I**sotope **S**eparator **O**n**L**ine **DE**vice

ISS **I**SOLDE **S**olenoidal **S**pectrometer

LINAC **LIN**ear **AC**celerator

PHC **P**ulse **H**eight **C**orrection

PSB **P**roton **S**ynchrotron **B**ooster

REX-ISOLDE **R**adioactive beam **EX**periment at **ISOLDE**

RFQ **R**adio-**F**requency **Q**uadrupole

RIB **R**adioactive **I**on **B**eam

RMS **R**oot **M**ean **S**quare

SD **S**tandard **D**eviation

SRIM **S**tooping and **R**ange of **I**ons in **M**atter

VADIS **V**ersatile **A**rc **D**ischarge **I**on **S**ource

Abstract

Single-particle states in ^{213}Rn were populated using the ^{212}Rn$(d,p)^{213}$Rn reaction in inverse kinematics. The experiment was performed at the ISOLDE facility where a ^{212}Rn beam was accelerated up to 7.63 MeV/u and directed at CD_2 targets in the ISOLDE solenoidal spectrometer. Cross sections and energies of excited states up to 4 MeV were measured from excitation energy spectra and compared to optical-model calculations using the DWBA code, PTOLEMY. From this, spectroscopic factors were extracted, and assignments were made of the angular momentum transferred to states.

Two-body matrix element calculations have been compared to the effective single-particle energies of $\nu 2g_{9/2}$ and $\nu 1i_{11/2}$ orbitals, indicating that the inclusion of a tensor component is important when describing the evolution of orbitals along the isotonic chain—assuming protons only fill the $\pi 1h_{9/2}$ orbital. Additionally, comparisons of energies and spectroscopic factors of states with shell-model calculations show a broad agreement with experimental data up to approximately 2.5 MeV. The findings from this experiment contribute valuable insights to the understanding of the evolution of shell structure along the $N = 127$ isotonic.

Blank page

Declaration of authorship

I, Daniel J. Clarke, confirm that no portion of the work referred to in this thesis has been submitted in support of an application for another degree or qualification of this or any other university or other institute of learning.

Blank page

Copyright statement

i. The author of this thesis (including any appendices and/or schedules to this thesis) owns certain copyright or related rights in it (the "Copyright") and they have given the University of Manchester certain rights to use such Copyright, including for administrative purposes.

ii. Copies of this thesis, either in full or in extracts and whether in hard or electronic copy, may be made only in accordance with the Copyright, Designs and Patents Act 1988 (as amended) and regulations issued under it or, where appropriate, in accordance with licensing agreements which the University has from time to time. This page must form part of any such copies made.

iii. The ownership of certain Copyright, patents, designs, trademarks and other intellectual property (the "Intellectual Property") and any reproductions of copyright works in the thesis, for example graphs and tables ("Reproductions"), which may be described in this thesis, may not be owned by the author and may be owned by third parties. Such Intellectual Property and Reproductions cannot and must not be made available for use without the prior written permission of the owner(s) of the relevant Intellectual Property and/or Reproductions.

iv. Further information on the conditions under which disclosure, publication and commercialisation of this thesis, the Copyright and any Intellectual Property and/or Reproductions described in it may take place is available in the University IP Policy (see https://documents.manchester.ac.uk/DocuInfo.aspx?DocID=24420) in any relevant Thesis restriction declarations deposited in the University Library, the University Library's regulations (see https://www.library.manchester.ac.uk/about/regulations/) and in the University's policy on Presentation of Theses.

Blank page

Acknowledgements

This work reflects a journey of eight years of study at The University of Manchester. So many people have helped and supported me along the way, and I apologise if I have missed anyone out.

First, I would like to thank my supervisors David Sharp and Sean Freeman, whose patience and guidance have been invaluable to me during my PhD. Despite juggling an incredible number of responsibilities, you have both always found the time to listen and offer advice, for which I am very thankful. Special thanks to Sean for all the feedback given during the writing up process, and to David for introducing me to the legendary 'homemade' limoncello at *La Meyrinoise*.

A massive thanks must also go to Liam Gaffney, who dedicated countless hours at ISOLDE explaining the weird and wonderful inner workings of ISS to me during my LTA. I learnt so much over this period and likely would have broken far more things along the way without your expertise and guidance!

My time at CERN was made all the more enjoyable by the company of Frank Browne, whose presence brought a great deal of laughter to both the lab and our many evenings spent at LA Taproom with Sean. I would also like to thank Annie Dolan for all the help and support in the lab at ISOLDE. I wish you every success in the future with the work you go on to do in Liverpool.

Thank you to everyone in the nuclear group in Manchester. I thoroughly enjoyed the time spent on experiments with Sam Reeve and Katie Garrett, even if we occasionally found ourselves in states of delirium from lack of sleep. Special thanks to Matt and Alex as well. I hope we managed to help keep each other somewhat sane during our arduous writing up periods. I am also grateful to Sam Bennett

for his initial guidance at the beginning of my PhD.

Outside the world of nuclear physics, so many people have offered me immense support, and without them, this thesis would not have been possible. Thank you to Reagan, Amy and Alex for your friendship over the years and for coming out to visit me in Geneva. I am grateful to Joanna and Oli for keeping me fed and watered during the writing up process—I am slowly repaying my Guinness debt. Thanks also to all of Tegan's friends including Hobbs, Tom, Amy and, of course, Sidney. It has been lovely getting to know you all over the past few years.

To Tegan—you have been there for me throughout my PhD, showing endless understanding and support through all the challenges it has thrown at me. You have done so much, especially over the last six months during this tough writing-up period, and I am sure you will be as happy as I am to finally see the back of this thesis. I hope you had as much fun as I did exploring Geneva and Switzerland together. I will always cherish the time we spent in the mountains—Shred it!

Finally, and most importantly, I would like to thank my mum, dad and brother who have been there throughout all the ups and downs over the last four years. None of this would have been possible without your constant love and support, and I am very grateful for everything you have done for me.

Chapter 1

Evolution of single-particle states and shell structure in nuclei

Nuclei are quantum systems composed of protons and neutrons. In principle, if the form of interactions between nucleons is known, properties of nuclei should be able to be predicted using quantum mechanics. However, unlike atomic systems, the force between nucleons is complex in nature and requires modification when the two nucleons are surrounded by other nuclear matter. On top of this, most nuclei contain too few components to accurately apply statistical methods to predict their properties, but sufficiently many that including all interactions between nucleons becomes impractical computationally for all but the simplest nuclei. By replacing the combined effect of all nucleon-nucleon interactions with an average field, shell structure can be seen to emerge in nuclei from the motion of single particles in the associated potential. This interpretation has provided information helping to explain and predict experimental observables of stable nuclei with magic numbers of neutrons or protons, N or Z = 2, 8, 20, 28, 50, 82 and 126, such as discontinuities in binding energies and the values of first-excited 2^+ states. However, it is not clear if these models predict the behaviour of exotic nuclei, and there is experimental evidence that points towards shell structure evolving in nuclei away from stability [1].

In this chapter, the theoretical framework of the independent-particle model (IPM) and emergence of shell structure is discussed. Experimental evidence highlighting the evolution of shell structure across will be given along with theoretical inter-

pretations of this behaviour due to nucleon-nucleon interactions. Shell structure in the region around $N = 126$ will also be summarised, forming the motivation of this work.

1.1 The nuclear shell model

In the nuclear shell model, nucleons are assumed to move independently of each other and are subject to a central average potential created by all nucleons. With the addition of a spin-orbit term to the potential, independently by Mayer [2, 3] and Haxel, Jensen and Suess [4], this model was used to predict magic numbers for stable nuclei across the nuclear chart.

1.1.1 Mean-field potential

The total Hamiltonian, $\widehat{H}$, for a nucleus of A nucleons is described by

$$\widehat{H} = \sum_{i}^{A} \widehat{H}_i, \tag{1.1}$$

where $\widehat{H}_i$ is the Hamiltonian for each nucleon. Restricting the system to include only two-body nucleon-nucleon interactions, the total Hamiltonian for each nucleon can be written as

$$\widehat{H}_i = T_i(\mathbf{r}_i) + \sum_{i \neq j} V_{ij}(\mathbf{r}_i, \mathbf{r}_j), \tag{1.2}$$

where T is the kinetic energy operator and V is the potential function describing nucleon-nucleon interactions. The premise of the model is that the potential of two-body nucleon-nucleon interactions can be replaced by a central average potential created by the interactions of all nucleons, $U(r_i)$, with the nucleon of interest that only depends on its position, r_i. This can be incorporated into the Hamiltonian of each nucleon as

$$\widehat{H}_i = \underbrace{T_i(\mathbf{r}_i) + U(r_i)}_{\widehat{H}_i^{(0)}} + \underbrace{\sum_{i \neq j} V_{ij}(\mathbf{r}_i, \mathbf{r}_j) - U(r_i)}_{\widehat{H}_i^{\text{res}}}, \tag{1.3}$$

where $\widehat{H}_i^{\text{res}}$ corresponds to residual interactions and represents the part of the overall potential not described by the central potential. If the choice of $U(\mathrm{r}_i)$ is good, one might expect that the effect of $\widehat{H}_i^{\text{res}}$ might be small.

The single-particle wave functions, $\phi_1(\mathbf{r}_1), \phi_2(\mathbf{r}_2), \ldots, \phi_A(\mathbf{r}_A)$, are solutions to the Schrödinger equation,

$$\widehat{H}_i^{(0)}\phi_i = \varepsilon_i\phi_i, \tag{1.4}$$

with eigenvalues $\varepsilon_1, \varepsilon_2, \ldots, \varepsilon_A$. Nucleons fill degenerate states in orbitals starting with the lowest energy orbital following the Pauli exclusion principle and each orbital has a radial quantum number, n, orbital angular momentum, ℓ, and total angular momentum, j. Degeneracies determine the maximum occupancy of the orbital. A product wave function of the nucleus, such as

$$\Psi = \prod_i^A \phi_i(\mathbf{r}_i), \tag{1.5}$$

is a solution of Equation 1.4 with eigenvalues

$$E^{(0)} = \sum_i^A \varepsilon_i, \tag{1.6}$$

where $E^{(0)}$ is the total energy of the nucleus. However, as the system is fermionic, the wave function must be described using a Slater determinant,

$$\Psi = \frac{1}{\sqrt{A!}} \begin{vmatrix} \phi_1(\mathbf{r}_1) & \phi_1(\mathbf{r}_2) & \cdots & \phi_1(\mathbf{r}_A) \\ \phi_2(\mathbf{r}_1) & \phi_2(\mathbf{r}_2) & \cdots & \phi_2(\mathbf{r}_A) \\ \vdots & \vdots & \ddots & \vdots \\ \phi_A(\mathbf{r}_1) & \phi_A(\mathbf{r}_2) & \cdots & \phi_A(\mathbf{r}_A) \end{vmatrix}, \tag{1.7}$$

to satisfy antisymmetrisation under exchange of nucleons [5].

Different phenomenological potentials can be chosen that are consistent with a short-ranged attractive nucleon-nucleon force and a very simple starting point is an infinite square-well potential, shown in Figure 1.1. Solutions to the Schrödinger equation using this potential lead to a degeneracy of each orbital characterised by the orbital angular momentum of $2(2\ell+1)$. Although the potential does not have realistic properties due to discontinuities forcing all states to be bound, it does correctly predict the magic numbers of 2, 8 and 20. A harmonic oscillator potential, also shown in Figure 1.1, has the advantage of being a continuous function and has analytical solutions. Due to this, harmonic oscillator functions are used

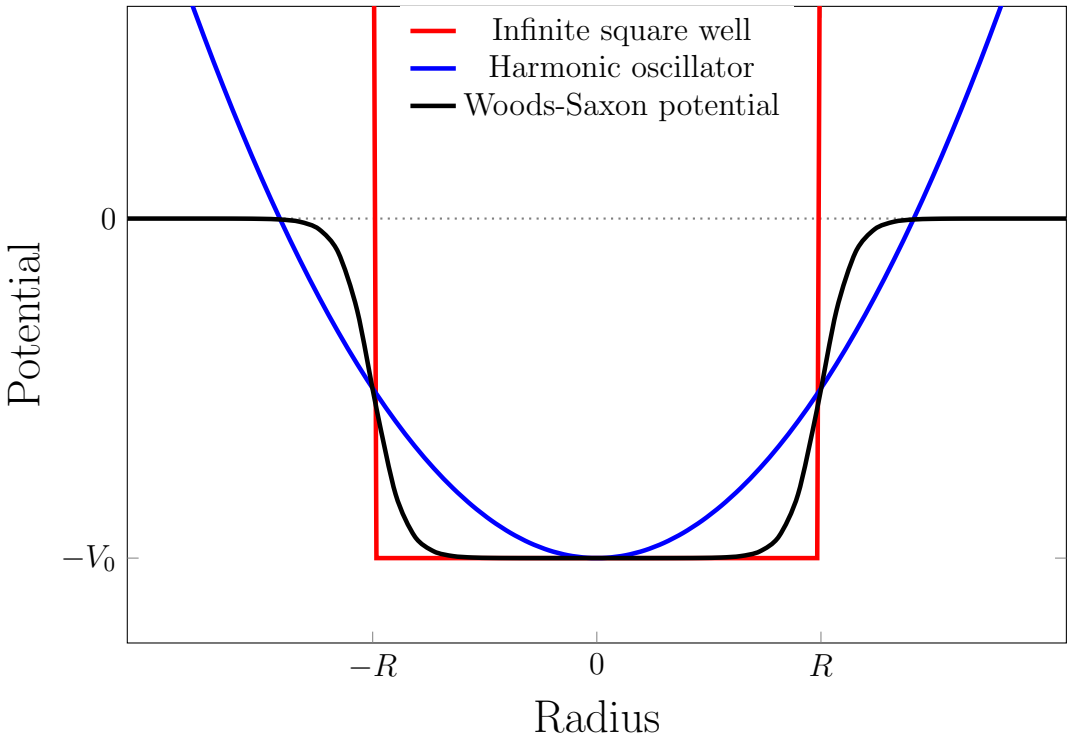


Figure 1.1: Examples of different mean-field potentials. The terms R and V_0 represent the nuclear radius and potential depth, respectively.

to describe the basis set in full shell-model calculations for computational convenience. However, it does not possess the correct asymptotic behaviour, tending to infinity as the radial distance increases. Despite this, solutions also predict the magic numbers of 2, 8 and 20 but not those above this. Shell closures arising from this potential are shown in Figure 1.2. A more realistic and commonly used function is the Woods-Saxon potential [6], shown in Figure 1.1. This has the correct asymptotic behaviour and can be thought of as lying somewhere in between the two previous potentials. The potential has the form

$$U_{\mathrm{ws}}(\mathrm{r}) = \frac{-V_0}{1 + \mathrm{e}^{\left(\frac{r-R}{a}\right)}}, \tag{1.8}$$

where V_0 is the potential depth, with a typical value of approximately 50 MeV, $R = r_0 A^{\frac{1}{3}}$ with $r_0 \approx 1.25$ fm, and a is a diffuseness parameter, usually taken to be ~ 0.5 fm. When solving the Schrödinger equation using the Woods-Saxon potential, exact analytical solutions only exist for states with an orbital angular momentum of $\ell = 0$ [7] and numerical methods need to be employed for $\ell \neq 0$. Even with its more realistic form, shell closures of N or $Z = 2$, 8, 20, 40, 58, 92 and 112 are found, deviating from experimental observations above 20 [5, 8, 9, 10].

The disagreement between theory and experiment was resolved by the inclusion of a spin-orbit term in the potential. This arises from the coupling of the orbital angular momentum of nucleons, ℓ, with their intrinsic spin, s, contributing to an additional term in the nuclear Hamiltonian:

$$U_{\rm so}(r) = -V_{\rm so}\frac{1}{r}\frac{\partial U(r)}{\partial r}\boldsymbol{\ell}\cdot\boldsymbol{s}, \tag{1.9}$$

where $U(r)$ is the central potential. This has the effect of splitting states, other than those with $\ell = 0$, into two levels with total angular momenta $j = \ell \pm \frac{1}{2}$. Evaluating the expectation value of the dot product in Equation 1.9 gives

$$\langle\boldsymbol{\ell}\cdot\boldsymbol{s}\rangle = \frac{1}{2}\left[j(j+1) - \ell(\ell+1) - s(s+1)\right]\hbar^2. \tag{1.10}$$

The choice of a negative sign in Equation 1.8 means that, for a given pair, the $j = l + \frac{1}{2}$ state is more attractive and lowered in energy compared to the $j = l - \frac{1}{2}$ state, consistent with experimental findings. Additionally, the separation in energy of a pair of states is related to difference in expectation values given by

$$\langle\boldsymbol{\ell}\cdot\boldsymbol{s}\rangle_{\ell+1/2} - \langle\boldsymbol{\ell}\cdot\boldsymbol{s}\rangle_{\ell-1/2} = \frac{1}{2}(2\ell+1)\hbar^2, \tag{1.11}$$

showing that the energy difference between spin-orbit partners increases with orbital angular momentum [5, 8]. For high-j orbitals, the spin-orbit splitting is sufficiently large to alter the shell gaps arising in the single-particle potential (see Figure 1.2) which then reproduces the magic numbers observed near stability.

Even with the inclusion of spin-orbit coupling, there are major deficiencies in the predictions of the IPM. These arise because the effect of residual interactions is practically always too large to ignore. The next section described how their effects can be incorporated.

1.1.2 Residual interactions and configuration mixing

Although the IPM model is persuasive in its simplicity, beyond the prediction of ground-state spins and parities in nuclei close to doubly-magic systems, it fails to reproduce details of nuclear structure since the mean-field approximation is poor. Residual interactions invariably play a role and mix independent-particle configurations into more complex wave function. Residual nucleon interactions can be incorporated by using matrix diagonalisation and expressing a state of the

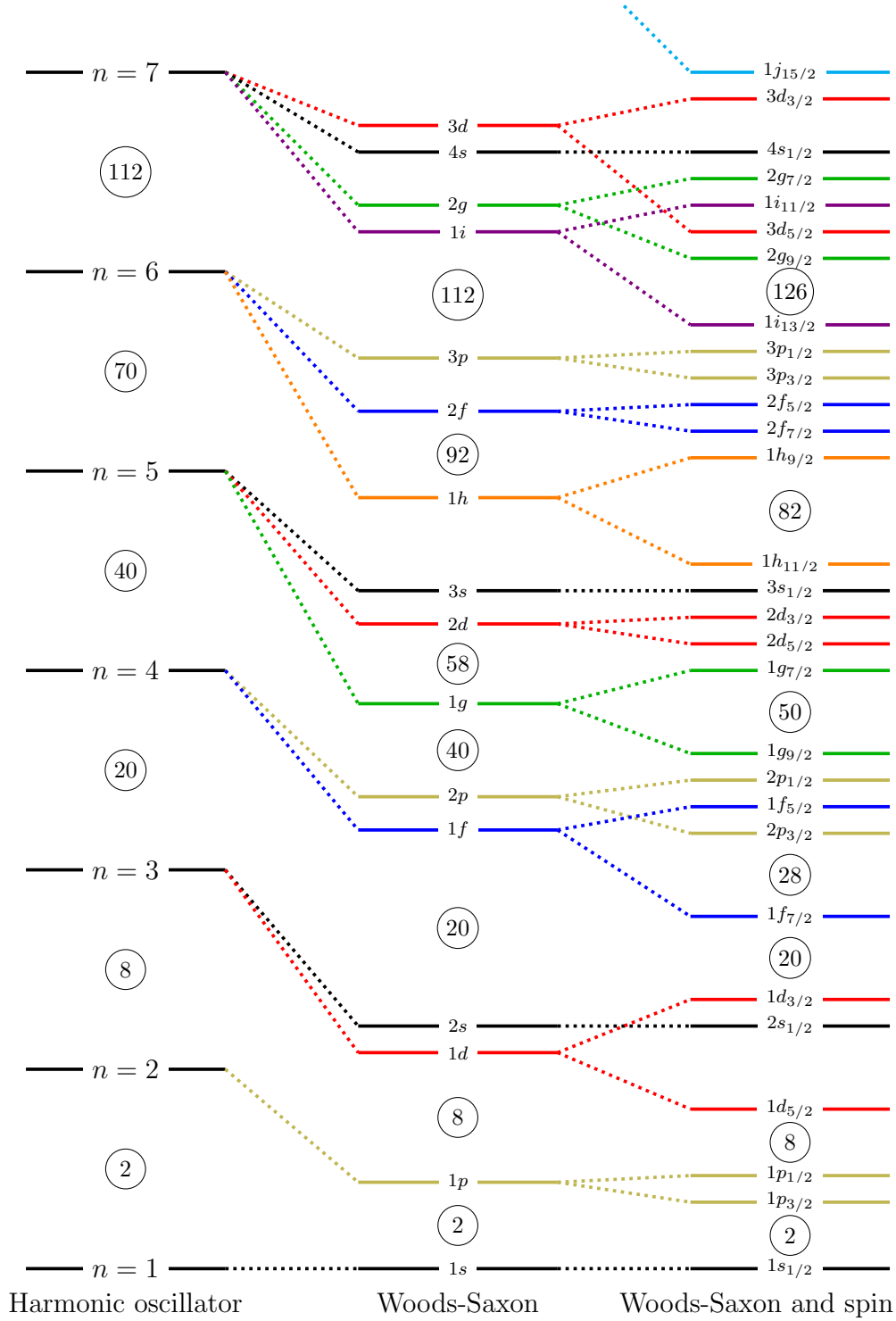


Figure 1.2: Orbitals and magic numbers in the nuclear shell model using a harmonic oscillator potential, a Woods-Saxon potential and a Woods-Saxon potential with a spin-orbit term. Adapted from Reference [11].

nucleus, Ψ_i, as a wave function formed by a sum of terms from a basis set of N IPM configurations through

$$\Psi_i = \sum_k^N a_{ki}\Phi_k, \tag{1.12}$$

where a_{ki} are expansion coefficients related to the probability of finding the nucleus in each configuration of nucleons, Φ_k. Each of these configurations are eigenstates of $\widehat{H}^{(0)}$ from the total nuclear Hamiltonian and expansion coefficients are normalised so that

$$\sum_k^N a_{ki}^* a_{ki} = 1. \tag{1.13}$$

If $\widehat{H}^{\text{res}}$ of the total Hamiltonian were small, the sum would be dominated by one of the expansion coefficient terms, forming pure states. Inserting Equation 1.12 into the Schrödinger equation and using the total Hamiltonian of the nucleus gives

$$(\widehat{H}^{(0)} + \widehat{H}^{\text{res}}) \sum_k^N a_{ki}\Phi_k = E_i \sum_k^N a_{ki}\Phi_k, \tag{1.14}$$

where the energy of the nucleus, E_i, can take on different values when measured. When projecting onto a particular configuration of nucleons, Φ_m, this becomes

$$\begin{aligned} \sum_k^N a_{ki} \underbrace{\langle\Phi_m|(\widehat{H}^{(0)} + \widehat{H}^{\text{res}})|\Phi_k\rangle}_{H_{km}} &= \sum_k^N a_{ki} \left[E_k^{(0)}\delta_{km} + \langle\Phi_m|\widehat{H}^{\text{res}}|\Phi_k\rangle\right] \\ &= E_i \sum_k^N a_{ki}\delta_{km} = E_i a_{mi}, \end{aligned} \tag{1.15}$$

where $E_k^{(0)}$ are energies of the nucleus from non-interacting shell-model calculations, and the degree of mixing between configurations is determined by the magnitude of $\langle\Phi_m|\widehat{H}^{\text{res}}|\Phi_k\rangle$. This can be written as a matrix equation, where H_{km} are matrix elements:

$$\begin{bmatrix} H_{11} & H_{12} & \cdots & H_{1N} \\ H_{21} & H_{22} & \cdots & H_{2N} \\ \vdots & \vdots & \ddots & \vdots \\ H_{N1} & H_{N2} & \cdots & H_{NN} \end{bmatrix} \begin{bmatrix} a_{1i} \\ a_{2i} \\ \vdots \\ a_{Ni} \end{bmatrix} = E_i \begin{bmatrix} a_{1i} \\ a_{2i} \\ \vdots \\ a_{Ni} \end{bmatrix}. \tag{1.16}$$

Values of expansion coefficients can be found by solving this matrix equation which will have solutions when its determinant is zero:

$$\begin{vmatrix} H_{11} - E_i & H_{12} & \cdots & H_{1N} \\ H_{21} & H_{22} - E_i & \cdots & H_{2N} \\ \vdots & \vdots & \ddots & \vdots \\ H_{N1} & H_{N2} & \cdots & H_{NN} - E_i \end{vmatrix} = 0. \tag{1.17}$$

In matrix algebra, finding the eigenvalues and vectors of a matrix is equivalent to diagonalising it and there are efficient numerical algorithms to achieve diagonalisation. There are, however, challenges with this method involving the computational size of matrices and the knowledge of the residual interaction itself. In principle, there is no upper bound to the number of states in a nucleus with a particular spin and parity if unbound states are considered. Additionally, the number of bound states are extremely large. Approaches therefore truncate the model space to restrict the size of the matrices and reduce the number of configurations by restricting the number of active orbitals. As illustrated in Figure 1.3, an inert core is usually defined below the Fermi surface and configurations involving excitations of nucleons out of the core in the external space are too highly excited to play an important role at low excitation energies. Nucleons in orbitals with large single-particle energies above the surface are treated similarly. Orbitals in the core and external space therefore tend to be ignored, and only valence orbitals are considered. The choice of this model space is a balance between including enough orbitals to cover the degrees of freedom needed to describe the physics of interest and the size of the calculation. For the residual interaction, one usually starts with a specific form of the nucleon-nucleon interaction deduced from nucleon scattering, modifying it for in-medium effects to calculate single-particle matrix elements. Shell model calculations tend to be done for simple relevant systems close to magic numbers with the addition of one or two nucleons, and matrix elements are adjusted to fit relevant experimental measurements such as energy levels. The resulting is a set known as the shell model interaction which can be used to calculate more complex nuclei in a similar mass region [12, 13, 14, 15].

1.2 Shell evolution

Experimental evidence indicates that single-particle orbital centroids can shift relative to each other as nucleons are added to orbitals, altering shell structure in

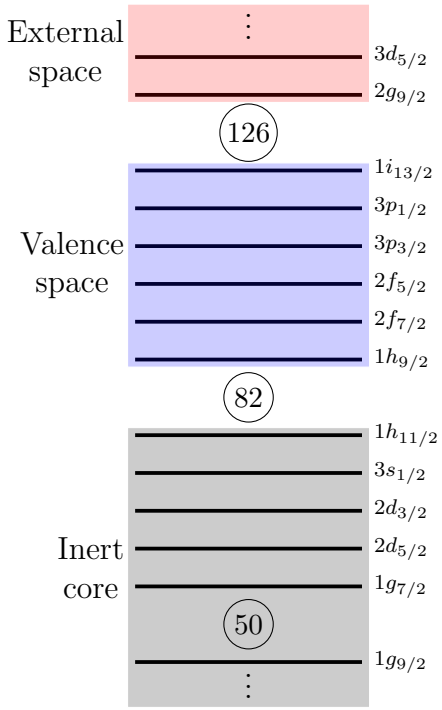


Figure 1.3: A schematic showing an example of the choice of model space used in shell-model calculations. Calculations involving orbitals in the inert core and external space would be ignored to reduce the number of calculations.

nuclei. Examples of this behaviour have been seen in light neutron-rich systems and in of heavier, nuclei. Many of these observations have been attributed to interactions between nucleons in different orbitals [16].

1.2.1 Monopole shift

Understanding interactions between valence neutrons and protons is important when describing the evolution of shell structure in nuclei. When moving along isotopic or isotonic chains, the occupancy of neutrons or protons in an orbital, j', changes the effect of interactions between nucleons of the other type in orbital j, varying its effective single-particle energy (ESPE). In principle, such effects should be described by shell-model calculations, assuming that the semi-empirical deduction of the interaction has been successful, and a sufficient model space can be used. However, thinking about monopole shifts caused by interactions of one type of nucleons with the other can be useful in identifying aspects of the nuclear force driving the changes.

The monopole component of the interaction between nucleons can be written as

$$V_{jj'}^{T} = \frac{\sum_{J}(2J+1)\,\langle jj'|\,V\,|jj'\rangle_{JT}}{\sum_{J}(2J+1)}, \tag{1.18}$$

where $\langle jj'|\,V\,|jj'\rangle_{JT}$ is the diagonal matrix element of a state for two nucleons coupled to angular momentum, J, and isospin, T. The term V represents an operator describing the interaction between the two nucleons. The summation over J are effectively averaging over the different combinations of orientations of different nucleon orbitals j and j'. The shift in the ESPE for protons occupying j', $\Delta\varepsilon_p(j)$, interacting with protons in orbital j is enhanced by the number of neutrons in orbital j', $n_n(j')$ and is given by

$$\Delta\varepsilon_p(j) = \frac{1}{2}[V_{jj'}^{T=0} + V_{jj'}^{T=1}]n_n(j'). \tag{1.19}$$

A similar equation can be constructed for $\Delta\varepsilon_n(j')$ based on the number of protons in j, $n_p(j)$ centroids [16].

1.2.2 Tensor interaction

The nuclear force also has a non-central tensor component, different from central components as it can result in an attraction or repulsion depending on the occupation $j_>$ or $j'_<$ orbitals. The discovery of this component of the nuclear force originates from observations of electromagnetic moments in the deuteron [17] resulting from admixtures of higher ℓ states to the predominantly $\ell = 0$ ground state. This admixture reproduces the experimental value for the magnetic moment and gives the ground state a slightly prolate shape. For a two-nucleon system, it can be written as

$$V_T = V_t(r)S_{12}, \tag{1.20}$$

where $V_t(r)$ is an attractive (negative) potential depending on the distance between nucleons and S_{12} is the tensor operator:

$$S_{12} = \frac{3(\boldsymbol{\sigma}_1 \cdot \mathbf{r})(\boldsymbol{\sigma}_2 \cdot \mathbf{r})}{r^2} - (\boldsymbol{\sigma}_1 \cdot \boldsymbol{\sigma}_2). \tag{1.21}$$

Symbols $\mathbf{r}$ and $\boldsymbol{\sigma}_{1,2}$ denote the relative positions of nucleons and spin vectors, respectively. S_{12} therefore takes on different values depending on how spins are

coupled. If spins combine to form an antisymmetric singlet state where $\boldsymbol{\sigma}_1 = -\boldsymbol{\sigma}_2$, then $S_{12} = 0$ and there is no effect from the tensor interaction. Alternatively, if spins couple to form a symmetric triplet state, when nucleons are aligned parallel to the direction of $\mathbf{r}$, S_{12} is positive and nucleons become more bound. When spins are aligned perpendicular to the direction of $\mathbf{r}$, the first term in Equation 1.21 is zero and S_{12} is negative, leaving the system less bound [18]. These configurations are illustrated on the left of Figure 1.4.

For systems with multiple valence nucleons outside a core, this description can be generalised. The effects can be calculated, but qualitative effects of the tensor interaction can be understood by thinking about nucleons in a $j_<$ ($j = l - s$) orbital interacting with those in a $j'_>$ ($j' = l' + s$). Considering the uncertainty principle, the relative angular momentum of these states is large creating a narrower spatial distribution in the plane of the orbits. This corresponds to a prolate distribution (left of Figure 1.4) where, analagous to the deuteron ground state, nucleons will be energetically preferred. The situation is also shown for nucleons in $j_<$ and $j'_<$ (or $j_>$ and $j'_>$) on the left of Figure 1.4. This arrangement has a smaller relative momentum and a larger spatial distribution in the plane of the orbits resulting in an oblate shape for the relative wave function contributing to an overall repulsion of nucleons. A pictorial description of this effect showing the interaction between different orbitals is shown on the right of Figure 1.4. The magnitude of this effect is greater when the radial overlap of wave functions for orbitals involved is larger, and increases if the relative momentum between nucleons is greater. As a result, the effect is enhanced for nucleons with more similar orbital angular momenta and for nucleons in orbitals with larger overall orbital angular momenta [16].

1.2.3 Light and medium mass neutron-rich systems

There is evidence for the disappearance of $N = 20$ and emergence of $N = 16$ sub-shell closures in light neutron-rich systems, suggesting that ^{24}O is doubly magic. One indicator comes from neutron separation energies, S_n, in this region, and Figure 1.5 shows values for isotopes with different numbers of neutron excess. The left figure shows S_n for odd-N, even-Z nuclei and the right figure that for odd-N, odd-Z nuclei. It can be seen that decreases in S_n across isotonic chains appear at traditional magic numbers for $N = 8$ and $N = 20$, highlighted by black vertical dotted lines. As protons are removed from isotopes and the neutron excess for a given neutron number increases, a decrease in S_n can be seen at $N = 16$ in both

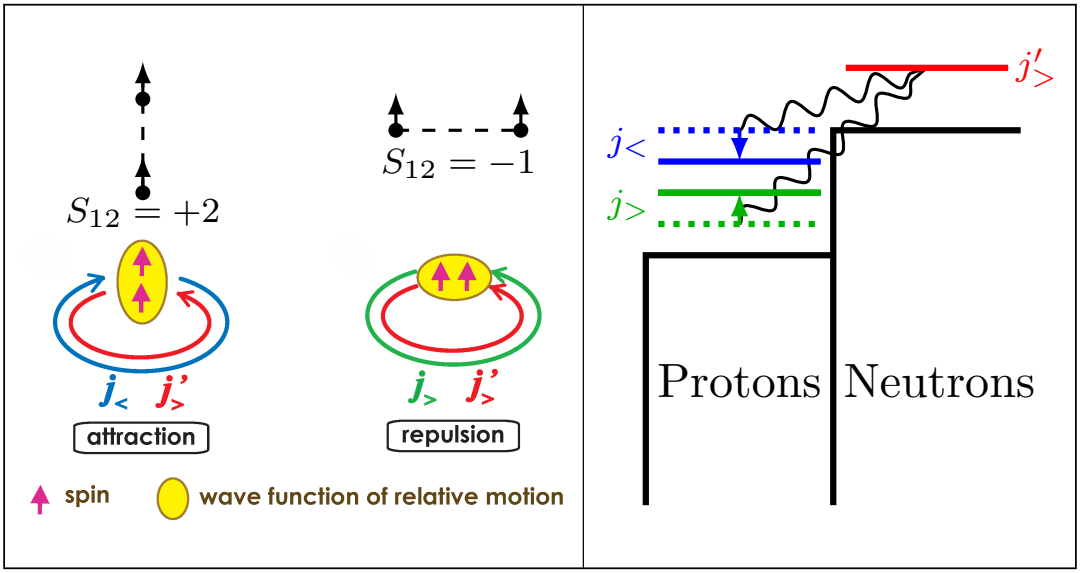


Figure 1.4: The left image shows values of the tensor interaction for different spin arrangements and a diagram illustrating the force between two nucleons based on the arrangements of spins. The right image is a schematic showing the effects of the tensor interactions based on the interaction of $j_>$ and $j_<$ proton orbitals with a $j'_>$ neutron orbital. Adapted from References [16, 19].

figures for neutron excesses greater than 5. This has been highlighted by red-dotted lines in Figure 1.5 and indicates the existence of a magic number [20]. This is reinforced by looking at first-excited 2^+ energies for C, O, Ne and Mg isotopic chains, shown in Figure 1.6, where a clear increase can be seen for ^{24}O compared to other even-even isotones [21]. The mechanism behind the appearance of this shell gap has been attributed to monopole tensor interaction from the attraction between protons in $\pi 1d_{5/2}$ and neutrons in $\nu 1d_{3/2}$ orbitals. Moving to ^{24}O along $Z = 8$, protons are removed from the $\pi 1d_{5/2}$ orbital and the attraction between the orbitals is decreased, reducing the energy gap. The $\nu 1d_{3/2}$ orbital therefore becomes less bound moving closer to the pf-shell, creating a new shell closure at $N = 16$.

Similarly, there is evidence for the emergence of subshell closures for $N = 32$ and $N = 34$ in ^{52}Ca and ^{54}Ca from observations of increased excitation energies in first-excited 2^+ states compared to even-even isotonic neighbours [24, 25, 26]. Looking at black data points for $N = 30$ isotones on the right-hand plot of Figure 1.7, it can be seen that the first-excited 2^+ state in doubly-magic ^{58}Ni ($Z = 28$) is approximately 0.4 MeV more than that in ^{50}Ca ($Z = 20$). When going to $N = 32$ isotones, there is a large increase of the 2^+ state in ^{52}Ca relative to ^{60}Ni indicating the existence of an $N = 32$ subshell gap for $Z = 20$. A comparable energy for the first 2^+ state in ^{54}Ca, shown on the left in Figure 1.7, and a large

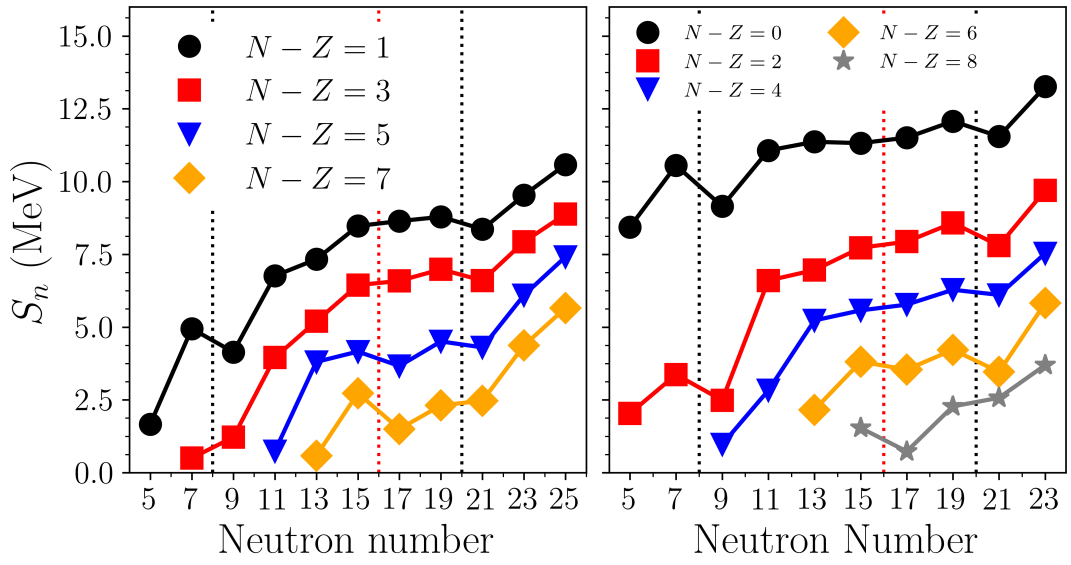


Figure 1.5: Neutron separation energies at different neutron numbers and proton excesses. The left figure shows isotonic chains for nuclei with odd N and even Z. The right figure shows odd-N, odd-Z nuclei. Black vertical dotted lines show traditional magic number at $N = 8$ and 20. Red vertical dotted lines highlight the emergence of the magic number at $N = 16$. Solid lines are included to guide the eye. Adapted from Reference [20].

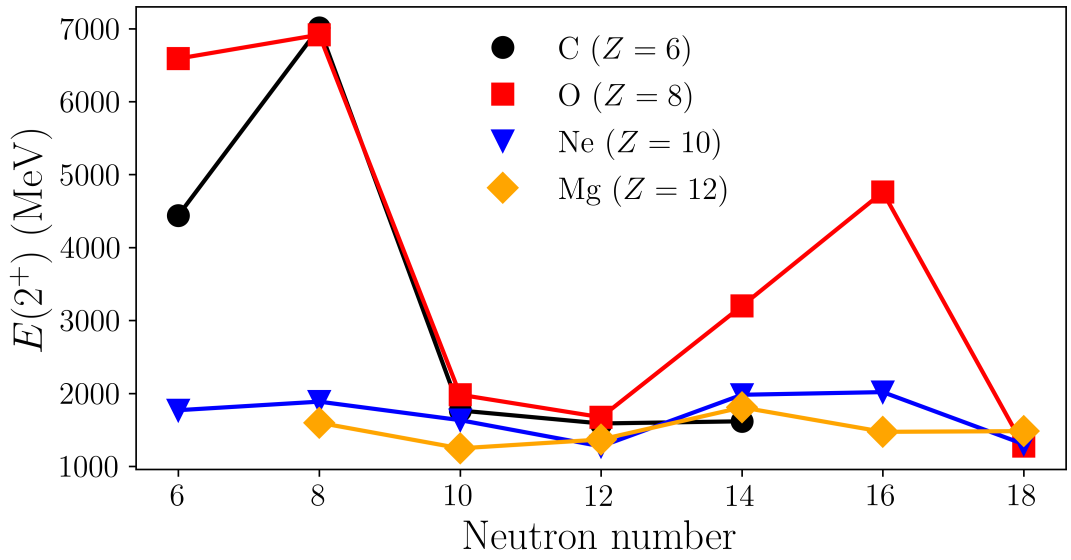


Figure 1.6: First-excited 2^+ states in C, O, Ne and Mg isotopic chains. Adapted from Reference [21] with data added from References [22, 23] for ^{26}O and ^{20}Mg.

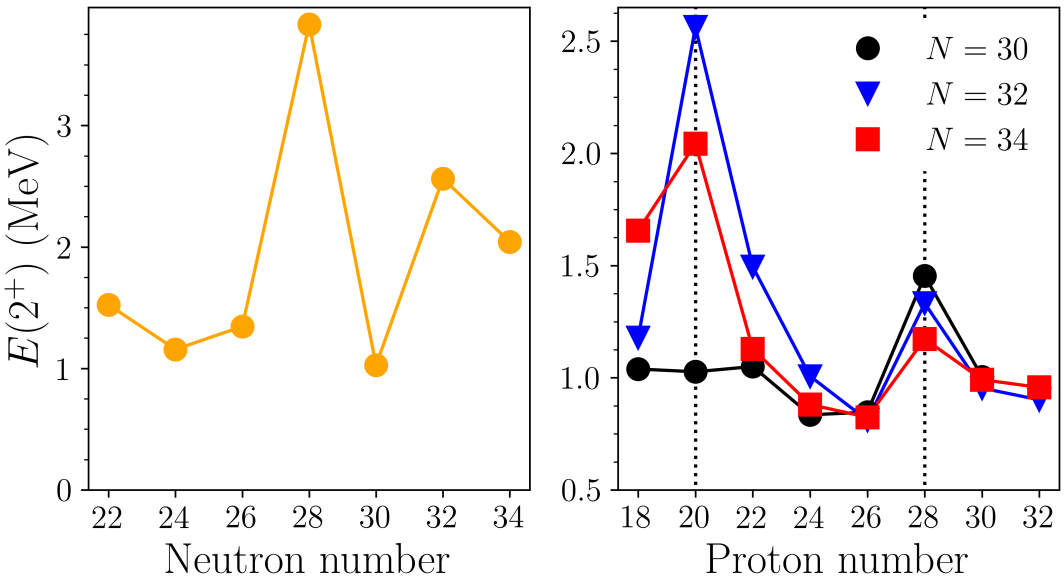


Figure 1.7: The left figure shows energies of first-excited 2^+ states in Ca isotopes. The right figure shows first-excited 2^+ states along the $N = 30$, 32 and 34 isotonic chains. Dotted lines indicate magic proton cores at $Z = 20$ and 28. Solid lines in both figures are used to guide the eye. Adapted from Reference [26] with data from Reference [27] and Reference [28] added for ^{50}Ar and ^{52}Ar, respectively.

increase compared to other $N = 34$ isotones was also observed from in-beam γ-ray spectroscopy measurements following one- and two-knockout reactions on ^{55}Sc and ^{56}Ti. From this, it has been inferred that ^{54}Ca is also doubly magic with $N = 34$ being another subshell closure for $Z = 20$. Closures have been suggested to emerge from nucleon-nucleon tensor interactions between protons and neutrons in $\pi 1f_{7/2}$ and $\nu 1f_{5/2}$ orbitals. As protons are removed from the $\pi 1f_{7/2}$ orbital, the attraction of the $\pi 1f_{7/2}$ and $\nu 1f_{5/2}$ orbitals is weakened, increasing the energy gap between them and leading to subshell closures at $N = 32$ and $N = 34$.

Other examples of shell evolution in light neutron-rich systems includes the disappearance of the $N = 28$ shell closure in ^{42}Si [29] and the disappearance of $N = 20$ in ^{32}Mg [30], with evidence for both from observations of decreased first-excited 2^+ energies.

1.2.4 Trends in heavier stable nuclei

Trends of single-particles states have also been observed in heavier stable nuclei. Using Sn(α, t) transfer reactions in normal kinematics, with an α-particle beam on stable Sn isotopes, states for $\pi 1g_{7/2}$ and $\pi 1h_{11/2}$ orbitals were probed in $^{113-125}$Sb

isotopes [31]. In this systematic study, the lowest lying $7/2^+$ and $11/2^-$ states across the isotopic chain were observed to contain over 90% of the spectroscopic strength with the expected single-particle strength to within 15%. This suggests that these states can be described as single-particle in nature and observed energies are approximately that of the $\pi 1g_{7/2}$ and $\pi 1h_{11/2}$ orbitals. The binding energy of these orbitals are shown in Figure 1.8, and it can be seen that the separation in binding energy between states increases to approximately 2 MeV moving up the isotopic chain. The behaviour of these orbitals can be explained as originating from a tensor monopole interaction. Neutron occupancies in this region are shown in Figure 1.9, where an increase in neutrons occupying the $\nu 1h_{11/2}$ orbital can be seen compared to other orbitals outside. As neutrons fill the $\nu 1h_{11/2}$ orbital, the attractive interaction between the $\pi 1g_{7/2}$ increases, and it is pulled down in energy relative to $\pi 1h_{11/2}$. The $\pi 1h_{11/2}$ orbital is also pushed up in energy relative to the $\pi 1g_{7/2}$ orbital as a result of experiencing a repulsive interaction from the $\nu 1h_{11/2}$ orbital. This interpretation was able to successfully explain observed single-particle trends with calculations of proton ESPE including a tensor monopole interaction [16]. A comparison of calculations with and without a tensor term are shown in Figure 1.8.

Similarly, the behaviour of neutron orbitals $\nu 1i_{13/2}$ and $\nu 1h_{9/2}$ have been studied through the population of single-particle states using (α,^{3}He) transfer reactions in normal kinematics on the stable $N = 82$ isotones ^{138}Ba, ^{140}Ce, ^{142}Nd and ^{144}Sm [34]. The energy difference of $\nu 1i_{13/2}$ and $\nu 1h_{9/2}$ ESPE centroids and the difference between the lowest $9/2^-$ and $13/2^+$ states are shown in Figure 1.10, exhibiting a decrease with atomic number. Experimental proton occupancies for these isotopes suggests that $\pi 1g_{7/2}$ and $\pi 2d_{5/2}$ fill across this isotopic chain [35] which, according to tensor-force interactions, will have opposite effects on $\nu 1i_{13/2}$ and $\nu 1h_{9/2}$ orbitals due to different spin-orbit couplings ($j_<$ versus $j_>$). However, the radial overlap of $\pi 1g_{7/2}$ should be much greater than $\pi 2d_{5/2}$ for high-j neutron orbitals. As a result, $\nu 1i_{13/2}$ should feel an overall repulsion and $\nu 1h_{9/2}$ an attraction, causing them to move towards each other in energy across the isotopic chain, and this qualitative description agrees with experimental observations in Figure 1.10.

Moving to $N = 50$ nuclei, single-particle centroids of states using data from (d,p) and (α,^{3}He) reactions in ^{86}Kr, ^{88}Sr, ^{90}Zr, and ^{92}Mo are shown in Figure 1.11 [36], where a decrease in the difference between ESPE centroids of $\nu 1g_{7/2}$ and $\nu 3s_{1/2}$ orbitals can be seen. Proton occupancies in this region from proton transfer reactions are also shown in Figure 1.11. The population of the $\pi 1g_{9/2}$ orbital is

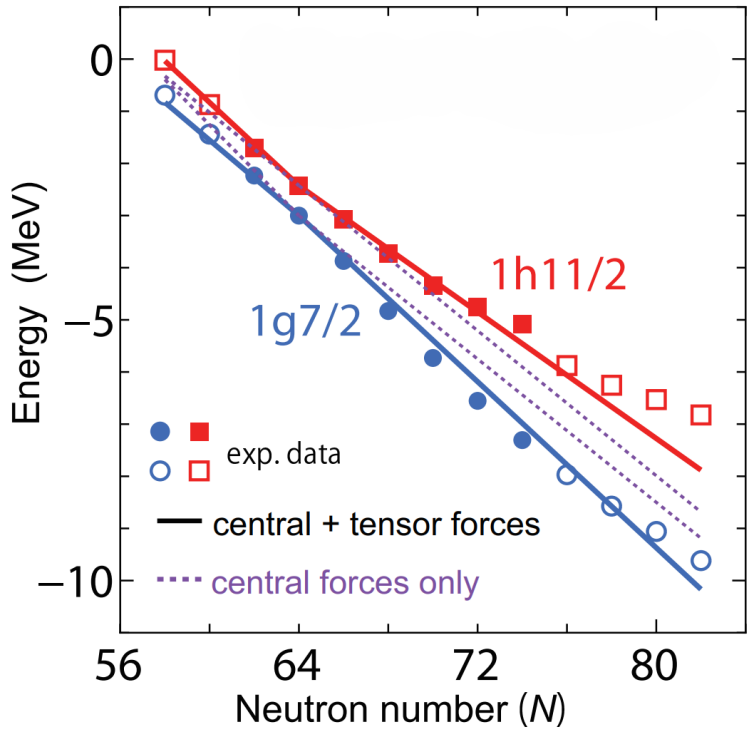


Figure 1.8: Experimental data showing the binding energy of the lowest lying $7/2^+$ and $11/2^-$ states in Sb isotopes. Filled data points are from transfer reactions in Reference [31]. Unfilled data points correspond to states where spin assignments have been made, but the spectroscopic strength of the state is not known. Solid and dashed lines are calculations of binding energies for $\pi 1g_{7/2}$ and $\pi 1h_{11/2}$ orbitals with the tensor term included and omitted, respectively. Figure taken from Reference [32].

low below $Z = 40$ and increases above this at a faster rate compared to $\pi 2p_{3/2}$, $\pi 2p_{1/2}$ and $\pi 1f_{5/2}$ orbitals. There is a large radial overlap of neutrons in $\nu 1g_{7/2}$ with protons in $\pi 1g_{9/2}$ and, as protons fill $\pi 1g_{9/2}$, there is an attractive interaction, reducing the energy of the orbital. The difference in ESPE centroids between $\nu 3s_{1/2}$ and $\pi 1g_{9/2}$ orbitals also decreases as $\nu 3s_{1/2}$ does not experience the tensor interaction. A better agreement of calculations compared with experimental observations for differences between ESPE centroids was found with a tensor term included with central forces compared to calculations using only central forces.

In $N = 81$ nuclei, neutron-hole strength has been systematically studied for ^{137}Ba, ^{139}Ce, ^{141}Nd, and ^{143}Sm isotopes using (p,d) and $(^3\text{He},\alpha)$ transfer reactions in normal kinematics on stable target [38]. By extracting spectroscopic factors, ESPE centroids for $\nu 3s_{1/2}$ and $\nu 1h_{11/2}$ orbitals in this region were determined. In ^{134}Xe and ^{136}Ba, protons mainly fill the $\pi 1g_{7/2}$ orbital [39]. Moving to ^{140}Nd and ^{142}Sm, the change is occupancy of protons mainly occurs in the $\pi 2d_{5/2}$ orbital [35]. In this study, changes to the effect of monopole shifts of neutron orbitals resulting from changes in proton occupancies were able to reproduce experimentally observed

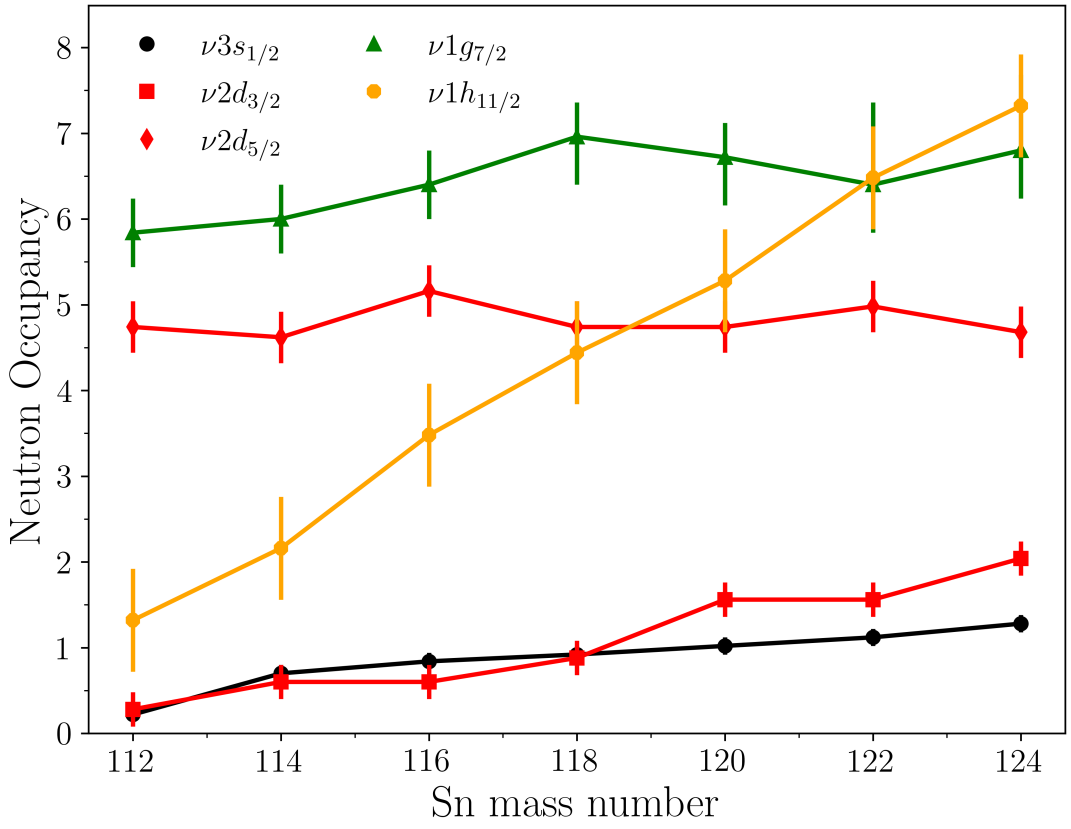


Figure 1.9: Experimental data showing neutron occupancies in $^{112-124}$Sn. Data taken from Reference [33].

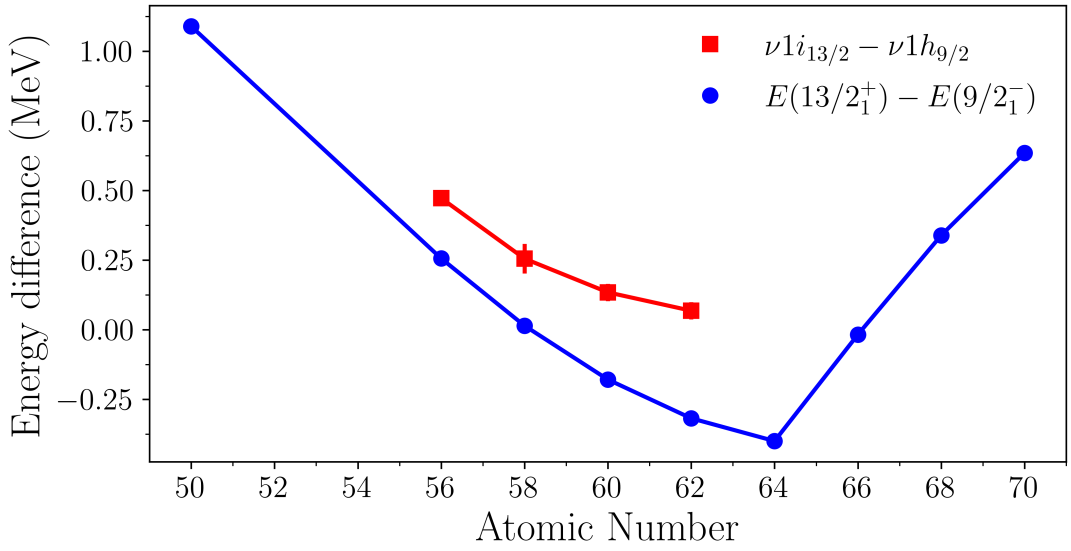


Figure 1.10: Experimental data showing the energy difference of $\nu 1i_{13/2}$ and $\nu 1h_{9/2}$ centroids and the energy difference between the lowest $9/2^-$ and $13/2^+$ states for $N = 83$ nuclei. Adapted from Reference [36].

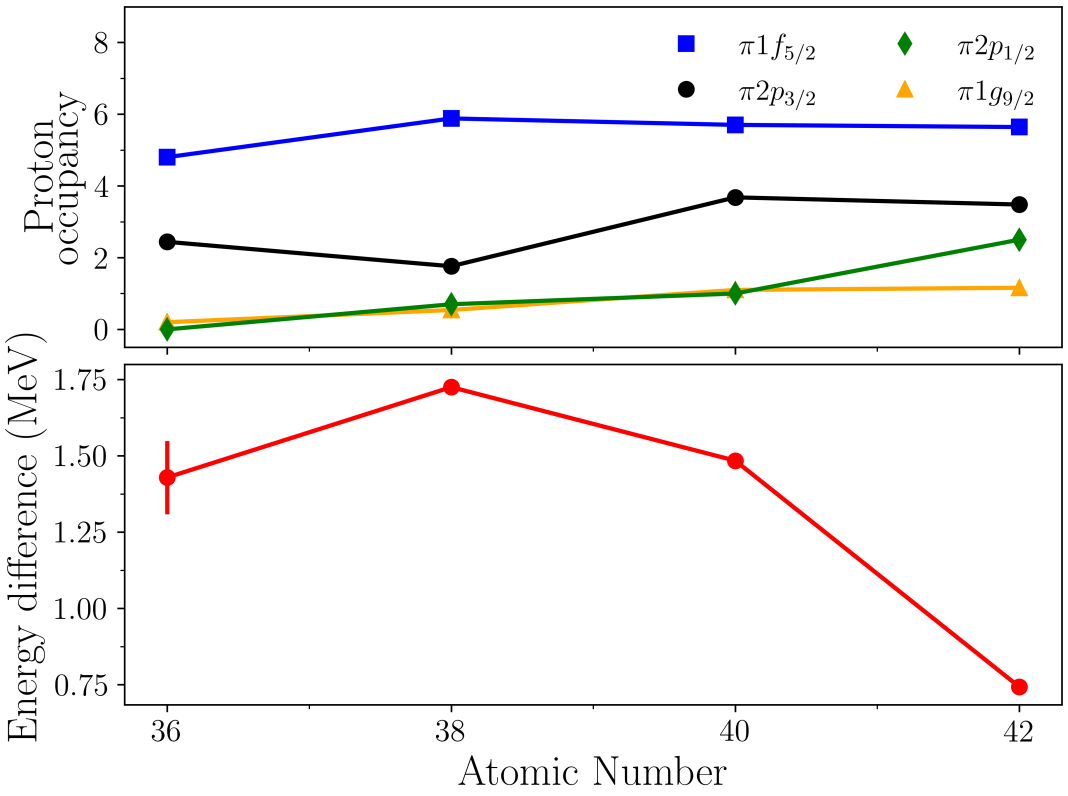


Figure 1.11: The top figure shows experimental data of valence proton occupancies across $N = 50$ isotopes with data taken from [37]. The bottom figure shows energy differences between $\nu 1g_{9/2}$ and $\nu 3s_{1/2}$ centroids for $N = 51$ nuclei. Adapted from Reference [36].

trends of ESPE centroids in $\nu 3s_{1/2}$ and $\nu 1h_{11/2}$ orbitals using effective two-body interaction calculations based on proton occupancies.

1.3 Aims of this work

The location of nuclei with one neutron outside $N = 126$ interacting with valence protons outside the $Z = 82$ closed shell provides a new region where trends of single-particle centroids can be investigated, and they are ideal systems to test modern shell-model calculations. The $\pi 1h_{9/2}$ orbital is expected to fill when moving up the $N = 126$ isotonic chain from ^{208}Pb, and any changes to single-particle centroids when a single neutron is added outside the $N = 126$ closed shell should then arise from the interaction of neutrons in $\nu 2g_{9/2}$, $\nu 2g_{7/2}$, $\nu 3d_{5/2}$, $\nu 3d_{3/2}$, $\nu 1i_{11/2}$, $\nu 1j_{15/2}$, and $\nu 4s_{1/2}$ orbitals with valence protons in the $\pi 1h_{9/2}$ orbital. These effects are expected be to stronger for $\nu 1i_{11/2}$ and $\nu 1j_{15/2}$ orbitals due to larger overlaps of radial wave functions with the $\pi 1h_{9/2}$ orbital. This can be seen in

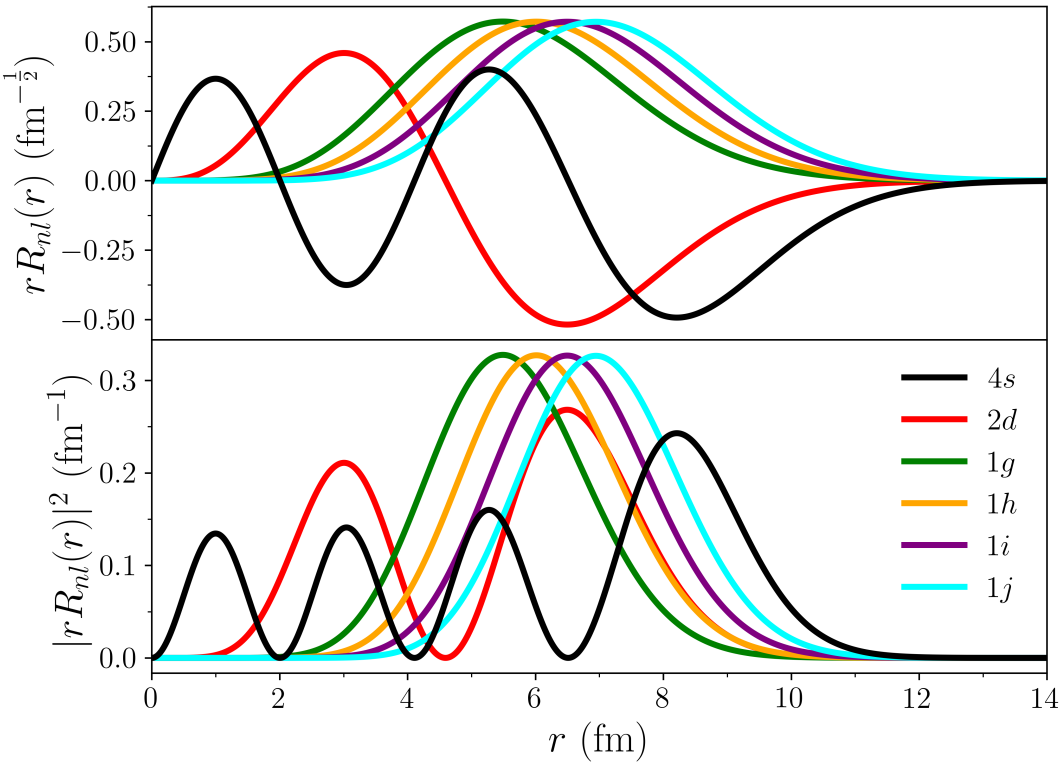


Figure 1.12: The top figure shows reduced radial wave functions for orbitals in an $A = 213$ nucleus. The bottom figure shows probability densities for the same orbitals. These have been calculated using a harmonic oscillator potential with the spin-orbit term omitted [10].

Figure 1.12, where reduced radial wave functions have been calculated for orbitals in ^{213}Rn using a harmonic oscillator potential.

Many studies using the (d,p) reaction on doubly magic ^{208}Pb have been conducted to probe single-particle states in ^{209}Pb [40, 41, 42, 43, 44, 45, 46, 47], while a single study on ^{210}Po was done with the (d,p) reaction in normal kinematics using a long-lived radioactive target [48]. More recently, information along this isotonic chain has been extended below ^{208}Pb using data from the $d(^{206}\text{Hg},p)^{207}$Hg reaction [49]. Relative spectroscopic factors normalised to the spectroscopic factor of the ground state for each nucleus across the isotonic chain are shown in Figure 1.13. The figure shows data from Reference [40] for ^{209}Pb, and it can be seen that no significant fragmentation of single-particle strength is observed when adding a neutron to doubly-magic ^{208}Pb. When protons are removed from the $Z = 82$ closed shell, fragmentation occurs for $\ell = 2$ single-particle states below 2 MeV in ^{207}Hg. When valence protons are added to the $Z = 82$ closed shell, some fragmentation occurs in single-particle states above 1 MeV corresponding to $\ell = 0$, 2 and 4 in ^{211}Po.

The motivation of this work is to extend studies along $N = 126$ and provide energies and spin assignments of states in ^{213}Rn using the transfer of neutrons in the $d(^{212}\mathrm{Rn},p)^{213}\mathrm{Rn}$ reaction to probe single-particle states. Energies and spin assignments in ^{213}Rn have previously been observed by comparing experimental conversion coefficients, measured from γ-γ coincidences following fusion-evaporation reactions, to theoretical calculations [50]. Conversion coefficients were also inferred from the detection of γ rays following the EC/β^+ decay of ^{213}Fr and compared to calculations to infer the spins of states in ^{213}Rn [51]. However, (d,p) transfer reactions have not previously been performed on ^{212}Rn and no spectroscopic information exists for ^{213}Rn that is directly sensitive to the underlying single-particle structure.

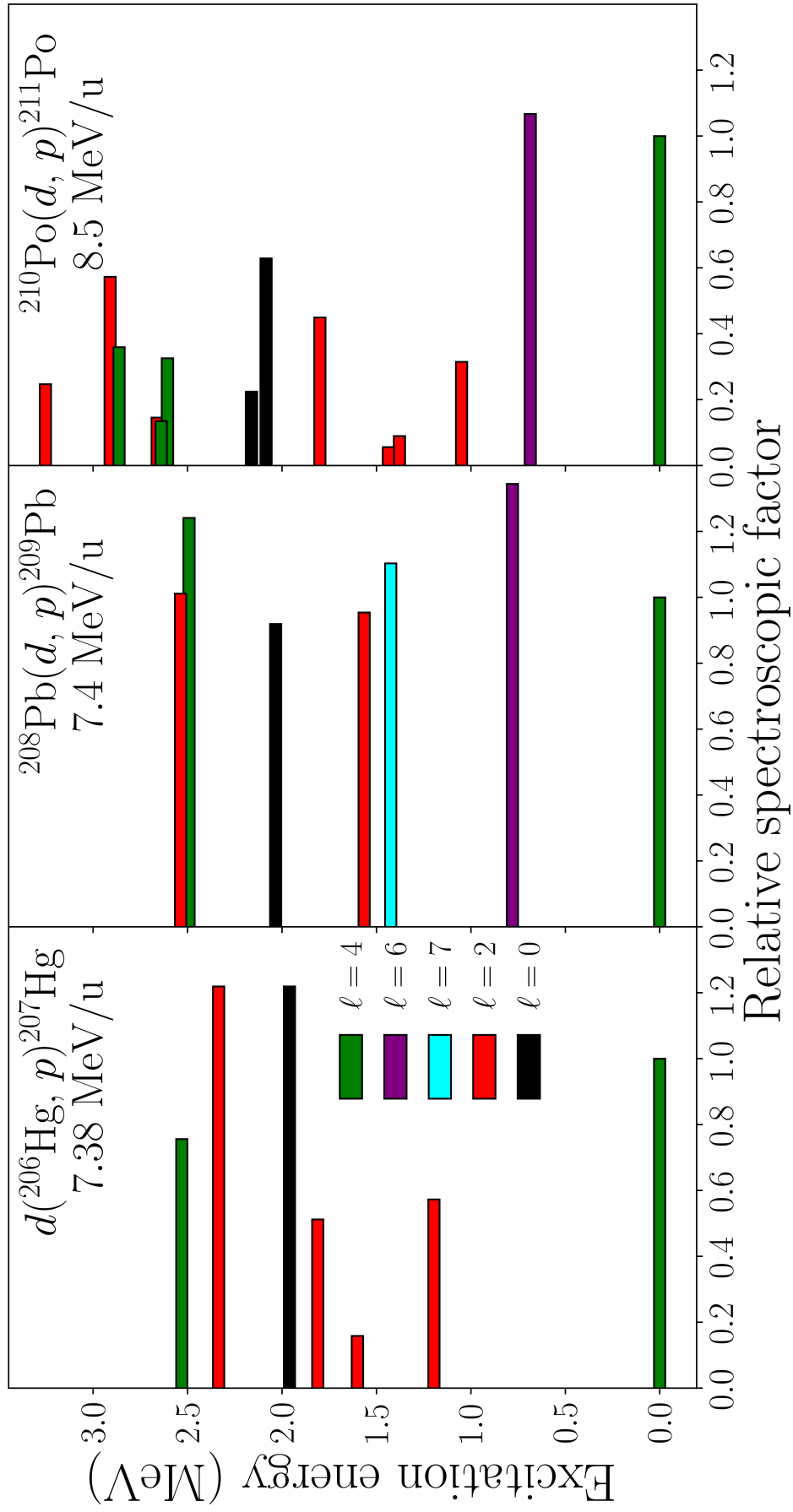


Figure 1.13: Relative spectroscopic factors for states in ^{207}Hg, ^{209}Pb and ^{211}Po extracted from transfer reactions. Spectroscopic factors have been normalised to the spectroscopic factor of the ground state. Figures have been labelled with the energy of each reaction. Data taken from References [40, 48, 49].

Blank page

Chapter 2

Probes of single-particle structure

This chapter discusses direct transfer reactions and their application as a probe to investigate the single-particle structure of nuclei. It provides a brief theoretical description of single-nucleon transfer reactions, along with details of the distorted-wave Born approximation (DWBA); a method used to model direct transfer reactions and calculate cross sections. Additionally, this chapter discusses the extraction of spectroscopic factors.

2.1 Reaction mechanisms

Different reaction mechanisms can take place when two nuclei interact. At one extreme, compound reaction mechanisms occur when nuclei fuse, forming an excited compound state in a multistep process where energy is shared amongst nucleons which are rearranged within the nucleus leading to a state of thermal equilibrium. This energy sharing introduces a randomness into the reaction that eliminates any memory of the type of particle that initiated it. Time scales of these types of reactions are at least around 10^{-19} s [52] and examples where compound processes are significant include proton and neutron capture, neutron induced fission and heavy-ion fusion evaporation.

Direct reaction mechanisms occur on the periphery of the nuclear surface via a single-step process in shorter time scales (approximately 10^{-22} s) than compound reactions. In these reactions there is minimal rearrangement of nucleons in the

nucleus. Examples of reactions that can have strong contributions from direct processes include elastic and inelastic scattering, and few- and single-nucleon transfer reactions [52, 53].

The probability of populating states in a direct reaction depends on the overlap of matrix elements connecting initial and final states. The single-step nature of direct reactions therefore tends to preferentially populate lower-lying states that more closely resemble the ground state of the target nucleus with a change in one degree of freedom. In direct transfer reactions such as (d,p), final states are strongly populated that have a large overlap with the ground state of the target plus a single neutron. This makes direct reactions a preferred method for probing single-particle states in nuclei.

It is also important to note that reaction processes exist on a range of mechanisms falling between these two extremes. These intermediate processes include pre-equlibrium reactions which involve the emission of particles from a compound nucleus before it reaches a statistical equilibrium as well as multistep mechanisms. Additionally, the occurrence of direct and compound reactions are not mutually exclusive and both types of reactions can be observed when performing an experiment [52, 54].

Experiments can be designed to enhance the contribution of direct transfer mechanisms over other types of processes. Beam energies of around 10·A MeV [55] are often selected to increase the probability of direct transfer reactions. This is important as nuclei should have enough energy to get close to, or overcome, the Coulomb barrier so that peripheral nuclear interactions can occur. The Coulomb potential, V_{C}, for the reaction in this work between the deuteron and ^{212}Rn in units of MeV can be approximated as

$$V_{\mathrm{C}} \approx 1.44 \frac{Z_1 Z_2}{R_1 + R_2}, \tag{2.1}$$

where Z_1 and Z_2 are the atomic numbers of the deuteron and ^{212}Rn, respectively, and R_1 and R_2 are the radii of the deuteron and ^{212}Rn in units of fm, respectively. Using $R_1 = 1.5$ fm and $R_2 = 7.2$ fm gives a Coulomb potential of approximately 14.2 MeV for the ^{212}Rn(d,p)^{213}Rn reaction. With a beam energy of 7.63 MeV/u, the total kinetic energy in centre-of-momentum (CM) frame is approximately 15.1 MeV and therefore large enough to overcome the Coulomb barrier. At much larger beam energies, compound reactions dominate. These are isotropic in the CM frame reflecting the statistical nature of the energy distribution

amongst nucleons during the decay process, whereas direct transfer reactions are characterised by high yields of ejectiles at forward CM angles. Choosing favourable beam energies and then measuring ejectiles at specific angles can therefore increase the detection of ejected particles from direct transfer reactions over other types of reactions.

In order to perform transfer reactions on unstable nuclei for which there are no practical targets available, it is necessary to use a radioactive beam containing the nucleus of interest incident on a light target. This reaction configuration is called inverse kinematics and contrasts with that of normal kinematics, which uses a light beam on a heavy target.

2.1.1 Reaction cross sections

Production yields of nuclear reactions are determined by reaction cross sections. The cross section defines the constant of proportionality of the number of emitted particles in a given reaction, Y, and the beam intensity, N_b, and number of target particles per unit area, N_t. In experiments, detectors or spectrometers covering a finite solid angle tend to be used to measure reaction products and so a differential cross section is defined that is related to the size of the solid angle covered by the detector, $\Delta\Omega$. The angular distribution of particles from direct reactions are not generally isotropic, therefore the differential cross section will depend on polar and azimuthal angles, θ and ϕ, defined relative to the beam direction [8, 52]. The differential cross section can be written as

$$\frac{\mathrm{d}\sigma}{\mathrm{d}\Omega}(\theta,\phi) = \frac{Y}{\varepsilon N_\mathrm{b} N_\mathrm{t} \Delta\Omega}, \tag{2.2}$$

where ε is an efficiency term taking into account the purity of the beam and target as well as the absolute efficiency of the detector.

2.1.2 Theory of single-nucleon transfer reactions

For a direct transfer reaction, $A(a,b)B$, the initial and final quantum states, or partitions, of the reaction can be defined as $\alpha = a+A$ and $\beta = b+B$. Initially, the light particle, a, moves in a potential created by nucleons in the target nucleus, A. Next, the transfer of a nucleon (or nucleons) occurs in a single step. Finally,

the ejectile particle, b, leaves the nucleus under the influence of the potential of the residual nucleus. An illustration of this process for a (d,p) reaction is given in Figure 2.1.

The interaction causing the transition between partitions α to β can be considered as a perturbation on the Hamiltonian describing initial and final states. Fermi's Golden Rule can be used to determine the transition probability of the direct reaction as

$$\lambda_{\beta\alpha} = \frac{2\pi}{\hbar}|V_{\beta\alpha}|^2 \rho\left(E_\beta\right), \tag{2.3}$$

where $\rho\left(E_\beta\right)$ is the density of final states and $V_{\beta\alpha}$ is the nuclear matrix element for the transition of the system from partition α to β. The definition of the nuclear matrix element is

$$V_{\beta\alpha} = \langle\Psi_\beta|\,\widehat{V}\,|\Psi_\alpha\rangle\,, \tag{2.4}$$

where Ψ_α and Ψ_β are total wavefunctions of incoming and outgoing systems, respectively, and $\widehat{V}$ describes the interaction potential that causes the reaction. The differential cross section for the reaction depends on the nuclear matrix element and can be written as

$$\left(\frac{\mathrm{d}\sigma}{\mathrm{d}\Omega}\right)_{\beta\alpha} = \frac{\mu_\alpha\mu_\beta}{\left(2\pi\hbar^2\right)^2}\frac{k_\beta}{k_\alpha}|V_{\beta\alpha}|^2. \tag{2.5}$$

Symbols μ_α and μ_β denote the reduced mass of each channel and k_α and k_β are their wave numbers [56]. From this equation, it can be seen that a larger nuclear matrix element will result in a larger differential cross section, and this occurs when there is a larger overlap between the initial and final states. For (d,p) direct transfer reactions, final states exhibit a large overlap with states resembling the initial plus a transferred neutron.

Initial and final-state wave functions are needed to calculate differential cross sections in Equation 2.5. These are often not easy to calculate and methods must be employed to approximate the reaction. A simple way to describe way the reaction is the plane-wave Born approximation [56, 57]. This considers the relative motion of incoming and outgoing partitions as plane waves and the interaction is treated as a small perturbation of elastic scattering. This method is able to qualitatively describe the correct shapes of angular distributions and adequately describes the role of angular momentum. However, discrepancies are found when comparing magnitudes of measured and calculated cross sections [53, 57]. Better agreement can be found by incorporating distortions of incoming and outgoing waves caused by the nuclear potential of the target nucleus.

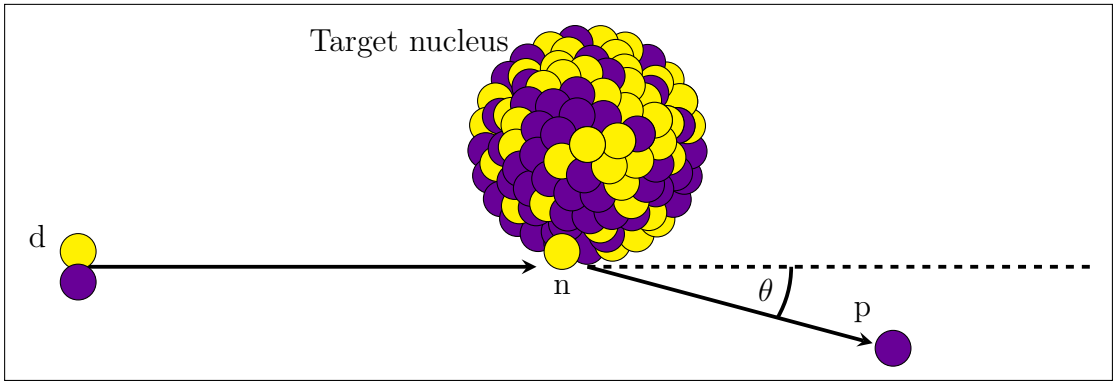


Figure 2.1: An illustration of a (d,p) direct transfer reaction. The deuteron is incident on a target nucleus and a neutron is transferred to a state via a single-step process. The proton is ejected influenced by the potential of the residual nucleus.

2.1.3 The distorted-wave Born approximation

Unlike the plane-wave Born Approximation, the distorted-wave Born approximation (DWBA) accounts for distortions of waves due to interactions with the target nucleus. This results in a more accurate representation of the scattering process and better agreement with experimental data. An overview of the DWBA specifically for a (d,p) reaction will be given here and symbols subscripts of d, T, p and R will refer to those of the deuteron, target, proton and residual nucleus, respectively. Detailed derivations related to the theory of direct reactions employing the DWBA can be found in References [52, 53].

The total Hamiltonian to describe the incoming channel is

$$\widehat{H} = \widehat{H}_\alpha + \widehat{T}_\alpha + \widehat{V}_\alpha, \tag{2.6}$$

where $\widehat{H}_\alpha = \widehat{H}_\mathrm{d} + \widehat{H}_\mathrm{T}$ is the internal Hamiltonian in the CM frame of the system, $\widehat{T}_\alpha$ is kinetic energy operator, also in CM frame, and $\widehat{V}_\alpha$ is an operator describing the interaction between the deuteron and the target. The associated Schrödinger equation is

$$(\widehat{H}_\alpha + \widehat{T}_\alpha + \widehat{V}_\alpha)\Psi_\alpha = E\Psi_\alpha, \tag{2.7}$$

with Ψ_α denoting the total wave function of the incoming channel. The exit channel can be written as

$$(\widehat{H}_\beta + \widehat{T}_\beta + \widehat{V}_\beta)\Psi_\beta = E\Psi_\beta. \tag{2.8}$$

The total wave function of the entrance channel can be described as a product of

functions describing relative motion, χ_β, and internal motion as

$$\Psi_\alpha = \psi_\alpha \chi_\alpha, \tag{2.9}$$

and the same can be written for the exit channel. The wave function describing internal degrees of freedom for the entrance channel of the (d,p) reaction, ψ_α, is

$$\psi_\alpha = \psi_\mathrm{d} \psi_\mathrm{T}. \tag{2.10}$$

Symbols ψ_i denote internal wave functions of Hamiltonians H_i with internal energies ϵ_i. As the associated Schrödinger equation is separable, the internal energy for the incoming channel is the sum of the internal energies of deuteron and the target. The same can be applied to the outgoing channel.

In the DWBA, the total Hamiltonian of incoming and outgoing channels is written in terms of optical potentials that describe elastic scattering (see Section 2.2.1). Implicit in this choice, the entrance and exit channels are assumed to be dominated by elastic scattering and the transfer process is described as a first-order perturbation. The Hamiltonian of the exit channel can be altered to include this optical potential, $\widehat{U}_\beta$, as

$$(\widehat{H}_\beta + \widehat{T}_\beta + [\widehat{V}_\beta - \widehat{U}_\beta] + \widehat{U}_\beta)\Psi_\beta = E\Psi_\beta. \tag{2.11}$$

Distorted waves are solutions to homogenous Schrödinger equations and can be substituted into Equation 2.4. The transition matrix element of entrance channel to the exit channel can then be defined as

$$V_{\beta\alpha} = \langle \psi_\beta \chi_\beta | \left(\widehat{V}_\beta - \widehat{U}_\beta \right) | \psi_\alpha \chi_\alpha \rangle . \tag{2.12}$$

The real interaction, $\widehat{V}_\beta$, is the sum of interactions

$$\widehat{V}_\beta = \widehat{V}_\mathrm{pn} + \widehat{V}_\mathrm{pA}, \tag{2.13}$$

where $\widehat{V}_\mathrm{pn}$ is the interaction potential between the proton and neutron transferred in the reaction and $\widehat{V}_\mathrm{pA}$ is the interaction potential between the proton and the nucleus. The optical potential is assumed to closely resemble elastic scattering meaning $\widehat{V}_\mathrm{pA} \approx \widehat{U}_\beta$ [53]. Equation 2.12 can therefore be rewritten as

$$V_{\beta\alpha} = \langle \psi_\beta \chi_\beta | \, \widehat{V}_\mathrm{pn} \, | \psi_\alpha \chi_\alpha \rangle . \tag{2.14}$$

The internal wave function, ψ_{R} for the residual nucleus in a (d, p) reaction can be described as the initial nucleus with the addition of a neutron in a single-particle orbital summed over all combinations of possible states. This can be written as

$$\psi_{\mathrm{R}} = \sum_{nj\ell} \gamma_{nj\ell} \phi_{nj\ell} \psi_{\mathrm{T}}, \tag{2.15}$$

where $\gamma_{nj\ell}$ are expansion coefficients whose square modulus give the probability of the neutron populating the residual nucleus in a particular single-particle state, $\phi_{nj\ell}$. In a similar way, the deuteron can be described as the sum a proton plus a neutron in all possible states and can be written as

$$\psi_{\mathrm{d}} = \sum_{n'j'\ell'} \gamma_{n'j'\ell'} \phi_{n'j'\ell'} \psi_{\mathrm{p}}. \tag{2.16}$$

Substituting these into Equation 2.14 gives

$$V_{\beta\alpha} = \sum_{nj\ell} \gamma_{nj\ell} \sum_{n'j'\ell'} \gamma_{n'j'\ell'} \left\langle \phi_{nj\ell} \psi_{\mathrm{T}} \chi_{\beta} \right| \widehat{V}_{\mathrm{pn}} \left| \phi_{n'j'\ell'} \psi_{\mathrm{p}} \chi_{\alpha} \right\rangle \tag{2.17}$$

which can be inserted into Equation 2.5 to give an expression for the differential cross section as

$$\left(\frac{\mathrm{d}\sigma}{\mathrm{d}\Omega} \right)_{\beta\alpha} = \sum_{nj\ell} \gamma^2_{nj\ell} \sum_{n'j'\ell'} \gamma^2_{n'j'\ell'} \frac{\mu_\alpha \mu_\beta}{(2\pi\hbar^2)^2} \frac{k_\beta}{k_\alpha} \left| \left\langle \phi_{nj\ell} \psi_{\mathrm{T}} \chi_{\beta} \right| \widehat{V}_{\mathrm{pn}} \left| \phi_{n'j'\ell'} \psi_{\mathrm{p}} \chi_{\alpha} \right\rangle \right|^2. \tag{2.18}$$

The term $\gamma^2_{nj\ell}$ is sometimes referred to as the spectroscopic strength or factor, and it describes the probability that the state populated in the residual nucleus is found as the target nucleus plus a neutron in a single-particle state with quantum number n, ℓ and j. Similarly, $\gamma^2_{n'j'\ell'}$ represents the probability that the deuteron is found as a proton coupled to a neutron in a single-particle state with n', ℓ' and j'. These can also be written as

$$S^{\mathrm{R}}_{nj\ell} = \gamma^2_{nj\ell} \tag{2.19}$$

$$S^{\mathrm{p}}_{n'j'\ell'} = \gamma^2_{n'j'\ell'}. \tag{2.20}$$

The differential cross section of a state can therefore be written in terms of spectroscopic factors and the DWBA differential cross section as

$$\left(\frac{\mathrm{d}\sigma}{\mathrm{d}\Omega} \right)_{\beta\alpha} = S^{\mathrm{R}}_{nj\ell} S^{\mathrm{p}}_{n'j'\ell'} \left(\frac{\mathrm{d}\sigma}{\mathrm{d}\Omega} \right)_{\mathrm{DWBA}}. \tag{2.21}$$

$S^{\mathrm{p}}_{n'j'\ell'}$ is approximately one.

In practice, calculations of DWBA differential cross sections are performed by computer codes as they require numerical methods to obtain distorted wave functions, evaluate transition matrix elements and handle integration processes. From these, experimental angular distributions measured for a state can be compared with calculations to verify that a given ℓ-transfer reproduces experimental data. These calculations also require input parameters of optical models and the accuracy of calculations depends on the choice of parameters.

2.2 Modelling a transfer reaction

Different reaction codes can be employed to calculate DWBA differential cross sections. In this work, the code PTOLEMY [58] was used. Other commonly used programmes include DWUCK [59], FRESCO [60], and TWOFNR [61] and these give very similar results when used with the same input parameters. To perform calculations, codes require distorted waves for incoming and outgoing channels, and overlap functions representing the relative motion of the transferred nucleon in the projectile and final state in the target nucleus. These are calculated using optical-model and bound-state parameter potentials which are defined by sets of input parameters.

2.2.1 Optical model

Details of the optical potential used in PTOLEMY can be found in Reference [58]. The potential is defined separately for entrance and exit channels and is the sum of multiple spherically symmetric contributions. It also includes imaginary terms describing the removal of flux from the elastic channel. The form of the potential is

$$\begin{aligned} V(r) = &-V_{\mathrm{v}} f_{\mathrm{v}}(r) + V_{\mathrm{so}} \frac{1}{r} \frac{\mathrm{d} f_{\mathrm{so}}(r)}{\mathrm{d}r} (\boldsymbol{\ell} \cdot \mathbf{s}) + V_{\mathrm{c}}(r) \\ &+ i \left[-\tilde{V}_{\mathrm{v}} \tilde{f}_{\mathrm{v}}(r) + \tilde{V}_{\mathrm{so}} \frac{1}{r} \frac{\mathrm{d} \tilde{f}_{\mathrm{so}}(r)}{\mathrm{d}r} (\boldsymbol{\ell} \cdot \mathbf{s}) + \tilde{V}_{\mathrm{s}} \frac{\mathrm{d} \tilde{f}_{\mathrm{s}}(r)}{\mathrm{d}r} \right], \end{aligned} \tag{2.22}$$

where subscripts v, so, c and s refer to volume, spin-orbit, Coulomb and surface terms, respectively. Strengths of potentials are given by V_i and $\tilde{V}_i$ for real and imaginary terms. Functions f_i and $\tilde{f}_i$ are Woods-Saxon potentials, each having

unique parameters r_i and a_i ($\tilde{r}_i$ and $\tilde{a}_i$ correspond to imaginary terms) describing the shape of the potential. If the mass number of the light nucleus is less than three, the radius of each potential is calculated from the mass number of the heavy nucleus as

$$R_i = r_i A_{\mathrm{T}}^{\frac{1}{3}}. \tag{2.23}$$

The Coulomb potential is described by the interaction for a uniformly charged sphere with radius, R_{c}, as

$$V_{\mathrm{c}}(r) = \begin{cases} \frac{Z_1 Z_2 e^2}{2R_{\mathrm{c}}} \left[3 - \left(\frac{r}{R_{\mathrm{c}}}\right)^2\right] & \text{if } r \leq R_{\mathrm{c}}, \\ \frac{Z_1 Z_2 e^2}{r} & \text{if } r > R_{\mathrm{c}}. \end{cases} \tag{2.24}$$

Shapes of potentials are shown in Figure 2.2. The sum of contributions creates an attractive potential at the centre of the nucleus, becoming repulsive as the distance from the centre increases due to the Coulomb term.

Potential depth parameters are calculated using fits to data from elastic scattering experiments, and those used in the current work are from such literature. This procedure can be done globally for nuclei across a range of masses, atomic numbers and beam energies, or locally where fits use data confined to specific regions of the nuclear chart at restricted energies. Care should be taken when selecting an optical-model parameter set. For global fits, localised effects may be smoothed out. When using local parameter sets, there is a greater that fits are influenced by secondary minima in the χ^2 surface and, although elastic scattering may be adequately described, the potentials may be less effective for calculations of reaction cross sections. Details about choices of optical-model parameters are given in Section 4.5.1.

2.2.2 Bound-state parameters

In calculations of DWBA cross sections, PTOLEMY also requires parameters to describe internal bound-state wave functions of projectile and target nuclei. For the target bound state, parameters characterise a Woods-Saxon potential that is the same form of terms in the real part of Equation 2.22, and the depths of potentials are varied to match the binding energy of the transferred nucleon to the modelled state. In this study, bound-state parameters to describe the target nucleus were taken from Reference [63] with a radius parameter of 1.28 fm and

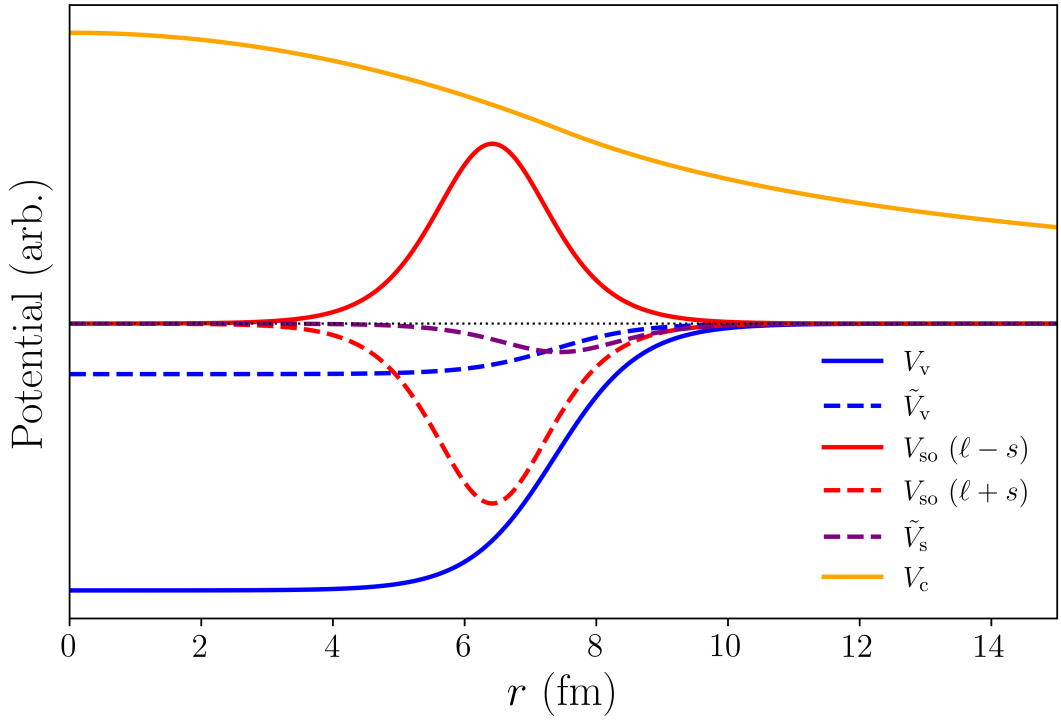


Figure 2.2: Components of the exit channel optical potential for the $d(^{212}\mathrm{Rn},d)^{212}\mathrm{Rn}$ reaction at 7.63 MeV/u with parameters from Reference [62]. Spin-orbit potentials have been shown for spins aligned (attractive) and anti-aligned (repulsive). Magnitudes of some potentials have been arbitrarily adjusted to aid visualisation.

diffuseness term of 0.65 fm. The spin-orbit potential was described with a depth of 6 MeV and radius and diffuseness parameters of 1.1 fm and 0.65 fm, respectively. For the bound-state of the light nucleus, the spectroscopic strength can be taken from ab initio calculations. In the case of the deuteron, it was obtained using Green function Monte Carlo calculations with the Argonne v_{18} potential [64]. Varying bound-state parameters does not tend to change the shape of angular distributions but can affect magnitudes of cross sections [65, 66, 15].

2.3 Spectroscopic information

DWBA calculations assume a target spectroscopic strength of unity. However, fragmentation of independent-particle model (IPM) orbital strength across many weaker states occurs as a consequence of residual interactions, mentioned in Section 1.1.2. Spectroscopic factors can be extracted, albeit in a model dependent

way, by comparing measured and calculated cross sections as

$$\left(\frac{\mathrm{d}\sigma}{\mathrm{d}\Omega}\right)_{\mathrm{EXP}} = S_{nj\ell}\left(\frac{\mathrm{d}\sigma}{\mathrm{d}\Omega}\right)_{\mathrm{DWBA}}. \tag{2.25}$$

2.3.1 Sum rules

For nucleon-adding and removal reactions, observed spectroscopic strength can be described using sum rules developed by Macfarlane and French [67]. If all states in an orbital have been observed, sum rules relate the total occupancy or vacancy of that orbital to the summed strength of spectroscopic factors.

For nucleon-adding reactions, such as (d,p), the number of vacancies in an orbital, N_{v}, with total spin, j, is given by

$$N_{\mathrm{v}} = (2j+1)\sum_i S_i^+, \tag{2.26}$$

where i runs over all states in the orbital each with a spectroscopic factor, S_i. The sum of spectroscopic factors is one for an empty orbital and therefore states that the number of vacancies is equal to the degeneracy of the orbital. For nucleon-removal reactions, the number of occupancies in an orbital, N_{o}, is

$$N_{\mathrm{o}} = \sum_i S_i^-. \tag{2.27}$$

If the orbital is completely full, the sum of spectroscopic factors is defined as

$$\sum_i S_i^- = 2j+1, \tag{2.28}$$

The sum of N_{v} and N_{o} should give the total degeneracy of the orbital.

In experiments, these sums have been found to be quenched by a constant factor of approximately 0.55 [63, 68] which has been interpreted as a consequence of short-range correlations between nucleons. Due to the repulsive component of the nucleon-nucleon interaction at short distances, nucleons form correlated pairs with high relative momentum and low CM momentum. Correlations therefore involve nucleons with kinetic energies greater than average nucleons in the nucleus and are responsible for the population of high-momentum states [69]. Consequently, single-particle strength is shifted to higher excitation energy. Transfer reactions

are generally not able to probe these higher-lying states.

2.3.2 Energy centroids

The energy centroid of a particular orbital, E_j, can be found by taking the average of all fragmented states weighted by their respective spectroscopic factors. In other words,

$$E_j = \frac{\sum_i E_i S_i}{\sum_i S_i}, \tag{2.29}$$

where the sum is over all states with an energy, E_i, and spectroscopic factor, S_i. Calculating centroids this way provides a method to estimate the single-particle energy of an orbital, assuming all single-particle strength has been observed.

Chapter 3

The $d(^{212}\mathrm{Rn},p)^{213}\mathrm{Rn}$ reaction at ISOLDE

Neutron-adding transfer reactions on ^{212}Rn were performed at the Isotope Separator Online Device (ISOLDE) facility in September 2021. This chapter will outline how radioactive isotopes were produced, ionised, separated and accelerated up to energies of 7.63 MeV/u—the highest kinetic energy (1617 MeV) of any post-accelerated radioactive ion beam (RIB) from the High Intensity and Energy-ISOLDE (HIE-ISOLDE) accelerator to date. This chapter will also detail the ISOLDE Solenoidal Spectrometer (ISS) device used to measure protons emitted from the $d(^{212}\mathrm{Rn},p)^{213}\mathrm{Rn}$ reaction, including relevant transfer reaction kinematics and the solenoidal technique employed by this device.

3.1 The ISOLDE RIB facility

ISOLDE is a facility at the European Organisation for Nuclear Research (CERN), Geneva that produces and accelerates RIBs. A schematic of the facility layout can be seen in Figure 3.1. Using the isotope separator online (ISOL) technique, isotopes are produced from a proton beam impinging on a thick, heavy primary target. Atoms of chemical elements diffuse and effuse out of the primary target, are ionised using specialised ion-sources, and are mass separated using an isotope separator. Selected nuclei can then either be transported to the low energy portion

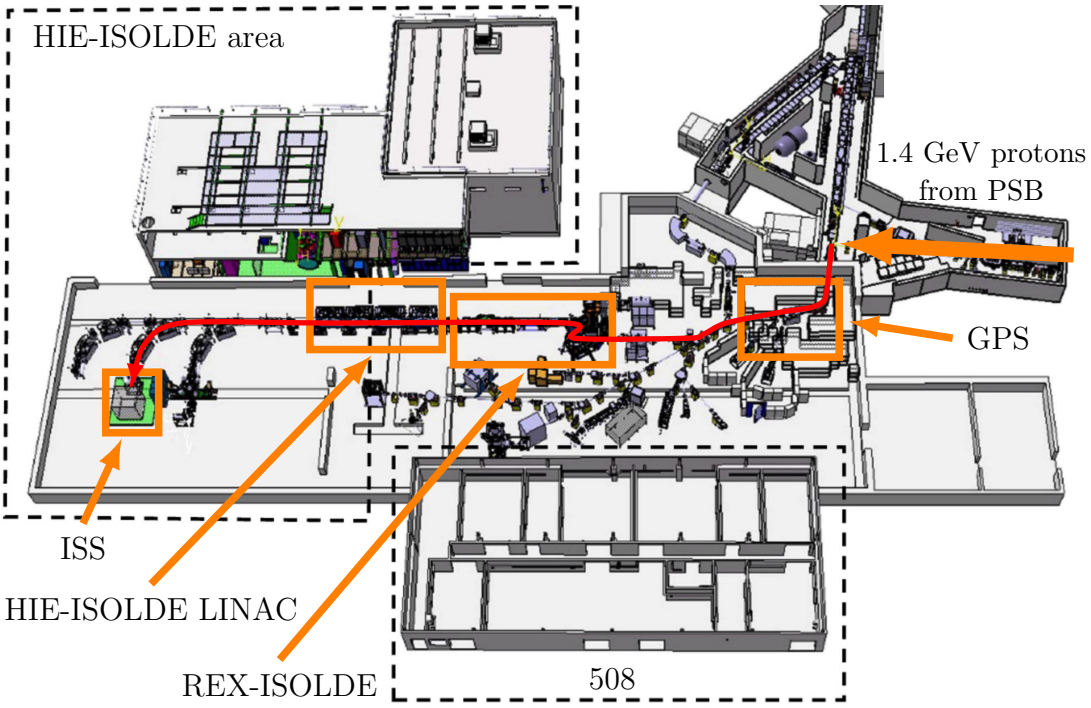


Figure 3.1: A schematic showing the layout of the ISOLDE facility. Components of the facility used to produce and accelerate ^{212}Rn nuclei have been labelled with orange boxes and arrows. The red arrow shows the path of the beam from the primary target to ISS. Building 508 contains the control room and offices for experiments. Adapted from Reference [70].

of ISOLDE at an energy up to 60 keV or—as was done in this experiment—post-accelerated up to a desired energy between 3.3 and 10 MeV/u before being delivered to HIE-ISOLDE experimental areas [70].

3.1.1 Isotope production

The ISOLDE facility receives protons in bunches from the Proton Synchrotron Booster (PSB) at a maximum rate of every 1.2 s and an energy of 1.4 GeV where they impinge on a primary target with an intensity of up to 2 µA. In this work, an average proton current of 0.5 µA was used, which was sufficient to produce yields of the isotope of interest at the required intensity.

Protons induce fission, fragmentation and spallation reactions in the primary target producing a range of isotopes [70], and different target materials are chosen based on the specific nucleus of interest in an experiment. For this experiment, a UC_x target was used which has a typical thickness of 45 g/cm^2 and diameter of 14 mm [71]. The rate of effusion and diffusion out can be increased by applying

an electrical current to heat the target, reducing release times to less than 1 s [72]. A current of 570 A was used in this experiment which is equivalent to raising the target to a temperature of around 2000 °C.

3.1.2 Element selection

After diffusing from the target, radioactive atoms are ionised via one of three ionisation sources: surface, plasma or laser. As Rn has a relatively large ionisation energy [73], it cannot be ionised efficiently via surface or laser methods, therefore plasma ionisation was selected. In this work specifically, a Versatile Arc Discharge Ion Source (VADIS) VD7 [74] was used. A plasma is generated by the acceleration of electrons through a potential between a cathode and extraction electrode. Collisions of atoms with these electrons leads to their ionisation producing $^{212}Rn^{1+}$ ions. This ion source also employs a water-cooled transfer line to suppress the transport of less volatile elements, reducing contamination [75].

To select the isotope of interest, ions extracted from the ion source are accelerated off a high-voltage platform that houses the target and ion source and delivered to a mass separator. The ISOLDE facility has two separators, with the General Purpose Separator (GPS) being used in this work. This device uses a double-focusing 70° magnet with a bending radius of 1.5 m to separate ions based on their mass-to-charge ratio [76] and has a design resolving power of 800 [70]. After mass separation, the main contaminants in the beam are isobars. Figure 3.2 shows information about potential contaminants that could be produced in the primary target, with yields given per µC of proton beam. It can be seen that ^{212}Fr and ^{212}Ra are the main potential isobaric contaminants, being produced in similar quantities to ^{212}Rn. However, with boiling points of 620 °C and 1737 °C for ^{212}Fr [77] and ^{212}Ra [78], respectively, compared to −62 °C for ^{212}Rn [73], beam contamination from these elements is suppressed by the water-cooled transfer line in the ion source. After separation, nuclei are post accelerated.

3.1.3 Post acceleration

Acceleration of the beam occurs via two linear accelerators (LINACs). First, the Radioactive beam experiment at ISOLDE (REX-ISOLDE) accelerator is used to accelerate nuclei up to 3 MeV/u [81]. This includes ion accumulation, bunching

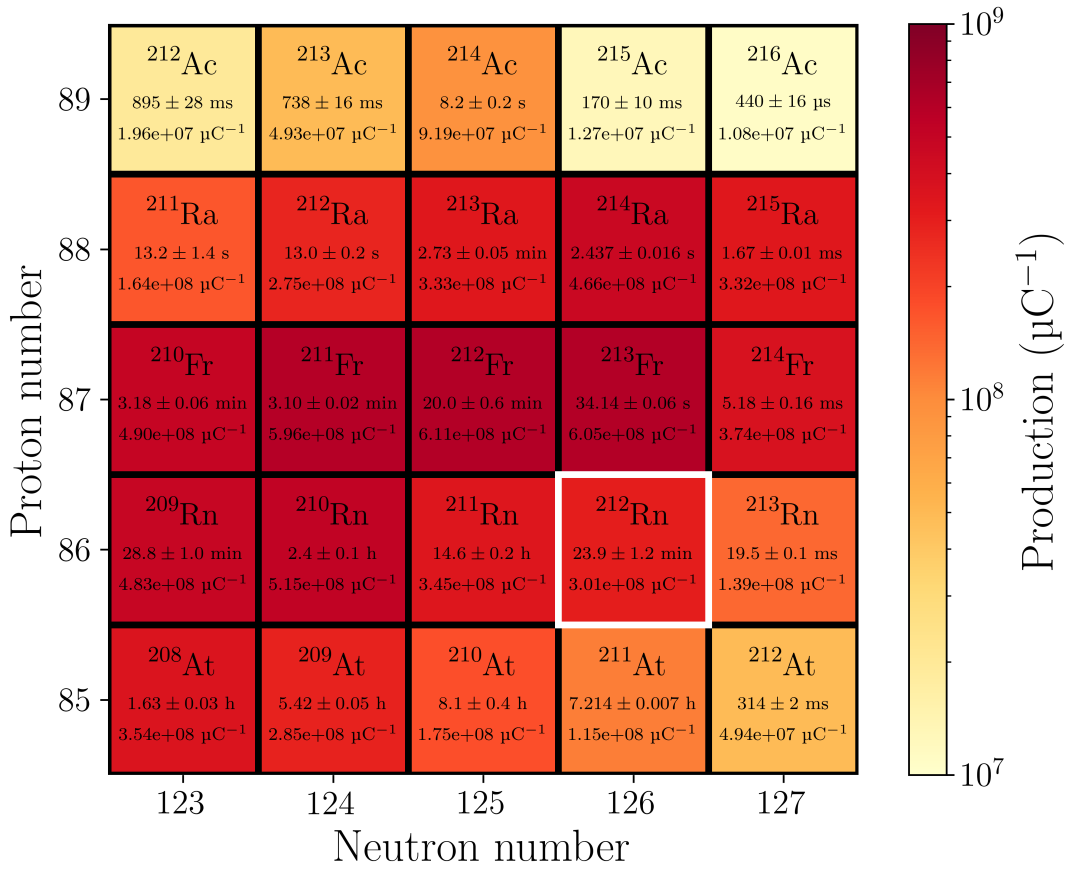


Figure 3.2: In-target production yields per μC of proton beam for elements in the mass region around ^{212}Rn. Half-lives are also shown. Data from References [79, 80] have been used.

and cooling in REXTRAP, charge-breeding in REXEBIS and acceleration in REX-LINAC. After this, nuclei pass through the superconducting HIE-ISOLDE LINAC where they can be accelerated up to energies of around 10 MeV/u, depending on the mass-to-charge ratio of the ion [82]. A drawing of the layout of equipment used for post acceleration is shown in Figure 3.3.

3.1.3.1 REX-ISOLDE

A schematic of REX-ISOLDE is shown in Figure 3.4. Before acceleration through the LINAC, a quasi-continuous beam of 1^+ ions enters the REXTRAP. This is a buffer-gas-filled Penning trap system that cools and accumulates the beam, preparing it for efficient low emittance, bunched delivery to the electron beam ion source (EBIS) device, REXEBIS. The trap sits inside the bore of a 3 T superconducting solenoid and has an entrance platform voltage set slightly below the potential of the ion source mentioned in the previous section. This electrostatically decelerates

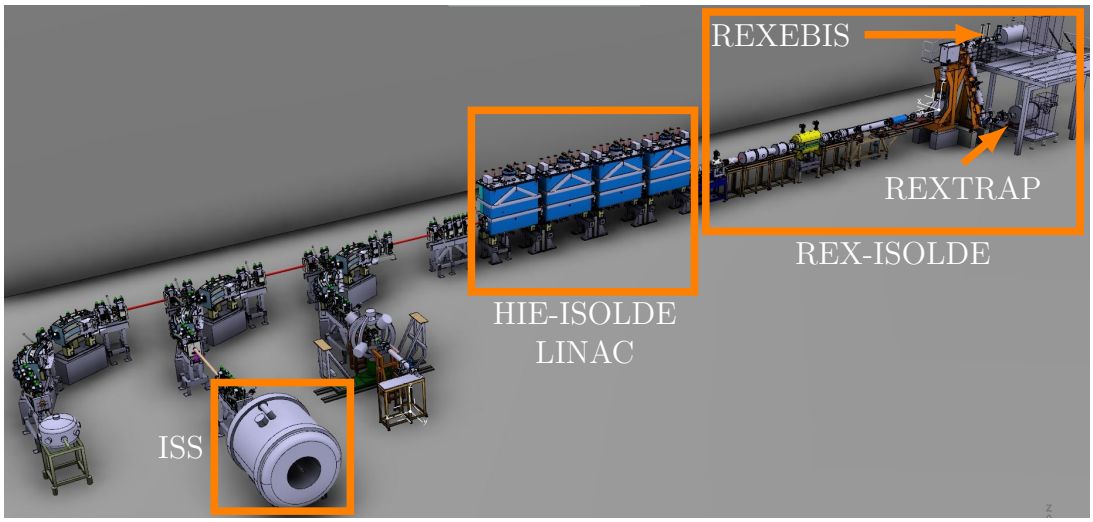


Figure 3.3: A drawing showing the layout of REX-ISOLDE, the HIE-ISOLDE superconducting LINAC and ISS in the ISOLDE facility. Adapted from Reference [83].

ions before they are injected into a region of high magnetic field containing the buffer gas pressures of up to 10^{-3} mbar. Ions are reflected by a potential near the exit of the trap and lose energy through collisions with buffer gas atoms contributing to longitudinal cooling. Radiofrequency quadrupole electric potentials are also used to provide radial confinement, resulting in ions accumulating at the minimum of the trap potential. After cooling, the potential at the exit of the trap is lowered, accelerating ions towards the EBIS [81, 84, 85, 86]. A schematic of this process is shown in Figure 3.5.

The REXEBIS device has the function of increasing the charge state of the ions. This charge breeding allows ions to be accelerated more effectively through the REX-LINAC. To achieve this, an injection potential is used to decelerate ions from REXTRAP. Charge breeding is performed via the impact of ions with a dense mono-energetic electron beam from an electron gun cathode. The electron beam is confined by a solenoidal magnetic field of up to 2 T over a distance of approximately 1 m. The first component of the REX-LINAC requires the mass-to-charge ratio of ions to be, $A/q < 4.5$ and a longer breeding time in REXEBIS, limited by the half life of the radioactive ion, creates a larger charge-state distribution of ions. In this work, $^{212}Rn^{+}$ ions were charge bred to $^{212}Rn^{50+}$ with $A/q = 4.24$ [87]. After reaching the desired charge state, the potential in the device is lowered. Ions are directed towards the first LINAC and the next ion pulse from the trap is injected for charge breeding. The repetition and breeding times will be discussed in Section 3.1.5. Before entering the LINAC, ions pass through another mass separator. This reduces contamination that may be present from

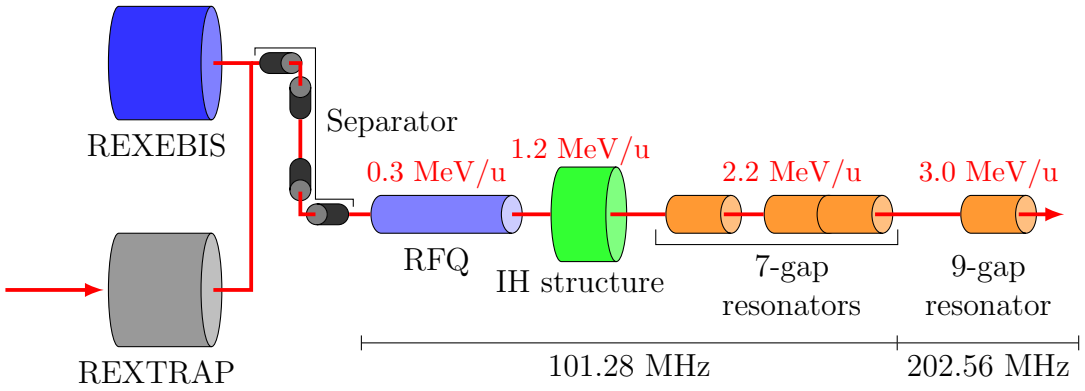


Figure 3.4: A schematic of REX-ISOLDE in the ISOLDE facility. The red line shows the path of the beam. The maximum beam energy reached in each component has been labelled. Adapted from Reference [93].

the buffer gas, again separating ions based on mass-to-charge ratios [88, 89, 90].

After the mass separator, ions are directed into the room-temperature REX-LINAC. This consists of a series of components to increase the overall energy of the beam, preparing it for injection into the super-conducting HIE-ISOLDE LINAC. A schematic of the LINAC is shown in Figure 3.4. The first component is a radio-frequency quadrupole (RFQ) which accelerates the ion beam to 0.3 MeV/u. From here, the beam goes through a 20-gap Interdigital H-type (IH) structure followed by three 7-gap resonators. Beam energies of 1.2 MeV/u are achieved in the IH structure and successive energies of up to 1.55, 1.88 and 2.2 MeV/u in each 7-gap resonator, all of which operate at 101.28 MHz. Finally, the beam reaches the 202.56 MHz 9-gap IH resonator, capable of accelerating ions up to 3 MeV/u [88, 91, 92]. After this, the beam is ready for the final stage of post-acceleration in the HIE-ISOLDE LINAC.

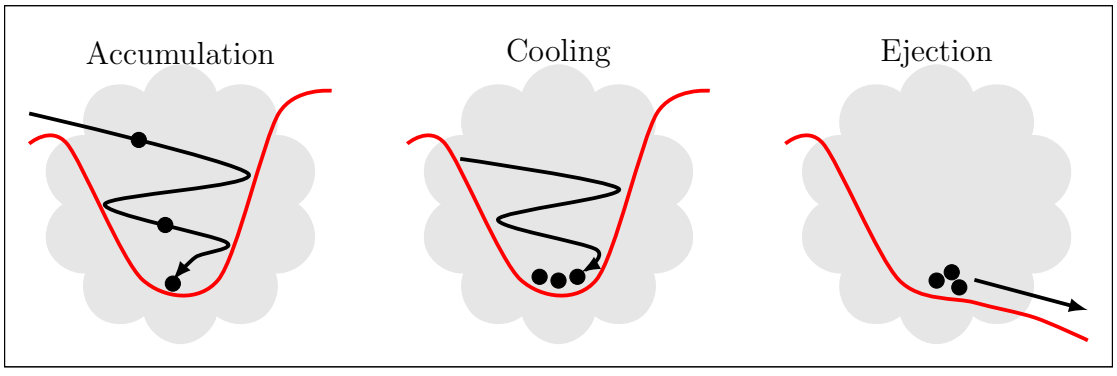


Figure 3.5: A schematic showing how REXTRAP accumulates, bunches and cools ion beams. Red lines indicate the potential along in the trap at each stage. Adapted from Reference [85].

3.1.3.2 HIE-ISOLDE

The HIE-ISOLDE LINAC receives the beam from REX-ISOLDE and accelerates it to energies of up to around 10 MeV/u. The device consists of four high-β superconducting cryomodules which can be seen in Figure 3.3. Each cryomodule contains five superconducting cavities and one superconducting solenoid for transverse beam focusing which are supercooled using liquid helium [94, 95].

3.1.4 Beam properties

The final energy of the beam for this measurement after post acceleration through the HIE-ISOLDE LINAC was 7.63 MeV/u with a full width at half maximum (FWHM) of 0.4%. The transmission efficiency from the primary target to ISS was approximately 2%, producing a beam intensity of around 10^6 pps [87]. No evidence of beam contamination was found, and the beam purity was estimated to be greater than 99%. Figure 3.6 shows calculations from the distorted-wave Born approximation (DWBA) code, PTOLEMY [58], of integrated cross sections in the angular range of the ejectile experimentally accessible in ISS. This has been done for each expected angular momentum transfer in this nuclear region, assuming the population of the ground state in the residual nucleus. An increase in cross section can be seen as the beam energy increases for all angular momentum transfers. Figure 3.7 shows angular distributions for different angular momentum transfers to the ground state of the residual nucleus at different incident beam energies in the approximate angular range measurable in ISS. It can be seen that the maxima of distributions become more forward peaked as the beam energy increases. The shapes of distributions also become more distinct, allowing ℓ-transfers to the residual nucleus to be identified more easily. The highest beam energy available was therefore selected for this work.

3.1.5 Timing

The timing of different facility components used to produce the final beam is shown in Figure 3.8. Cooling and accumulation inside REXTRAP was synchronised to the breeding time inside REXEBIS, which was set to 150 ms, giving a beam pulse rate of 6.67 Hz in ISS.

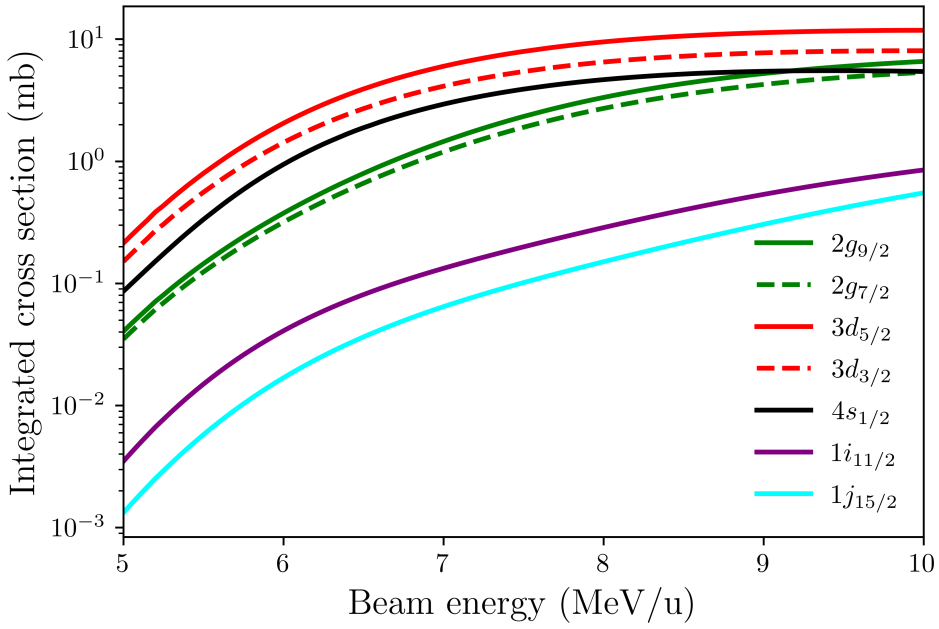


Figure 3.6: Integrated cross section calculations for different angular momentum transfers as a function of incident beam energy in the ^{212}Rn$(d,p)^{213}$Rn reaction using the DWBA code, PTOLEMY. A spectroscopic factor of $S = 1$ has been assumed and cross sections for each angular-momentum transfer have been calculated for a hypothetical state at 0 MeV. Optical-model parameters of Reference [96] and Reference [97] have been used for the deuteron and the proton, respectively. Bound state parameters are from Reference [63].

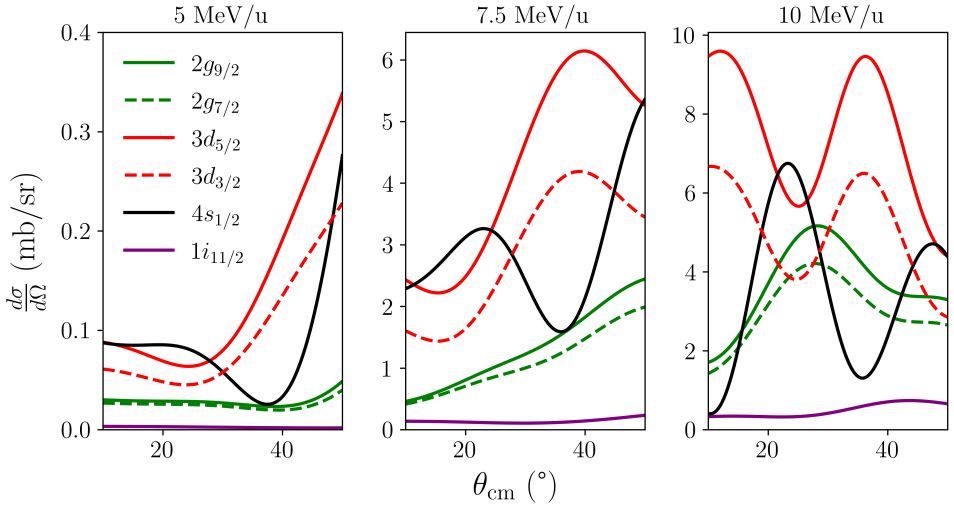


Figure 3.7: Calculations of angular distributions for angular momentum transfers at different incident beam energies in the ^{212}Rn$(d,p)^{213}$Rn reaction using the DWBA code, PTOLEMY. The energy per nucleon used in the calculations is given above each figure. A spectroscopic factor of $S = 1$ has been assumed and cross sections for each angular momentum transfer have been calculated to populate the ground state of the residual nucleus. Optical model and bound state parameters are the same as those used for calculations in Figure 3.6.

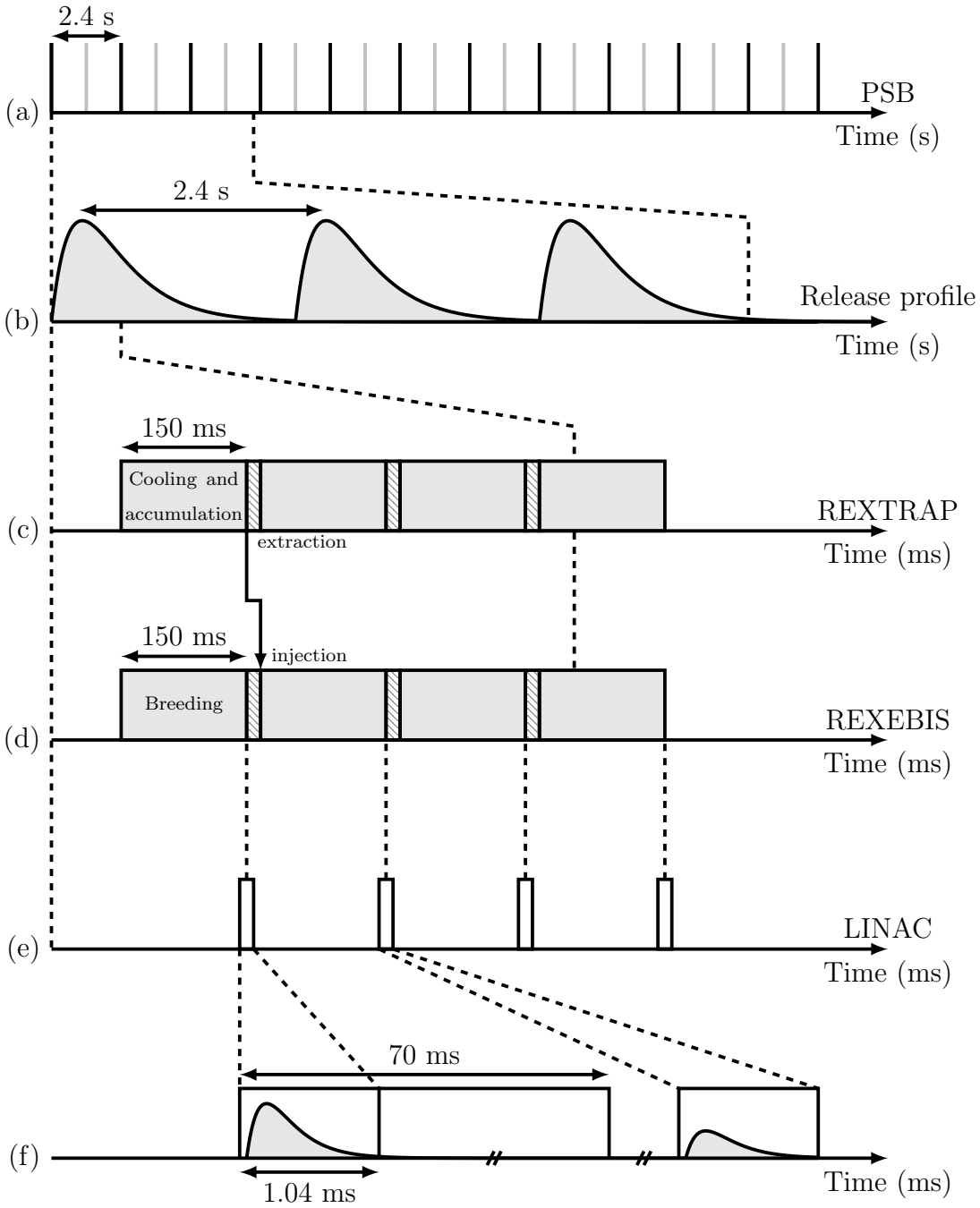


Figure 3.8: Schematic of the timing of different components at ISOLDE. (a) Proton bunches from the PSB are separated by 1.2 s with a width of around 100 µs. Primary targets at ISOLDE receive some fraction of the total produced bunches, shown as black vertical lines at the top of the figure. Other bunches from the PSB, shown as grey lines, are delivered to different experimental areas within CERN. (b) Release profiles of isotopes from the primary target. (c) Accumulated and cooled bunches from REXTRAP. (d) Charge-bred bunches from REXEBIS are synchronised to REXTRAP. (e) Injection to REXLINAC is synchronised to extraction from REXEBIS. (f) The extracted and accelerated beam used in ISS has a release time from REXEBIS of around 1 ms. Adapted from References [92, 98].

The release of ions from the REXEBIS into the REX-LINAC can be done in two modes: fast and slow extraction. Fast extraction releases most ions after around 200 µs and slow extraction spreads the release over 1 ms. Typically, for ISS measurements, slow extraction is used in order to minimise pile-up events in recoil detectors. However, as this measurement did not use recoil detectors, fast extraction was selected partway through the experiment to assist in removing unwanted α-particle background events from the decay of the beam. This had other unintended pile-up consequences that are discussed in Section 4.4.2.

Beam-on and beam-off windows for the ISS data acquisition system were defined in software relative to a trigger signalling the extraction of ions from REXEBIS. The beam-on window was chosen to cover timestamped data recorded during the release time of REXEBIS. The beam-off window covered data recorded between pulses. Data from the beam-off window were then used to perform a background subtraction of beam-on data. In this work, a beam-on time window of 1.04 ms and a total beam-on and beam-off time window of 70 ms were selected. More details on this are given in Section 4.2.2.

3.2 Transfer reaction kinematics

This section details the two-body kinematics used to describe transfer reactions, and how ions move in a solenoidal field. A brief description using relativistic kinematics is given followed by a more detailed classical description, as well as the challenges of performing an experiment in inverse kinematics. A full relativistic derivation of transfer reaction kinematics using the solenoidal technique is given in Reference [14].

Throughout this section, prime notation will be used to denote quantities of nuclei in the centre-of-momentum (CM) frame of the system with symbols m_i and v_i representing the mass and velocity of each nucleus, respectively. Subscripts, b, t, e and r will be used in place of i to refer to properties of the beam, target, ejectile and residual nucleus, respectively.

3.2.1 Relativistic effects

In this work, data recorded by the Si array were treated relativistically when transforming quantities from the lab frame to the CM frame. The Lorentz factor to transform between lab and CM inertial frames is given by the ratio of the total energy of the system in the lab frame, E_{tot}, to the total energy of the system in the CM frame, E'_{tot} as

$$\gamma_{\mathrm{cm}} = \frac{E_{\mathrm{tot}}}{E'_{\mathrm{tot}}} = \frac{T_{\mathrm{b}} + m_{\mathrm{b}} + m_{\mathrm{t}}}{E'_{\mathrm{tot}}}, \tag{3.1}$$

where T_{b} is the kinetic energy of the beam nucleus in the lab frame. The total energy in the CM frame can be calculated from the invariant mass of the system as

$${E'_{\mathrm{tot}}}^{2} = \sum_i (E_i)^2 - \left|\sum_i (\boldsymbol{p}_i)\right|^2 = (E_{\mathrm{b}} + E_{\mathrm{t}})^2 - |\boldsymbol{p}_{\mathrm{b}} + \boldsymbol{p}_{\mathrm{t}}|^2, \tag{3.2}$$

where $E_{\mathrm{b,t}}$ and $\boldsymbol{p}_{\mathrm{b,t}}$ are the total energy and momentum of beam and target nuclei, respectively. As the target is at rest in the lab frame, this can be expressed as

$$E'_{\mathrm{tot}} = \sqrt{m_{\mathrm{b}}^2 + m_{\mathrm{t}}^2 + 2E_{\mathrm{b}}m_{\mathrm{t}}}. \tag{3.3}$$

The Lorentz factor to transform between the lab and CM frame is therefore

$$\gamma_{\mathrm{cm}} = \frac{T_{\mathrm{b}} + m_{\mathrm{b}} + m_{\mathrm{t}}}{\sqrt{m_{\mathrm{b}}^2 + m_{\mathrm{t}}^2 + 2\left(T_{\mathrm{b}} + m_{\mathrm{b}}\right)m_{\mathrm{t}}}}, \tag{3.4}$$

from which the ratio of the velocity of the CM frame to the speed of light, β_{cm}, can be calculated as

$$\beta_{\mathrm{cm}} = \sqrt{1 - \frac{1}{\gamma_{\mathrm{cm}}^2}}. \tag{3.5}$$

If the lab frame energy of the ejectile is known, the energy of the ejectile in the CM frame, E'_{e}, can be calculated from a Lorentz transformation [99] as

$$E'_{\mathrm{e}} = \gamma_{\mathrm{cm}}\left(E_{\mathrm{e}} - \beta_{\mathrm{cm}}p_{\mathrm{e}}\sin\alpha\right), \tag{3.6}$$

where E_{e} and p_{e} are the energy and momentum of the ejectile, respectively and the lab angle, α, is defined later in Section 3.2.4. All of these can be experimentally measured. After the reaction, the total four-momentum of the system in the CM frame, $\mathbf{P}'_{\mathrm{tot}}$, is the sum of the four-momenta of the residual nucleus, $\mathbf{P}_{\mathrm{r}}$, and the

ejectile, $\mathbf{P}_\mathrm{e}$,

$$\mathbf{P}'_\mathrm{tot} = \mathbf{P}'_\mathrm{r} + \mathbf{P}'_\mathrm{e}. \tag{3.7}$$

Rearranging for $\mathbf{P}'_\mathrm{r}$ and squaring gives

$$(m_\mathrm{r} + E_\mathrm{x})^2 = {E'_\mathrm{tot}}^2 + m_\mathrm{e}^2 - 2\mathbf{P}'_\mathrm{tot} \cdot \mathbf{P}'_\mathrm{e} = {E'_\mathrm{tot}}^2 + m_\mathrm{e}^2 - 2E'_\mathrm{tot}E'_\mathrm{e}, \tag{3.8}$$

where E_x is the excitation energy of the residual nucleus. The excitation energy of the nucleus can be given as

$$E_\mathrm{x} = \sqrt{{E'_\mathrm{tot}}^2 - 2E'_\mathrm{tot}E'_\mathrm{e} + m_\mathrm{e}^2} - m_\mathrm{r}, \tag{3.9}$$

which can be calculated using results from Equation 3.3 and Equation 3.6. The momentum of the ejectile in the CM frame can also be found using Equation 3.6 as

$$p'_\mathrm{e} = \sqrt{m_\mathrm{e}^2 - {E'_\mathrm{e}}^2}. \tag{3.10}$$

With this, an inverse Lorentz transformation between the lab frame and CM frame,

$$E_\mathrm{e} = \gamma_\mathrm{cm}\left[E'_\mathrm{e} + \beta_\mathrm{cm}p'_\mathrm{e}\cos\left(\pi - \theta_\mathrm{cm}\right)\right], \tag{3.11}$$

can be used to calculate the CM emission angle of the ejectile as

$$\theta_\mathrm{cm} = \pi - \cos^{-1}\left(\frac{E_\mathrm{e}/\gamma_\mathrm{cm} - E'_\mathrm{e}}{\beta_\mathrm{cm}p'_\mathrm{e}}\right). \tag{3.12}$$

At the time of writing, the $d(^{212}\mathrm{Rn},p)^{213}\mathrm{Rn}$ reaction at 7.63 MeV/u is the highest kinetic energy of any beam delivered to a HIE-ISOLDE experiment. The total kinetic energy of the beam was 1617.13 MeV, much less than the rest mass of beam nuclei, $m_\mathrm{b} = 197.42$ GeV/c^2. The reaction is therefore very close to the classical regime with $\gamma_\mathrm{cm} = 1.008$ and the remainder of this section will follow a classical description of two-body kinematics to describe transfer reactions.

3.2.2 Two-body kinematics

In a two-body, fixed-target transfer reaction, illustrated in Figure 3.9, the CM frame is defined as the frame in which the momentum of the beam and target are equal such that

$$m_\mathrm{b}\boldsymbol{v}'_\mathrm{b} = m_\mathrm{t}\boldsymbol{v}'_\mathrm{t}. \tag{3.13}$$

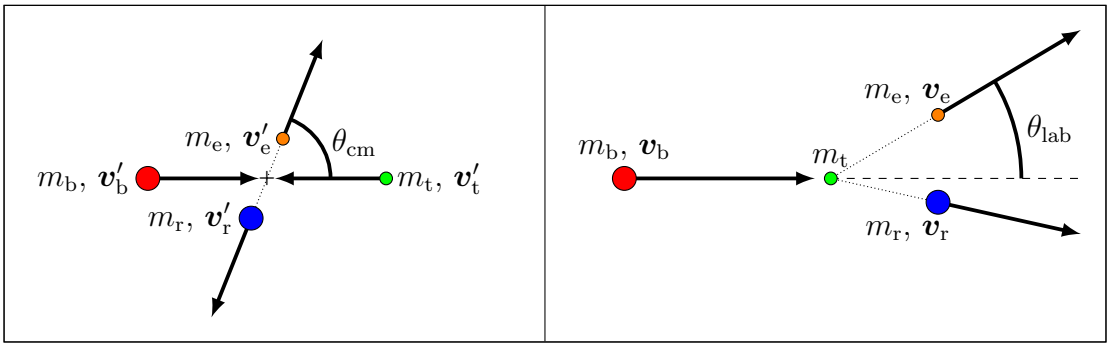


Figure 3.9: Diagram of a fixed-target transfer reaction in the CM frame (left) and lab frame (right). The CM frame moves at a velocity, V_cm, relative to the lab frame.

Similarly, after the reaction,

$$m_\mathrm{e}\boldsymbol{v}'_\mathrm{e} = m_\mathrm{r}\boldsymbol{v}'_\mathrm{r}. \tag{3.14}$$

The velocity of a nucleus in the CM frame can be related to the velocity in the lab frame by

$$\boldsymbol{v}'_i = \boldsymbol{v}_i - \boldsymbol{V}_\mathrm{cm}, \tag{3.15}$$

where $\boldsymbol{V}_\mathrm{cm}$ is the velocity of the CM frame relative to the lab frame, defined as

$$\boldsymbol{V}_\mathrm{cm} = \frac{\sum_i m_i \boldsymbol{v}_i}{\sum_i m_i} = \frac{m_\mathrm{b}}{m_\mathrm{b} + m_\mathrm{t}}\boldsymbol{v}_\mathrm{b} \tag{3.16}$$

for a fixed target reaction. The velocity of the beam in the CM frame is

$$\boldsymbol{v}'_\mathrm{b} = \boldsymbol{v}_\mathrm{b} - \frac{m_\mathrm{b}}{m_\mathrm{b} + m_\mathrm{t}}\boldsymbol{v}_\mathrm{b} = \frac{m_\mathrm{t}}{m_\mathrm{b} + m_\mathrm{t}}\boldsymbol{v}_\mathrm{b}. \tag{3.17}$$

As the target is at rest in the lab frame, it has a velocity in the CM frame of

$$\boldsymbol{v}'_\mathrm{t} = -\frac{m_\mathrm{b}}{m_\mathrm{b} + m_\mathrm{t}}\boldsymbol{v}_\mathrm{b}. \tag{3.18}$$

Before the reaction, the total kinetic energy of the system in the lab frame is equal to the beam energy, T_b. In the CM frame, the initial total kinetic energy of the system, T'_i, is the sum of kinetic energies of the beam and target in that frame,

$$T'_\mathrm{i} = \frac{1}{2}m_\mathrm{b}{v'_\mathrm{b}}^2 + \frac{1}{2}m_\mathrm{t}{v'_\mathrm{t}}^2. \tag{3.19}$$

Using Equation 3.17 and Equation 3.18, this is also

$$T'_\mathrm{i} = \frac{1}{2}m_\mathrm{b}{v_\mathrm{b}}^2\frac{m_\mathrm{t}}{m_\mathrm{b} + m_\mathrm{t}} = \frac{m_\mathrm{t}}{m_\mathrm{b} + m_\mathrm{t}}T_\mathrm{b}. \tag{3.20}$$

After the reaction, the ejectile and residual nucleus are ejected back-to-back at an angle θ_cm, conserving linear momentum. Using Equation 3.15, the kinetic energy

of the ejectile in the lab frame, T_e, can be related to the angle of emission in the CM frame, θ_cm, as

$$\begin{aligned} T_\mathrm{e} &= \frac{1}{2} m_\mathrm{e} \boldsymbol{v}_\mathrm{e}^2 \\ &= \frac{1}{2} m_\mathrm{e} \left(\boldsymbol{v}'_\mathrm{e} + \boldsymbol{V}_\mathrm{cm}\right) \cdot \left(\boldsymbol{v}'_\mathrm{e} + \boldsymbol{V}_\mathrm{cm}\right) \\ &= T'_\mathrm{e} + \frac{1}{2} m_\mathrm{e} V_\mathrm{cm}^2 + m_\mathrm{e} V_\mathrm{cm} v'_\mathrm{e} \cos\theta_\mathrm{cm}, \end{aligned} \tag{3.21}$$

where T'_e is the kinetic energy of the ejectile in the CM frame. The total kinetic energy available to the system will depend on two factors: the Q value and the state populated in the residual nucleus. The Q value is defined as the energy released in a reaction and can be calculated from the total mass difference of nuclei before and after the reaction as

$$Q = \left[m_\mathrm{b} + m_\mathrm{t} - \left(m_\mathrm{e} + m_\mathrm{r}\right)\right] \mathrm{c}^2. \tag{3.22}$$

The system will also lose kinetic energy if the residual nucleus is populated at any energy, E_x, above the ground state. This means the final total kinetic energy in the CM frame, T'_f, is

$$T'_\mathrm{f} = \frac{1}{2} m_\mathrm{e} v'^2_\mathrm{e} + \frac{1}{2} m_\mathrm{r} v'^2_\mathrm{r} = T'_\mathrm{i} + Q - E_\mathrm{x}. \tag{3.23}$$

Rearranging Equation 3.14 for v'_r and substituting into the previous equation gives the velocity of the light ejectile in the CM frame as

$$v'_\mathrm{e} = \sqrt{\frac{2m_\mathrm{r}\left(T'_\mathrm{i} + Q^*_\mathrm{x}\right)}{m_\mathrm{e}\left(m_\mathrm{e} + m_\mathrm{r}\right)}}, \tag{3.24}$$

where $Q^*_\mathrm{x} = Q - E_\mathrm{x}$ has been used.

The angle, θ_cm, ranges from 0° to 180°. The lab-frame angle of emission of the ejectile, θ_lab, and therefore T_e, compared to θ_cm is given by

$$\tan\theta_\mathrm{lab} = \frac{v'_\mathrm{e}\sin\theta_\mathrm{cm}}{v'_\mathrm{e}\cos\theta_\mathrm{cm} + V_\mathrm{cm}} = \frac{\sin\theta_\mathrm{cm}}{\cos\theta_\mathrm{cm} + V_\mathrm{cm}/v'_\mathrm{e}}, \tag{3.25}$$

which depends on how V_cm compares to v'_e. Using Equation 3.16 and Equation 3.20, the CM frame velocity can be given as

$$V^2_\mathrm{cm} = \frac{2m_\mathrm{b}T_\mathrm{b}}{\left(m_\mathrm{b} + m_\mathrm{t}\right)^2} = \frac{2m_\mathrm{b}T'_\mathrm{i}}{m_\mathrm{t}\left(m_\mathrm{b} + m_\mathrm{t}\right)}. \tag{3.26}$$

The ratio of V_{cm} to v'_{e} is then

$$\frac{V_{\mathrm{cm}}}{v'_{\mathrm{e}}} = \sqrt{\left(\frac{m_{\mathrm{b}}m_{\mathrm{e}}}{m_{\mathrm{t}}m_{\mathrm{r}}}\right)\left(\frac{m_{\mathrm{e}}+m_{\mathrm{r}}}{m_{\mathrm{b}}+m_{\mathrm{t}}}\right)\left(\frac{T'_{\mathrm{i}}}{T'_{\mathrm{i}}+Q^{*}_{\mathrm{x}}}\right)}. \tag{3.27}$$

In this equation, the second term under the square root is approximately 1 and the final term is fixed for a given beam energy and excitation energy. In elastic-scattering reactions, the masses of nuclei are the same before and after the reaction and no energy is transferred to the residual nucleus giving $V_{\mathrm{cm}}/v'_{\mathrm{e}} = 1$. From Equation 3.25, in a reaction of this kind, the lab angle of the ejectile is restricted to angles below 90° and transforms as $\theta_{\mathrm{lab}} = \frac{1}{2}\theta_{\mathrm{cm}}$. For transfer reactions, the ratio is mainly governed by the first term in brackets due to the large relative differences in the masses of light nuclei before and after a reaction. From this, different kinematic regimes can be identified depending on the masses of nuclei involved in the reaction.

For a transfer reaction where $m_{\mathrm{b}} \ll m_{\mathrm{t}}$, looking at Equation 3.16, the CM frame of the system is nearly at rest and $V_{\mathrm{cm}} \ll v'_{\mathrm{e}}$. In this regime, the ejectile lab frame energy has a negligible dependence on θ_{cm}. From Equation 3.21 and Equation 3.25, lab frame and CM frame quantities are roughly similar.

If $m_{\mathrm{b}} \gg m_{\mathrm{t}}$, the CM frame velocity increases becoming comparable to v'_{e} causing T_{e} to vary strongly with the cosine of θ_{cm}. For removal reaction such as (p,d), the first term in brackets in Equation 3.27 is approximately 2 and $V_{\mathrm{cm}}/v'_{\mathrm{e}} > 1$. Looking at Figure 3.10, in this regime θ_{cm} becomes double-valued for a given θ_{lab} and ejectiles are always emitted with a parallel component of their lab frame velocity in same direction as the beam, with $\theta_{\mathrm{lab}} < 90°$. In addition reactions such as (d,p), the first term in brackets in Equation 3.27 is approximately 0.5. The final term in brackets deviates from unity by around 16% for the ^{212}Rn(d,p)^{213}Rn reaction at 7.63 MeV/u between excitation energies of 0–5 MeV, therefore $V_{\mathrm{cm}}/v'_{\mathrm{e}} < 1$. In this regime it is possible for ejectiles to have the parallel component of their lab frame velocity opposite to the beam direction, such that $\theta_{\mathrm{lab}} > 90°$.

3.2.3 Challenges in inverse kinematics for a (d,p) reaction

In normal kinematics, θ_{cm} is usually defined relative to the direction of motion of the beam. Measurements of ejectiles tend to be chosen at forward CM angles for (d,p) reactions, corresponding to forward lab angles, as this is where cross sections

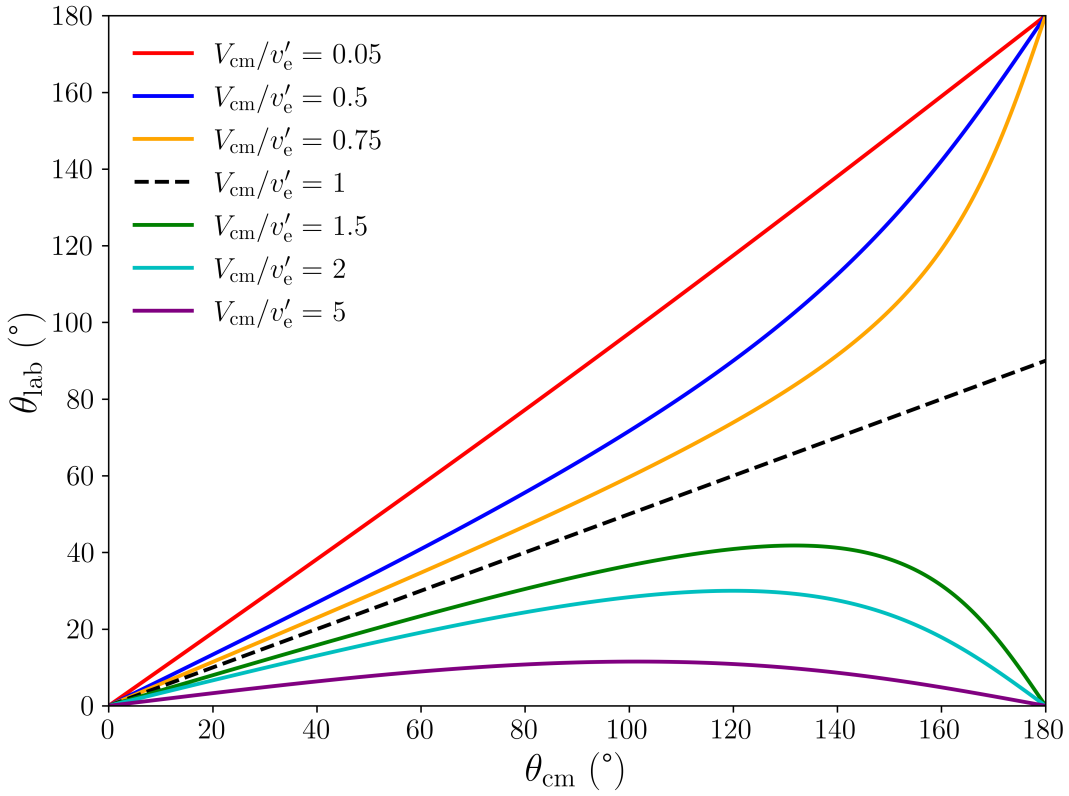


Figure 3.10: The transformation of CM angles to lab angles for different ratios of V_{cm}/v'_e. For the $d(^{212}\text{Rn},p)^{213}\text{Rn}$ reaction at 7.63 MeV/u, $V_{cm}/v'_e = 0.65$ for a proton emitted from the ground state of the residual nucleus. For ratios greater than 1, transformations become double-valued in the laboratory frame. Adapted from Reference [100].

are largest and ℓ-transfers are most distinguishable. However, for a reaction where there are no practical targets available, performed in inverse kinematics, the light nucleus approaches the heavy nucleus with a negative velocity in the rest frame of the heavy nucleus relative to the beam direction. Consequently, to be consistent with normal kinematics, the CM angle of the ejectile in inverse kinematics is usually defined as $\pi - \theta_{cm}$, where θ_{cm} is defined in Figure 3.9. Therefore, for both inverse and normal kinematics, $\theta_{cm} = 0°$ describes a projectile and an ejectile that travels in the same direction before and after the reaction as viewed from the rest frame of the heavy nucleus. Considering this definition of θ_{cm} and looking at Figure 3.10 for a (d,p) reaction, i.e. where $V_{cm}/v'_e < 1$, ejectiles emitted at forward CM angles correspond to backwards angles in the lab frame. From here, any reference to θ_{cm} will mean $\pi - \theta_{cm}$ of the angle defined in the previous section.

For the same initial lab-frame energy per nucleon, the two kinematic regimes are indistinguishable in the CM frame of the system. In normal kinematics, the velocity of the CM frame is close to zero and the system has similar characteristics when viewed from either the lab or CM frame. However, in inverse kinematics,

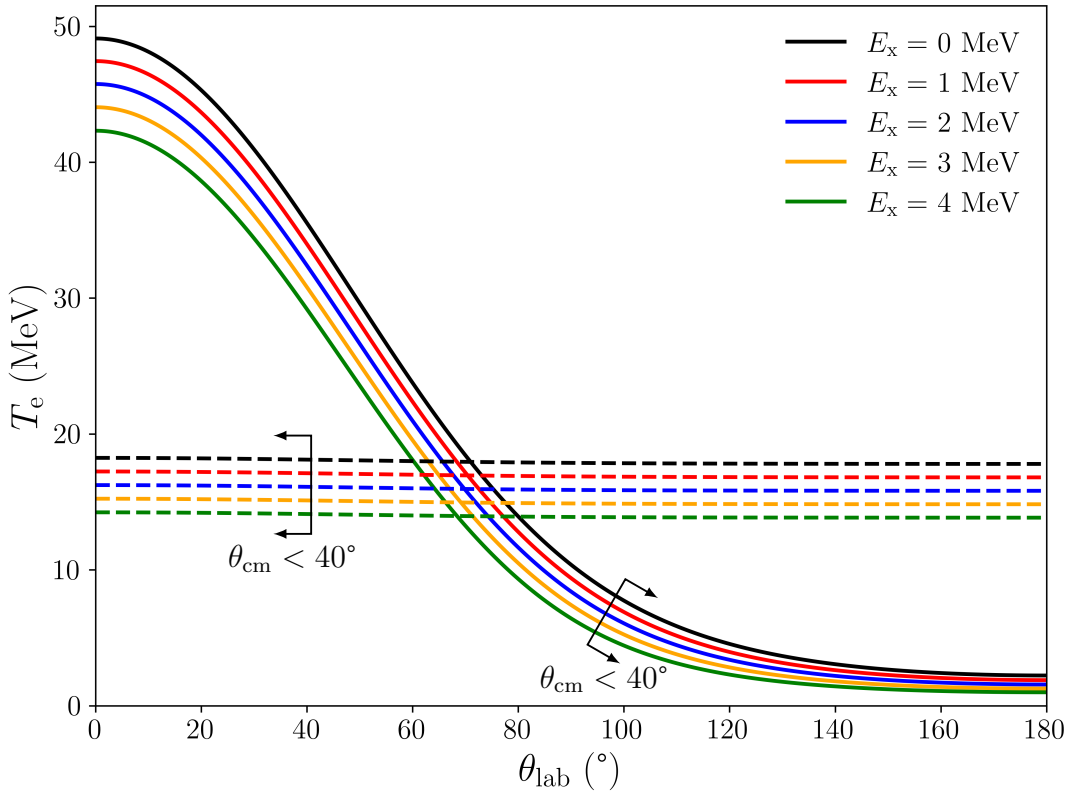


Figure 3.11: Calculations of the kinetic energy of ejectiles as a function of lab angle for different excited states populated in the ^{212}Rn$(d,p)^{213}$Rn reaction at 7.63 MeV/u. Solid lines are energies calculated for inverse kinematics and dashed lines show that for normal kinematics. Approximate regions of forward CM angles have been labelled for both kinematic regimes.

the velocity of the CM frame becomes significant and the behaviour in lab and CM frame are very different. The energy of protons from excited states experience a very significant kinematic compression and a kinematic shift that limit the excitation-energy resolution that can be obtained.

The kinematic compression of excited states can be seen by looking at Figure 3.11. For a reaction in inverse kinematics, as the lab angle of emission for protons emitted from different excited states increases, the energy separation between them, as measured in the lab frame, decreases. The magnitude of compression in inverse kinematics can be calculated by considering the difference between proton lab frame kinetic energies for two states populated in the residual nucleus, ΔT_{kc}. Using Equation 3.21, this can be expressed as

$$\Delta T_{kc} = \Delta T'_e - m_e V_{cm} \Delta v'_e \cos\theta_{cm}, \tag{3.28}$$

where $\Delta T'_e$ and $\Delta v'_e$ are the differences between proton CM frame kinetic energies

CM velocities for two states populated in the residual nucleus*. In this equation, $\Delta T'_{\mathrm{e}}$ and $\Delta v'_{\mathrm{e}}$ are CM quantities and are the same in normal kinematics and inverse kinematics. The reduction in the observed separation of states is therefore governed by V_{cm} and θ_{cm}. From this, the compression of measured states in inverse kinematics is more prominent for forward CM angles, corresponding to large lab angles. As an example for the $d(^{212}\mathrm{Rn},p)^{213}\mathrm{Rn}$ reaction at 7.63 MeV/u, if a proton populates the residual nucleus at $E_{\mathrm{x}} = 1$ MeV and is emitted at an angle $\theta_{\mathrm{cm}} = 40°$, it is separated in lab frame energy by 0.49 MeV from a proton emitted from the ground state at the same angle. This decreases to 0.35 MeV at $\theta_{\mathrm{cm}} = 10°$. Therefore, for an experiment using a fixed-angle detector, the effect of kinematic compression in inverse kinematics increases the difficulty in resolving peaks in an excitation energy spectrum at important experimental angles.

The effect of kinematic shift can be seen by considering the gradient of lines in Figure 3.11. For an experiment using a detector with a fixed angular acceptance between angles θ_1 and θ_2, the energy range of detected ejectiles, ΔT_{ks}, will be proportional to the size of this angular window. In other words,

$$\Delta T_{\mathrm{ks}} = \int_{\theta_1}^{\theta_2} \frac{\mathrm{d}T_{\mathrm{e}}}{\mathrm{d}\theta_{\mathrm{lab}}}\,\mathrm{d}\theta_{\mathrm{lab}}\,. \tag{3.29}$$

In Figure 3.11, it can be seen that the gradient of lines for states populated in inverse kinematics are much greater compared to those in normal kinematics. For the reaction in this work, if a fixed-angle detector with an opening angle of $\Delta\theta_{\mathrm{lab}} = 1°$ was used to detect protons from the ground state, an energy spread of 25 keV would be observed at $\theta_{\mathrm{cm}} = 10°$, increasing to 208 keV at $\theta_{\mathrm{cm}} = 40°$. This has the effect of broadening peaks in an excitation energy spectrum.

ISS has been designed to ameliorate the challenges of inverse kinematics using the solenoidal technique.

3.2.4 Transfer reactions in a solenoid

If a transfer reaction takes place in the magnetic field of a solenoid, where the field axis is aligned with the beam axis, an ejectile with momentum, $\boldsymbol{p}_{\mathrm{e}}$, will be subject to a force perpendicular to magnetic field lines. This will cause it to

* This expression would be $\Delta T_{\mathrm{kc}} = \Delta T'_{\mathrm{e}} + m_{\mathrm{e}} V_{\mathrm{cm}} \Delta v'_{\mathrm{e}} \cos\theta_{\mathrm{cm}}$ for normal kinematics using the definition of θ_{cm} from the previous section. As V_{cm} is close to zero in normal kinematics, the effects of kinematic compression are small.

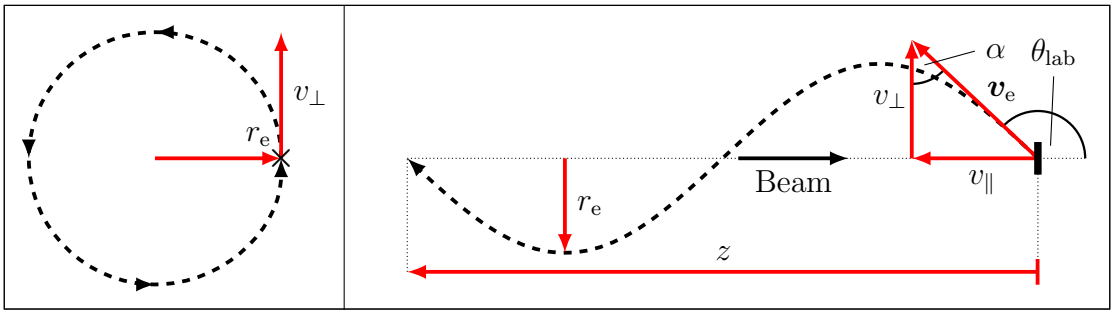


Figure 3.12: The trajectory of a proton in a solenoid following a (d,p) reaction. The beam travels along the central axis of the solenoid. Protons at forward CM angles travel backwards in the lab frame returning to the beam axis after one orbital period. The left figure is looking from one end of the central axis of the solenoid. The right figure is a side-on view. Adapted from Reference [14].

exhibit circular motion in the plane perpendicular to the field direction and move in a helical trajectory as shown in Figure 3.12. The force felt by the ejectile can be expressed as

$$m_e \frac{d\boldsymbol{v}_e}{dt} = q\boldsymbol{v}_e \times \boldsymbol{B} = qv_\perp B = m_e \frac{v_\perp^2}{r_e}, \tag{3.30}$$

where q is the charge of the ejectile, $\boldsymbol{B}$ is the magnetic field strength and $v_\perp$ is the component of the velocity of the particle perpendicular to magnetic field lines. The radius of orbit of the ejectile, r_e, is therefore

$$r_e = \frac{m_e v_\perp}{qB}. \tag{3.31}$$

The orbital period, T_{cyc}, can be related to the angular frequency, ω, by

$$T_{cyc} = \frac{2\pi}{\omega} = \frac{2\pi r_e}{v_\perp}, \tag{3.32}$$

which, by using Equation 3.31, can be also expressed as

$$T_{cyc} = \frac{2\pi m_e}{qB}. \tag{3.33}$$

From Figure 3.12, the component of velocity of the ejectile parallel to the beam axis and the magnetic field lines is

$$v_\parallel = v_e \sin\alpha, \tag{3.34}$$

where α is the angle, $\theta_{lab} - \pi$, in Figure 3.12. Given that the distance an ejectile travels parallel to the beam axis before returning after one cyclotron period, z, is

$$z = v_\parallel T_{cyc}, \tag{3.35}$$

combining Equations 3.33 to 3.35 gives the distance travelled from the target as

$$z = \frac{2\pi m_e v_e}{qB} \sin\alpha = \frac{2\pi p_e}{qB} \sin\alpha. \tag{3.36}$$

The angle, α, is therefore

$$\alpha = \sin^{-1}\left(\frac{qBz}{2\pi p_e}\right). \tag{3.37}$$

The velocity component parallel to the beam axis in the lab frame can be related to the velocity in the CM frame by

$$v_{\parallel} = V_{cm} + v'_e \cos(\pi - \theta_{cm}) = V_{cm} - v'_e \cos\theta_{cm}. \tag{3.38}$$

Combining with Equation 3.35 gives

$$v'_e \cos\theta_{cm} = V_{cm} - \frac{z}{T_{cyc}} = V_{cm} - \frac{qB}{2\pi m_e} z. \tag{3.39}$$

With Equation 3.21[†], the kinetic energy of the ejectile in the lab frame to the distance along the beam axis after an orbital period is

$$T_e = T'_e - \frac{1}{2} m_e V_{cm}^2 + \frac{qBV_{cm}}{2\pi} z. \tag{3.40}$$

In this equation, the first two terms on the right-hand side are constants in a particular reaction to a specific excitation energy of the residual nucleus, as is the velocity of the CM-frame. Therefore, in a solenoidal spectrometer, the lab energy of an ejectile from a particular state in the residual nucleus is linearly related to the distance from the target at which the ejectile returns to the beam axis. A measurement of T_e and z allows excitation energy and ejectile angle to be determined. Kinematic lines exhibiting this linearity in a 2.5 T solenoid are shown in Figure 3.13 for the same reaction as in Figure 3.11.

For an experiment performed in inverse kinematics using a fixed-angle detector, T_e is proportional to $\cos\theta_{cm}$, evident in Equation 3.21. This leads to the problems of kinematic compression and kinematic shift discussed in the previous section. Given the linear relationship of T_e and z in a solenoidal spectrometer, the effect of kinematic compression is completely removed and the separation of measured lab energies from different states becomes proportional to the separation of excited states in the residual nucleus. An analogue of kinematic shift is present, originating

[†] Using the redefinition of θ_{cm}, Equation 3.21 becomes $T_e = T'_e + \frac{1}{2} m_e V_{cm}^2 - m_e V_{cm} v'_e \cos\theta_{cm}$ for inverse kinematics.

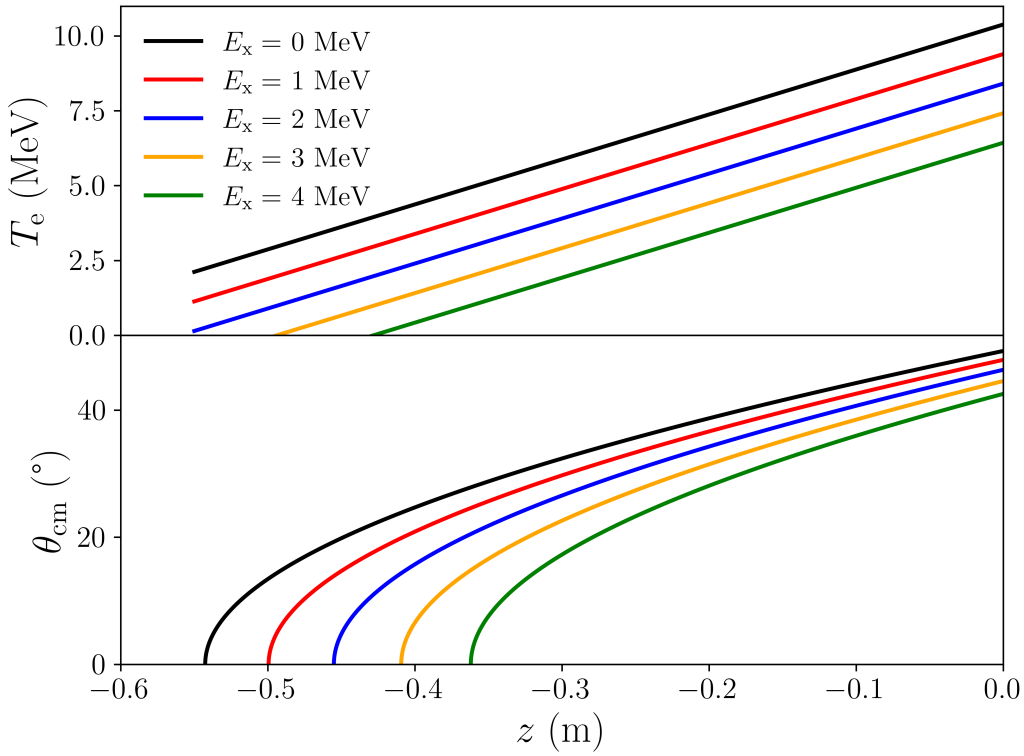


Figure 3.13: Calculations of kinematic lines for a proton populating different excited states in the $d(^{212}\mathrm{Rn},p)^{213}\mathrm{Rn}$ reaction at 7.63 MeV/u in a 2.5 T solenoid. The top figure shows T_e against z for protons returning to the beam axis after one cyclotron period. The bottom figure shows how positions along z map to different θ_{cm}.

from the gradient of kinematic lines giving a measured energy spread of

$$\Delta T_{ks} = \int_{z_1}^{z_2} \frac{dT_e}{dz}\, dz \tag{3.41}$$

for a measurement between z_1 and z_2. From Figure 3.13, this contribution for an on-axis detector with an infinitely small radius will be constant in a solenoid and will depend on the position resolution of the detector used to measure ejectiles. Assuming a position resolution of 1 mm for an on-axis detector, the associated uncertainty in excitation energy for the reaction in this work is approximately 15 keV — smaller than a fixed-angle detector with $\Delta\theta_{lab} = 1°$ discussed in the previous section.

3.2.5 Finite size of the array

The previous section assumes an ejectile is detected at the beam axis. However, from Figure 3.14, it can be seen that with a finite detector, the measured distance,

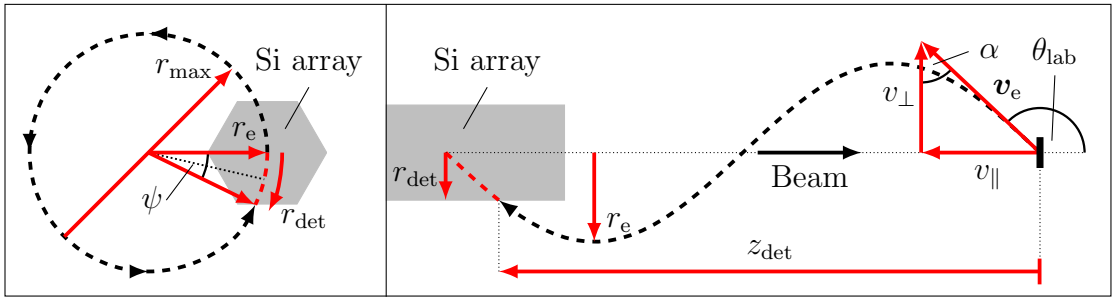


Figure 3.14: A schematic of the trajectory of a proton in ISS with a finite sized detector. The red dashed line shows the trajectory that is blocked by the array. Adapted from Reference [14].

z_{det}, will be shorter than the distance an ejectile would travel before returning to the beam axis after one cyclotron period if the position along the axis could be directly measured. Looking at Figure 3.14 and using Equation 3.31, the maximum distance of an ejectile from the beam axis, r_{max}, can be calculated as

$$r_{max} = 2r_e = \frac{2m_e v_\perp}{qB} = \frac{2p_e}{qB}\cos\alpha. \tag{3.42}$$

Additionally, the radius of the detector, r_{det}, can be related to the angle ψ through

$$r_{det} = 2r_e \sin\left(\frac{\psi}{2}\right) = r_{max}\sin\left(\frac{\psi}{2}\right), \tag{3.43}$$

therefore

$$\psi = 2\sin^{-1}\left(\frac{r_{det}}{r_{max}}\right) = 2\sin^{-1}\left(\frac{qBr_{det}}{2p_e\cos\alpha}\right). \tag{3.44}$$

The distance an ejectile travels parallel to the beam axis is proportional to the angle of the circle that it subtends before hitting the detector [101]. This means that

$$\frac{z - z_{det}}{z} = \frac{2\pi - (2\pi - \psi)}{2\pi} = \frac{\psi}{2\pi}, \tag{3.45}$$

which can be rearranged to

$$z_{det} = z\left(1 - \frac{\psi}{2\pi}\right). \tag{3.46}$$

Using Equation 3.44, this can be given in terms of z as

$$\begin{aligned} z_{det} &= z\left[1 - \frac{1}{\pi}\sin^{-1}\left(\frac{qBr_{det}}{2p_e\cos\alpha}\right)\right] \\ &= z\left[1 - \frac{1}{\pi}\sin^{-1}\left(\frac{\pi r_{det}}{z}\tan\left(\sin^{-1}\left(\frac{qBz}{2\pi p_e}\right)\right)\right)\right], \end{aligned} \tag{3.47}$$

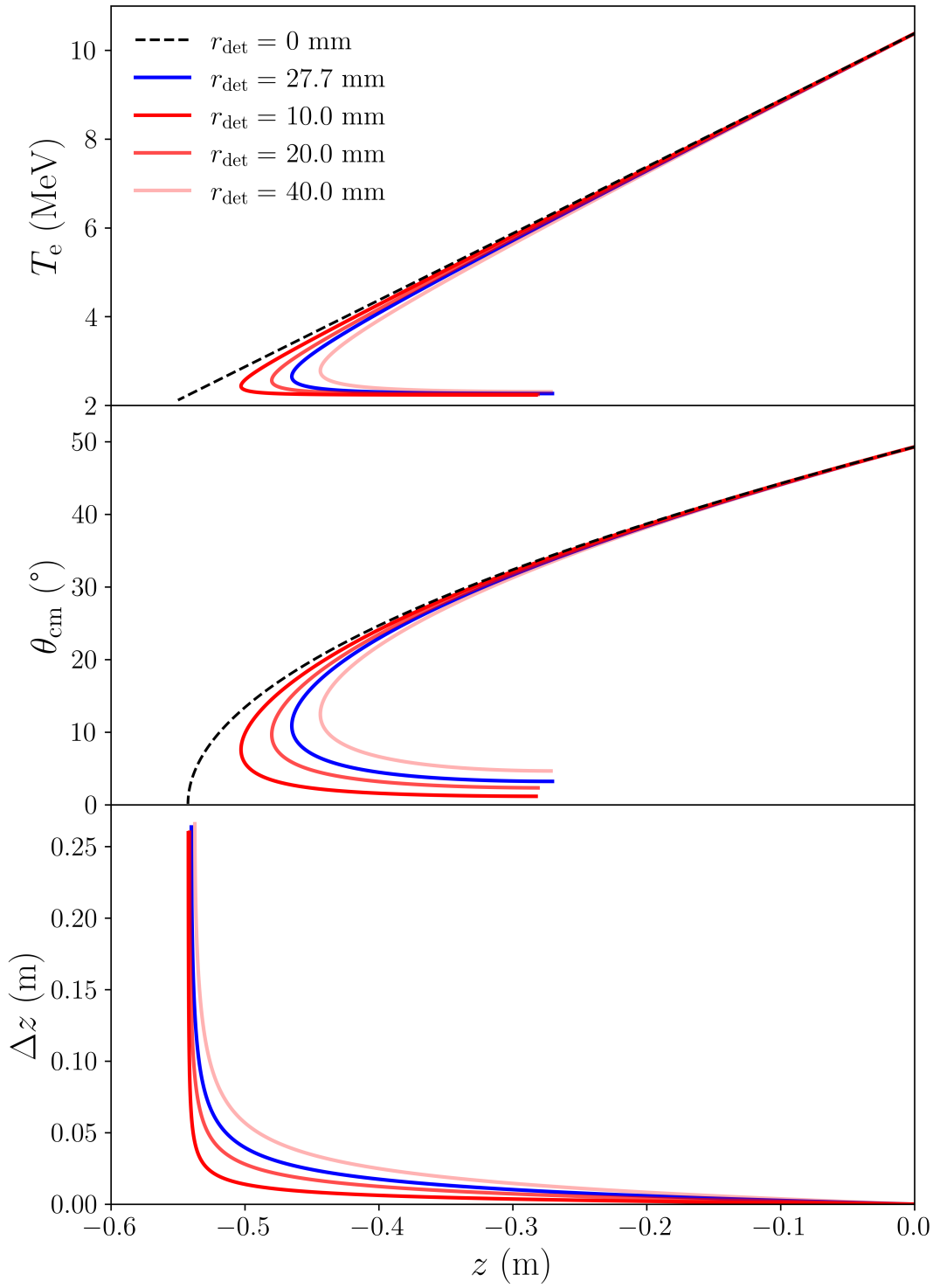


Figure 3.15: The top figure shows T_{e} against z for different detector radii for a proton populating the ground state in the $d(^{212}\mathrm{Rn},p)^{213}\mathrm{Rn}$ reaction at 7.63 MeV/u. The middle figure shows how different positions along z map to θ_{cm} for different detector radii. The bottom figure shows the difference between the measured distance and the distance a proton would travel if the detector had no thickness for different detector radii. The blue line in each figure shows calculations for the average radius of the detector used in this work. More details about this are given in Section 3.3.1.

using Equation 3.36 and 3.37. Apart from z, all of these quantities are known, however a solution cannot to be found analytically. Putting the expression into the form $f(z) = 0$, a solution for z can be found numerically by using a root-finding algorithm. In this work, the Newton-Raphson method was used, and more details are given in Section 4.3. Figure 3.15 shows the effect that increasing r_{det} has on the energy of an ejectile measured as a function of z after populating the ground state of the residual nucleus. As z decreases and θ_{cm} gets smaller, the correction factor needed for a finite detector, $\Delta z = z - z_{\mathrm{det}}$, increases. The kinetic energy of the ejectile becomes double-valued at CM angles below around 15° depending on r_{det}, corresponding to shallower trajectories hitting the detector at smaller absolute distances from the CD_2 target. As the radius of the detector is increased, kinematic 'knees' appear closer to the target, limiting the angular range from which yields of excited states can be measured.

3.3 ISS

The ISS uses an Oxford Instruments OR66 solenoid with an operating field of up to 4 T. The beam, detectors and targets are aligned along the central axis of the magnet bore which has a diameter of 925 mm. The total diameter and length are 2396 and 2732 mm, respectively. A diagram of ISS is shown in Figure 3.16 and a map of the magnetic field, using data recorded in 2018, is shown in Figure 3.17. For the $d(^{212}\mathrm{Rn},p)^{213}\mathrm{Rn}$, the field was set to 2.5 T.

3.3.1 On-axis Si array

A hexagonal double-sided Si strip detector array was used to detect protons ejected in the (d,p) reaction, shown in Figure 3.18. Si detectors are semiconductors, and when radiation interacts with the detector material, electrons are promoted from the valence band to the conduction band creating an electron-hole pair. Through the application of an electric field to the detector material, the electron and the hole undergo a net migration in opposite directions before they are collected at electrodes. The number of electron-hole pairs created is then proportional to the incident energy of the radiation, provided the particle is stopped within the active volume of the detector material. The detector material is doped to create a p-n junction region where incoming radiation generates electron-hole pairs. Si is

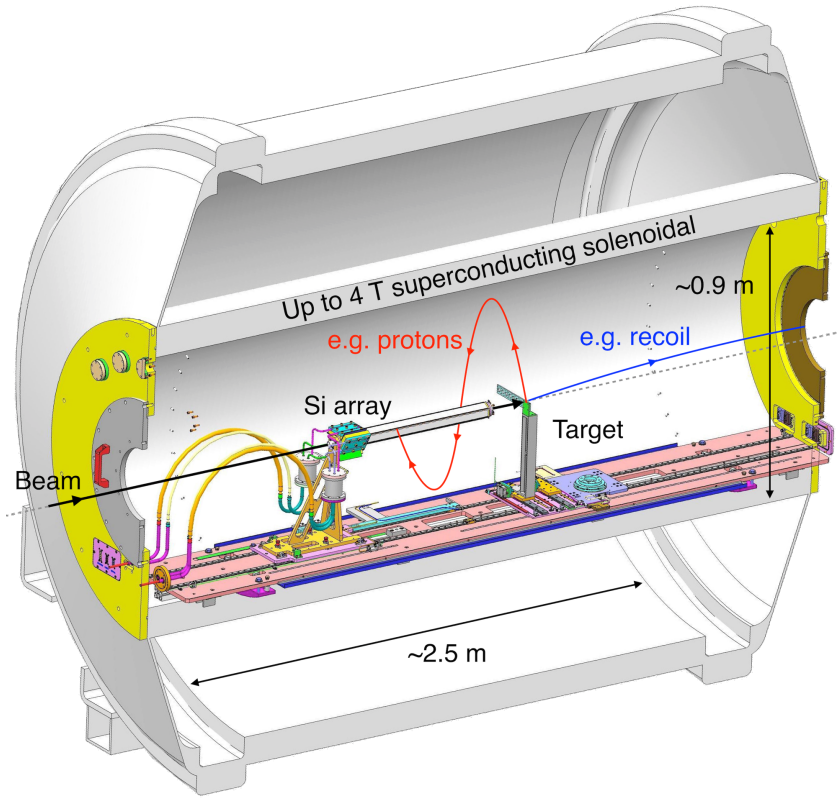


Figure 3.16: The layout of elements in ISS.

tetravalent and doping with pentavalent atoms creates an n-type material where the number of electrons is greater than the number of holes, compared to a pure material. Similarly, doping with trivalent atoms creates a p-type material where the availability of holes is increased compared to the number of free electrons [102].

The array is made up of three modules, each with eight Si wafers. Each wafer has eleven n-side strips running parallel to the beam axis for measuring azimuthal positions of ejectiles. Pairs of wafers are also connected by 128 p-side strips arranged perpendicular to the beam axis allowing the z position of ejectiles to be measured. There are 1800 channels in total and each Si wafer has an area of 3125 mm^2. The total length of the Si on the detector, including 0.95 mm gaps, is 501.5 mm and the geometric efficiency is 94% in the direction parallel to the beam and 70% in the azimuthal direction. The position of the Si array in the bore of the magnet for this work is shown in Figure 3.17. Discussions of transfer reactions in a solenoid in previous sections have assumed a homogenous field however, from Figure 3.17, it can be seen that the field inside the magnet changes along z and radially, and the field is most uniform at the centre of the magnet. Within the region covered by the Si array, the largest field deviation occurs at the largest axial and radial

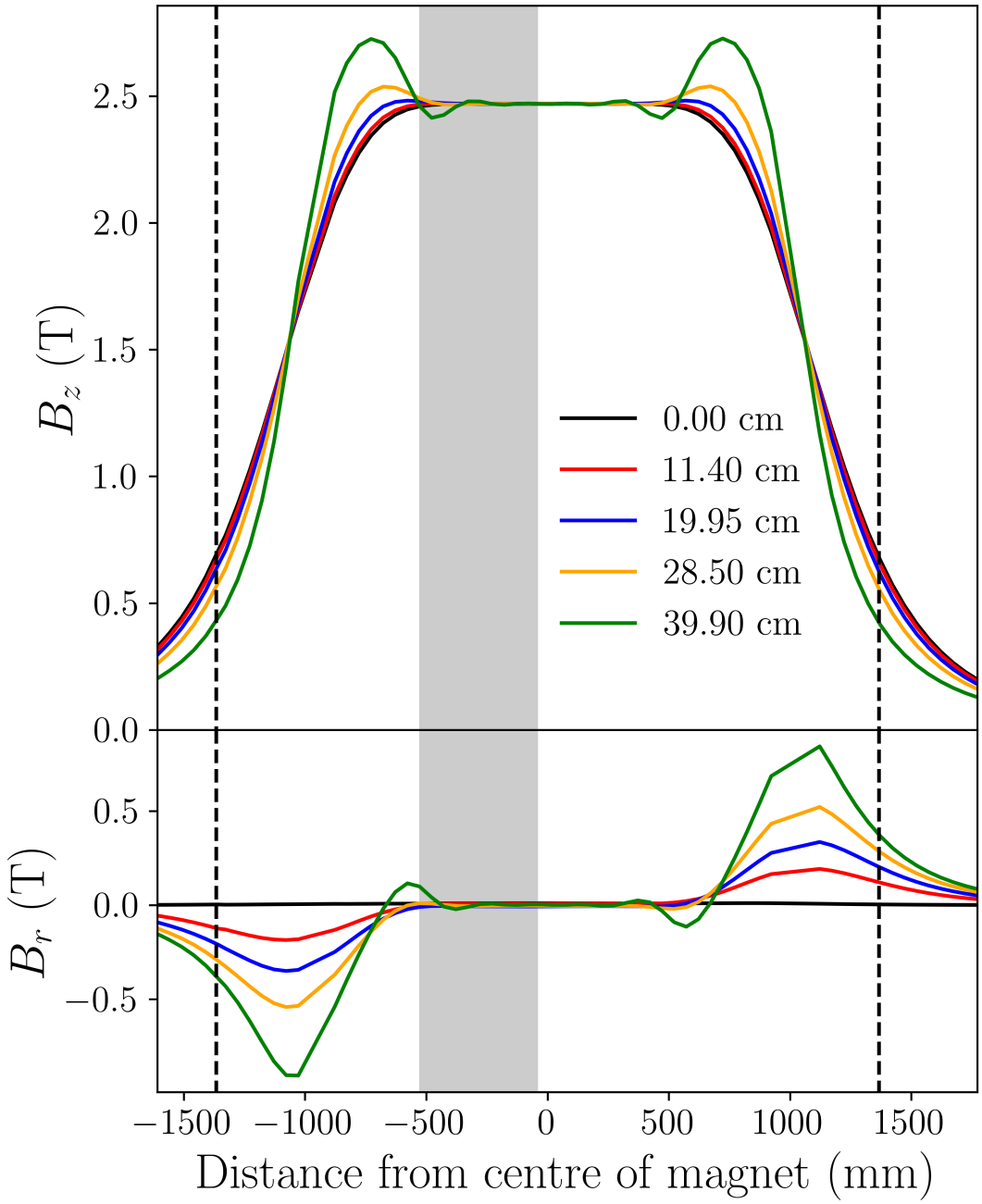


Figure 3.17: A map of axial and radial magnetic field strengths in ISS measured in 2018 when field was set to 2.47 T in the centre of the solenoid. Field strengths were measured at five distances indicated by the figure legend. The grey shaded region shows the approximate position of the Si array in the magnet for the $d(^{212}\mathrm{Rn},p)^{213}\mathrm{Rn}$ experiment. Dashed vertical lines show the region of the bore inside the magnet.

distances and is approximately 2%. This was an oversight during the setup of the experiment and, ideally, the detector position should be more central inside the magnet. At distances less than 400 mm from the centre of the magnet in this region, the deviation is less than 0.1% at all radial distances other than the largest.

The position resolution of the detector in z can be found by differentiating Equation 3.40 as

$$\frac{\mathrm{d}T_\mathrm{e}}{\mathrm{d}z} = \frac{qB\sqrt{2T_\mathrm{b}m_\mathrm{b}}}{2\pi(m_\mathrm{b}+m_\mathrm{t})}. \tag{3.48}$$

The position resolution of the detector in this work was approximately 15 keV/mm a p-side strips have a separation of 0.95 mm. The n-side strips on each Si wafer have a 2-mm pitch allowing the radial distance from the central axis of the detector to be determined on an event-by-event basis. A diagram of the hexagonal detector is shown in Figure 3.19. The smallest distance from the beam axis to the middle n-side strip on a Si wafer, d_0, is 27 mm. The radial distance of each strip from the central axis is then

$$r_\mathrm{det} = \sqrt{d_0^2 + \left(|n-5|\, x_\mathrm{p}\right)^2}, \tag{3.49}$$

where $n = 0, 1, 2, \ldots, 10$ is the strip ID number, labelled in Figure 3.19, and x_p is the strip pitch. Distances from the beam axis to each n-side strip are given in Table 3.1.

Strip ID	r_det (mm)
0	28.8
1	28.2
2	27.7
3	27.3
4	27.1
5	27.0

Table 3.1: Radial distances from the beam axis for each n-side strip. Strip numbers refer to positions labelled in Figure 3.19. Distances for strips 6–10 are symmetric about the central strip.

3.3.2 Downstream detectors

A luminosity detector placed downstream of the target was used to detect elastically scattered deuterons. Using the measured yield in the detector and optical-model calculations of elastic scattering, the product of the target thickness and beam intensity could be extracted allowing angular distributions to be placed



Figure 3.18: A photograph taken from the downstream end of the on-axis Si array [103]. The pipe seen at the end of the array is to block trajectories of ejectiles undergoing multiple orbits. It was not installed in this study.

on an absolute scale. The detector is a Micron Semiconductor S1 double-sided Si detector [104] and photographs are shown in Figure 3.20. It is an annular shape, divided into four sectors covering 2π in the azimuthal direction. It was also shielded by a thick aluminium blocker to limit the acceptance angle of elastically scattered deuterons and to block some deuterons that have undergone multiple orbits. The shield can be seen in Figure 3.20 and dimensions of the detector are given in Table 3.2.

A Faraday cup was also placed on the beam axis between targets and the luminosity detector to monitor beam currents of the unreacted beam and assist with beam tuning.

Detector property	Distance (mm)
Shield-detector distance	13.4
Shield thickness	12.8
Inner radius	24.0
Outer radius	48.0

Table 3.2: Relevant distances and detector dimensions of the luminosity monitor.

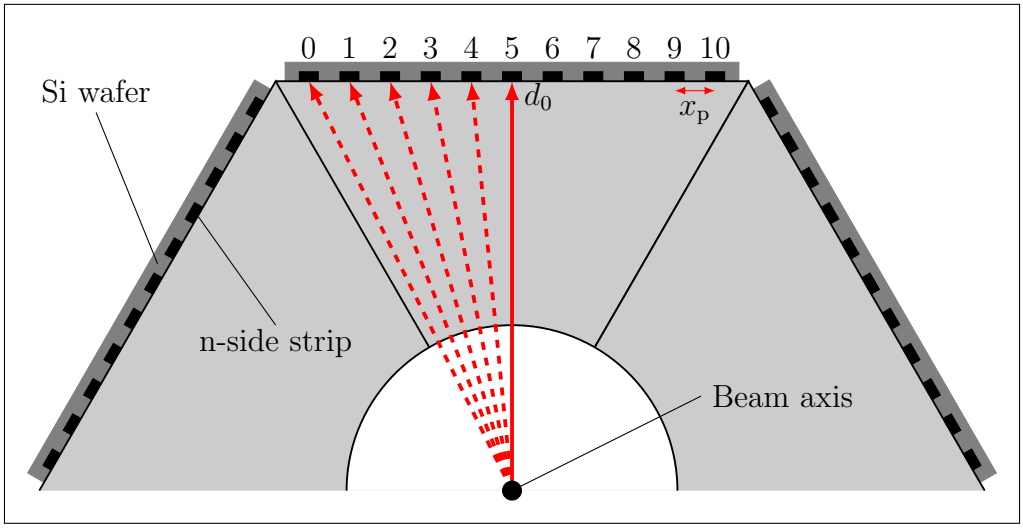


Figure 3.19: A cross-sectional diagram showing half of the hexagonal on-axis Si array. Events have different radial distances depending on where they hit the Si wafer. Strip ID numbers are labelled above each n-side strip for one section of the detector. Dashed red arrows show different radial distances used in the analysis of data which are given in Table 3.1.

3.3.3 Detector positions

The Si array and luminosity detector positions are shown in Figure 3.21 in relation to the CD_2 target. At a distance of 24.9 cm from the target, the angular coverage of the luminosity detector for single-orbit elastically scattered deuterons was $29.18^\circ \leq \theta_{cm} \leq 29.56^\circ$. More details of the method used to calculate the opening angle of the detector are discussed in Section 4.4.1.

The distance of the closest Si wafer on the array from the target was 64.5 mm. For the ground state of ^{213}Rn in this reaction, this covers angles of $2^\circ \lesssim \theta_{cm} \lesssim 46^\circ$ and a total solid angle of 1.21 sr. From Equation 3.42, it can be seen that the maximum radial distance of particles from the beam axis at a given θ_{cm} will be from those with the most momentum and therefore those emitted from the ground state of the residual nucleus. At a CM angle of 46°, protons from the ground state are ejected with a maximum radial distance from the beam axis of approximately 355 mm. From computer-aided design drawings, the structure supporting the target and detectors is a distance of 354 mm [105] from the beam axis. Consequently, some protons were likely blocked by this structure and data from these distances were discarded. This is discussed in Section 4.3.4.

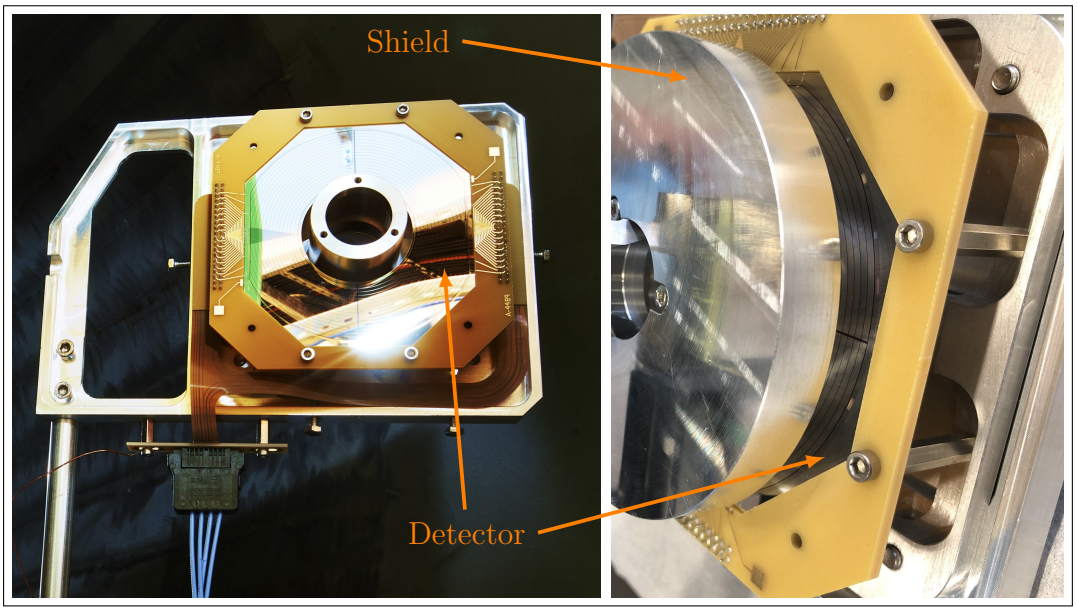


Figure 3.20: The left image shows the luminosity detector assembled without its shield. The right image shows the luminosity detector with the shield installed. The shield limits the opening angle of the detector.

3.3.4 Electronics

Application-specific integrated circuits (ASICs) designed for the R^{3}B experiment at the GSI Helmholtz Centre for Heavy Ion Research (GSI) were used to read out, process and digitise signals from Si strip detectors. More details on their design can be found in Reference [106]. Each module uses six ASICs, with four covering 128 p-side strips each and two covering 44 n-side channels each. A block diagram of the signal processing in an ASIC is shown in Figure 3.22. Each of the 128 channels in the ASIC has a charge-sensitive preamplifier, shaper, peak-hold circuit and comparator. Preamplifiers convert the charge collected in one strip of the detector to a voltage signal with an amplitude proportional to the energy of the ionising particle. Voltage signals are then filtered by CR-RC shaping circuits, reducing the noise of signals and generating pulses of the required shape for peak-hold circuits. The latter maintains the peak amplitude at the input of the analogue multiplexer which receives pulses from all strips connected to the ASIC. A comparator also receives an amplified version of the shaper output and is used as a minimum energy threshold. A channel control unit controls the transfer of signals from the multiplexer to an analogue-to-digital converter (ADC) where signals are converted to a 12-bit number containing amplitude and timestamp information. Signals above this threshold also trigger the read out of neighbouring strips. The

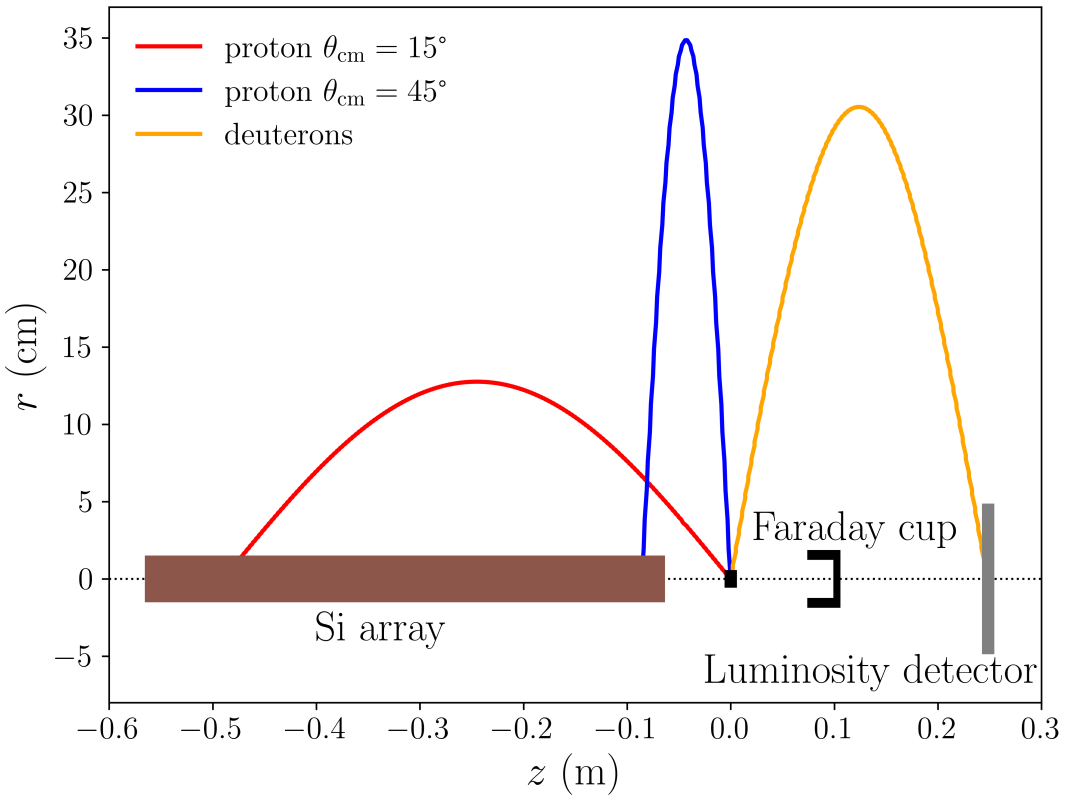


Figure 3.21: A schematic showing positions of detectors in the magnet. Example trajectories of protons emitted in the $d(^{212}\mathrm{Rn},p)^{213}\mathrm{Rn}$ reaction and elastically scattered deuterons in $d(^{212}\mathrm{Rn},d)^{213}\mathrm{Rn}$ reaction are also shown.

ASICs are controlled and read out using FPGA mezzanine cards.

Signals generated in the luminosity detector were fed into mesytec MSI-8 [107] preamplifiers before being sent to CAEN V1725 digitisers [108]. The digitiser has multiple acquisition parameters which control the extraction of information from detector pulses, shown in Figure 3.23. The digitiser continuously samples the input signal from the detector and estimates a baseline by averaging samples in a programmable window size. When the input signal crosses the threshold value, an event is triggered and the signal is delayed by a programmable number of samples, called the pre-trigger window. This allows the signal to be integrated before the threshold in the gate offset region. A long gate for integrating the signal is then generated, from which energies of the ionising particle can be determined. For the duration of this process, a trigger hold-off window is active which prevents other signals from triggering the digitiser. Values of digitiser parameters used are given in Table 3.3.

A common 62.5-MHz clock was used to ensure time synchronisation between sig-

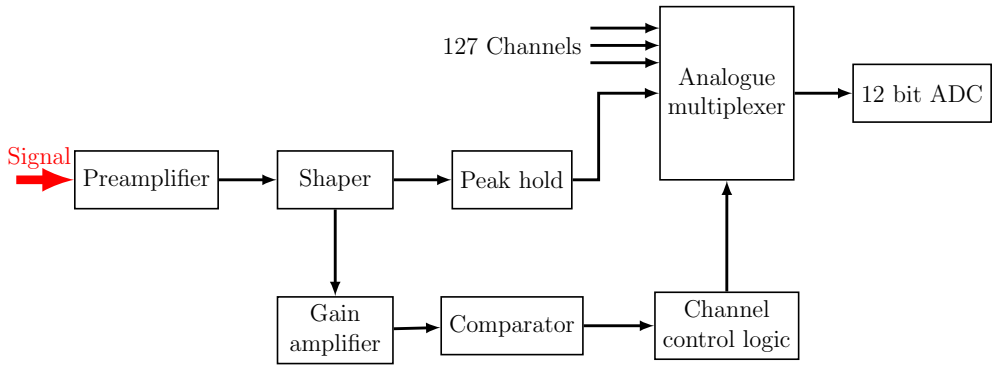


Figure 3.22: A block diagram of signal processing in an ASIC.

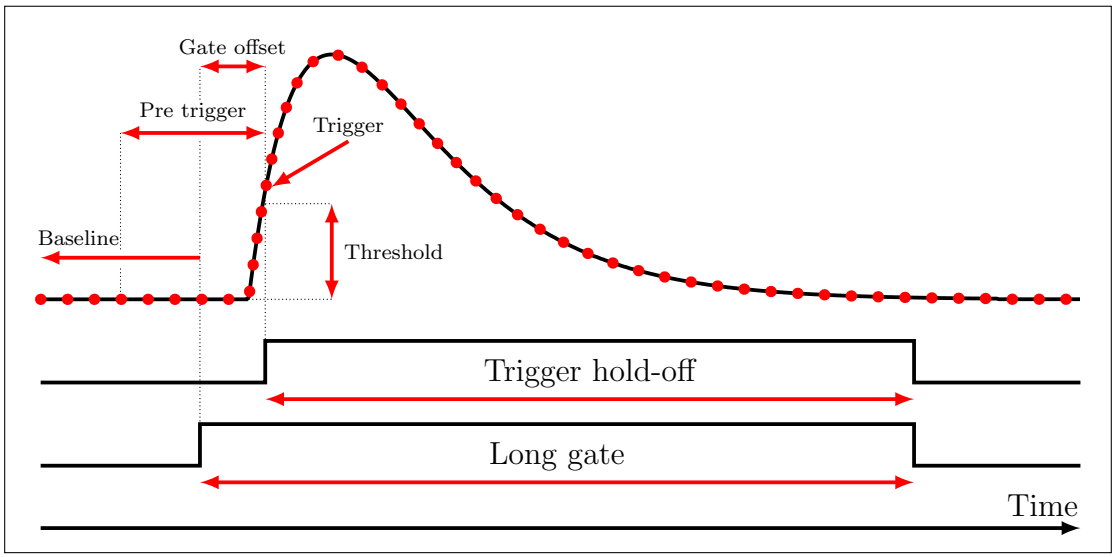


Figure 3.23: A diagram showing data acquisition parameters for a typical waveform in the luminosity monitor data acquisition system. Red dots indicate sample points. The trigger fires when the signal cross the threshold value. Values for parameters used during the experiment are given in Table 3.3.

nals from the Si array and luminosity detector.

3.3.5 Targets

Targets used in this work were made from deuterated polyethylene (CD_2) and were mounted on an eight-by-eight target frame. This was a typewriter-type target ladder which moved down to a new row after reaching the end column and making contact with a pusher. A photograph of the frame is shown in Figure 3.24. Targets were produced at Argonne National laboratory using the method outlined in Reference [109]. A mixture of CD_2 powder is heated above its melting temperature and dissolved into a solvent. The heated solution is poured onto a casting surface and cooled so that the solvent evaporates, leaving a CD_2 film. The film is

Data acquisition parameter	Samples	Time (ns)
Baseline	1024	4096
Pre trigger	10	40
Gate offset	6	24
Long gate	800	3200
Trigger hold-off	794	3176

Table 3.3: Data acquisition parameter settings for the luminosity detector. The data acquisition system samples the waveform every 4 ns. Parameters are summarised in Figure 3.23.

then placed in a laboratory oven at 145 °C for 30 minutes until visibly clear. Thin films are removed from the casting surface by rapid cryogenic freezing followed by mechanical release.

Across the experiment 17 targets were used to prevent damage due to the large mass of the ^{212}Rn beam. An α-particle source was also mounted on this frame and used to calibrate detectors and was not installed in the photograph shown in Figure 3.24. Target thicknesses were approximately 125 µg/cm^2.

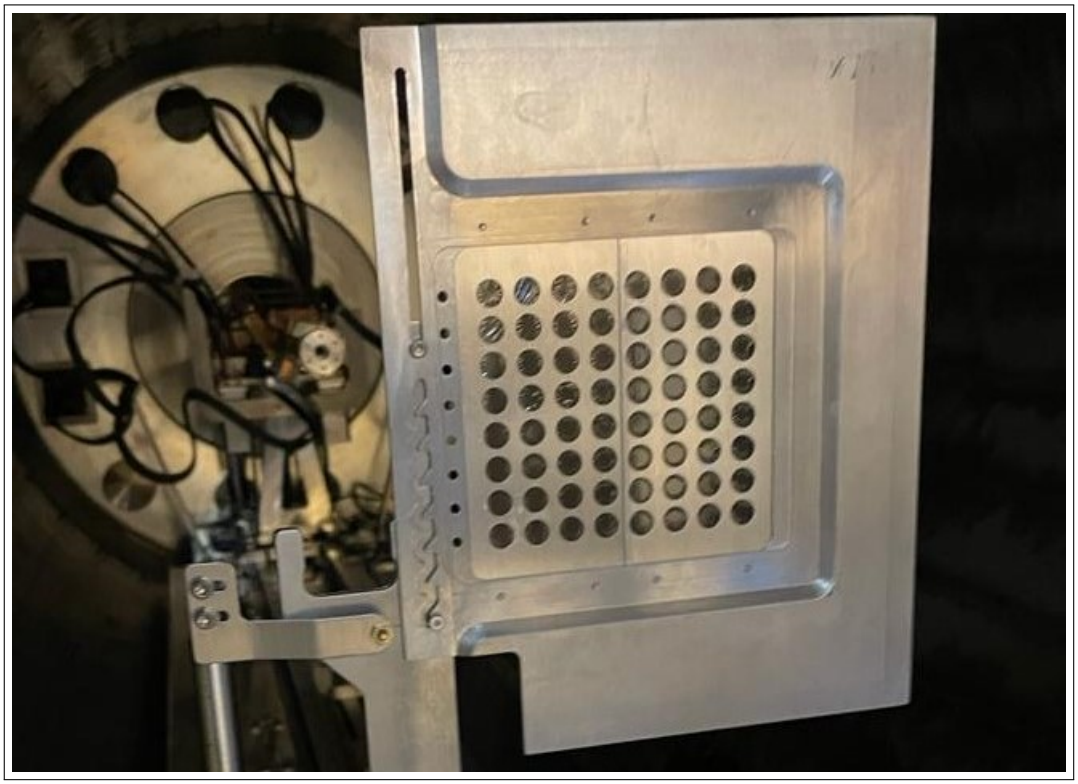


Figure 3.24: A photograph of the target ladder used to hold CD_2 targets. A mechanical mechanism is used to drop the ladder from one row to another and an electronic actuator moves the ladder to position different targets within each row.

Chapter 4

Analysis of data from the $d(^{212}\mathrm{Rn},p)^{213}\mathrm{Rn}$ reaction

This chapter discusses details of analysis methods applied to data from the $d(^{212}\mathrm{Rn},p)^{213}\mathrm{Rn}$ reaction at ISOLDE Solenoidal Spectrometer (ISS), from the calibration of detectors to the extraction of absolute cross sections and spectroscopic factors of excited states. The method used to determine assignments of ℓ-transfers to excited states in the residual nucleus is also described. Additional details of the sort code used for much of this analysis can be found in Reference [110].

4.1 Detector calibration

The first step in the analysis is to ensure all detectors are calibrated in terms of energy. Detectors were calibrated using an α source consisting of four different isotopes. Energies of α particles, E_α, were linearly fitted to peak centroids from analogue-to-digital converter (ADC) values, C, in the form

$$E_\alpha = aC + b, \tag{4.1}$$

where a and b are calibration parameters. Information on energies of α particles emitted from each isotope are given in Table 4.1.

When fitting data, the effective variance method [111] was used to account for

Radionuclide	α-particle energy (keV)
^{148}Gd	3182.69 ± 0.02
^{239}Pu	5148.31 ± 0.34
^{241}Am	5478.62 ± 0.14
^{244}Cm	5795.04 ± 0.05

Table 4.1: Table of α-particle energies used to calibrate the luminosity detector and the on-axis Si array from References [112, 113, 114, 115]. Values for ^{239}Pu, ^{241}Am and ^{244}Cm are averages of α-particle energies weighted by intensity from decay branches within 100 keV of the main decay branch.

uncertainties in both ADC channel peak centroids and energies of alpha particles being comparable in magnitude. In this method, uncertainties in x values, σ_{x}, and y values, σ_{y}, are used to calculate the chi-squared as

$$\chi^2_{\mathrm{eff}} = \sum_i \left(\frac{(y_i - f(x_i))^2}{\sigma^2_{\mathrm{y}_i} + (\sigma_{\mathrm{x}_i} f'(x_i))^2} \right), \tag{4.2}$$

where x_i and y_i are data point coordinates, $f(x)$ is the function to be fitted and $f'(x)$ is the derivative of $f(x)$. The best fit of data occurs using parameters that give the minimum of this sum.

4.1.1 Array calibration

An example of α-particle data measured in a p-side channel by the Si array before the experiment is shown in Figure 4.1. Gaussian functions with a constant background were fitted to the four peaks and centroid values were extracted. From the z_{det} measured, the angle of emission of α particles were calculated using kinematics described in Section 3.2. This allowed the energy lost in the dead layer of the Si to be determined. Additionally, pulse-height corrections (PHCs) were applied to energy loss corrected energies of α particles compensate for differences in the number of charge carriers produced by protons from the (d,p) and alphas of the same energy. After applying these corrections, an expected detected energy was used for the calibration. This procedure was repeated for the 1800 channels across the array and more details on these corrections are given in Section 4.3.2 and Section 4.3.3. To ensure complete coverage of the Si array, data was recorded at two distances from the target as measured to the nearest Si detector edge: 124.5 mm and 184.5 mm. Calibrated data for a p-side application-specific integrated circuit (ASIC) at each distance is shown in Figure 4.2.

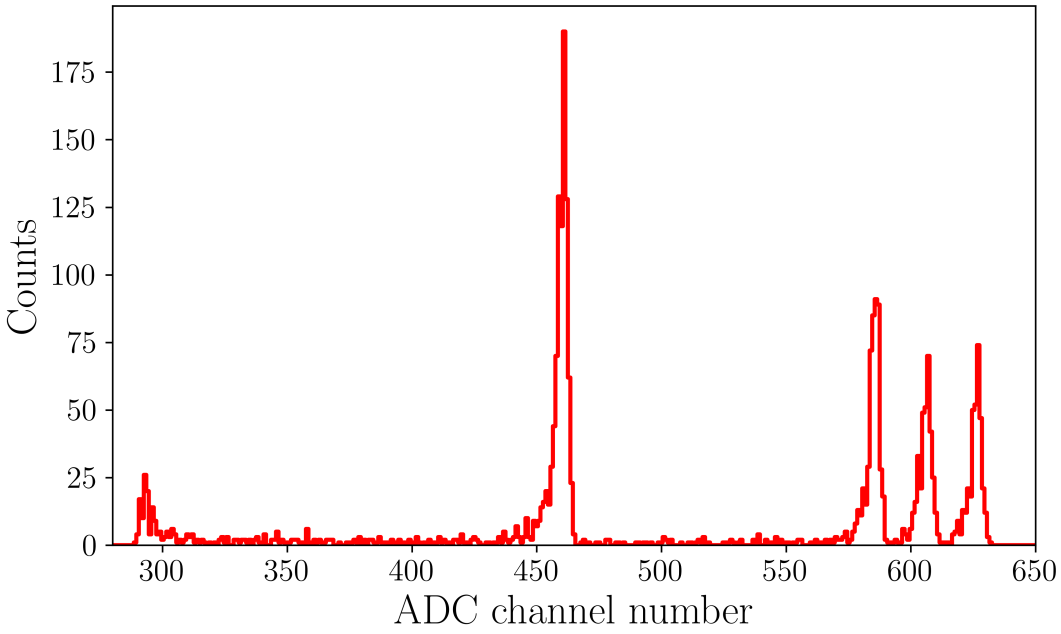


Figure 4.1: α particle data used to calibrate channel 0 of ASIC 5 in Module 0 of the array. The distance of the closest point of the Si array from the target was 124.5 mm when collecting these data. The feature around channel 290 is from electronic noise.

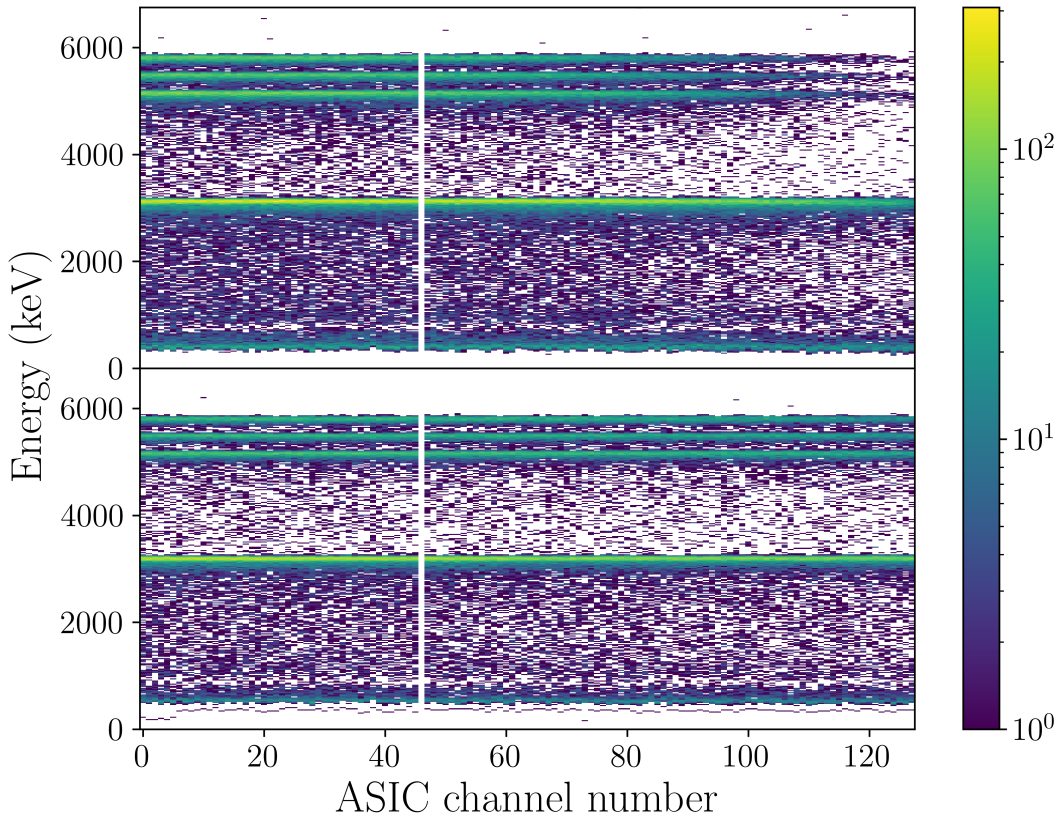


Figure 4.2: Calibrated data for channels of ASIC 5 in Module 0 of the array. The top figure is with the closest point of the array 124.5 mm from the target. The bottom figure is at a distance of 184.5 mm from the target.

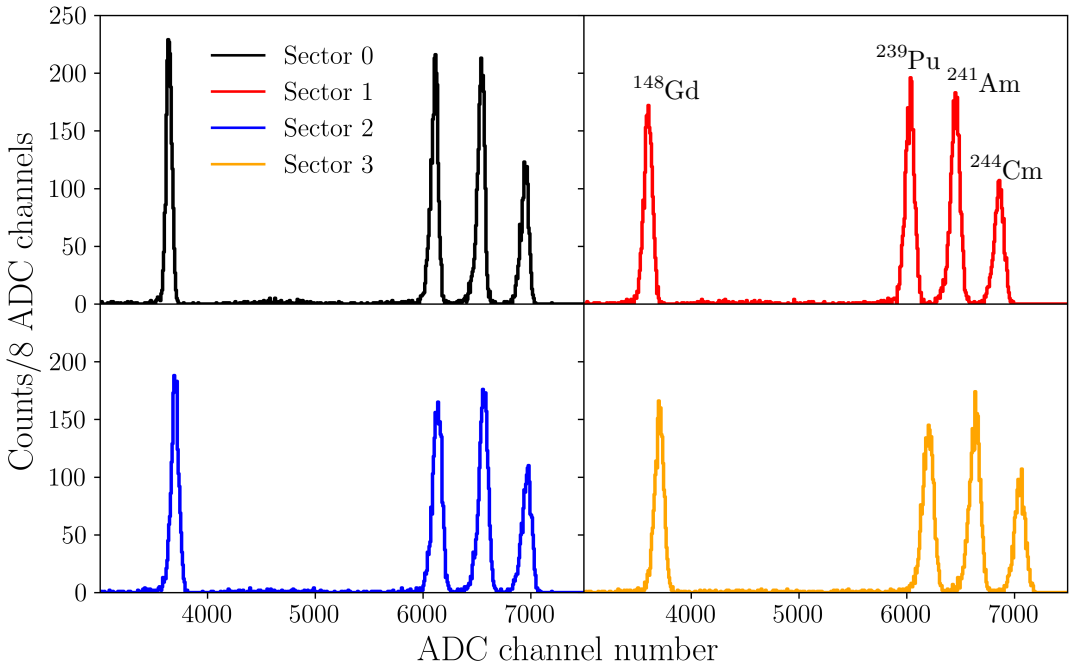


Figure 4.3: Uncalibrated data from the quadruple α-particle source used to calibrate each sector of the luminosity detector. For one sector, each peak has been labelled with the radionuclide from which α particles decayed.

4.1.2 Luminosity detector calibration

Data from α particles measured in each sector of the luminosity detector are shown in Figure 4.3. Peaks were fitted with Gaussian functions and linear backgrounds from which centroid values were used to calibrate each sector using Equation 4.1. Uncertainties on peak centroids ranged from 0.6 to 1.5 channels. As data from this detector was only used to extract absolute cross sections, a precise energy calibration was not necessary and no dead layer energy losses or PHCs were applied.

4.2 Timing conditions

An event in the Si array was selected to reconstruct the excitation energy of the residual nucleus based on certain timing criteria. These included satisfying timing conditions between overlapping p-side and n-side strips, and being within a defined time from a trigger signalling the release time of ions from the electron beam ion source (EBIS).

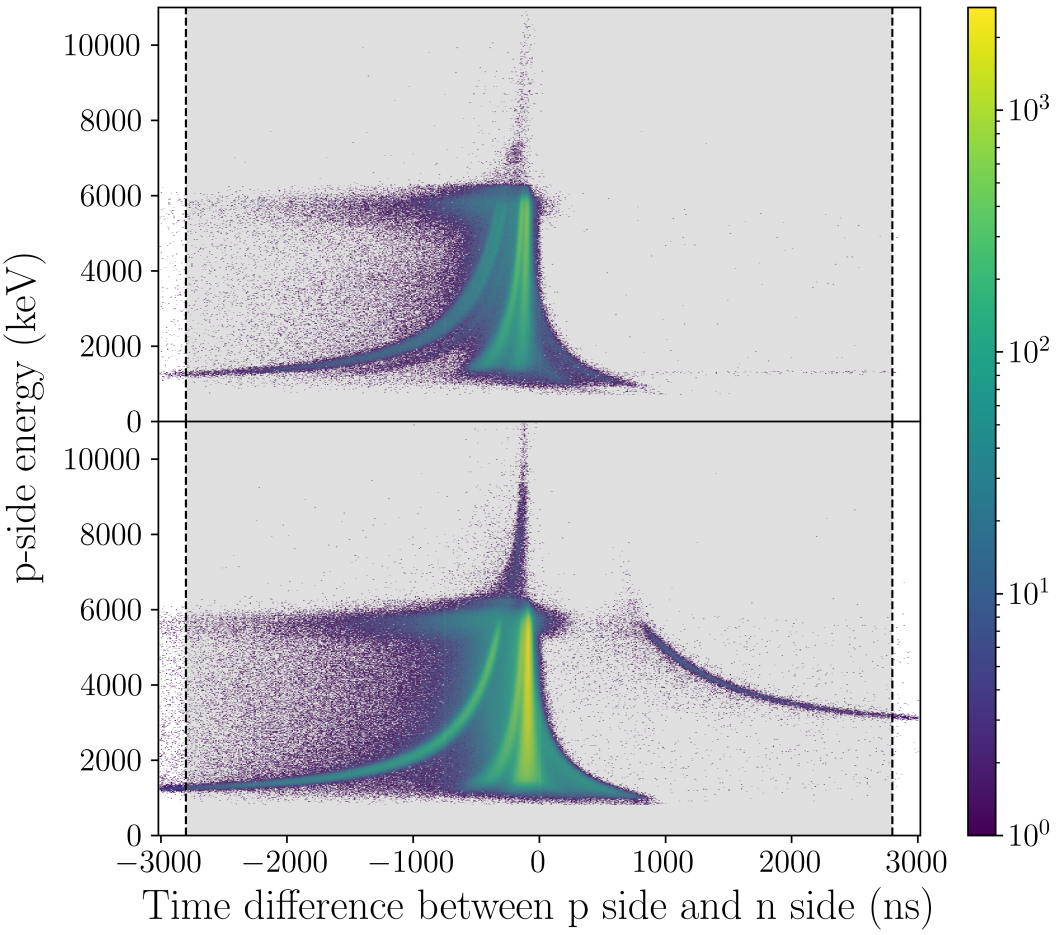


Figure 4.4: The time difference of events between p-side and n-side channels. The top figure shows data from Row 2 in Module 1 of the Si array. The bottom figure shows data from Row 3 in Module 2. Data from all runs is included. Different time walk curves are from changing ASIC energy thresholds during the experiment. Grey regions with dashed lines show the p-side and n-side coincidence time window.

4.2.1 Coincidence time window for p sides and n sides

Events in the Si array were accepted if a signal was measured in a p-side strip and a corresponding n-side strip within a defined time window, reducing unwanted events from triggering on electronic noise in the detector. An energy-dependent and ASIC-energy-threshold-dependent time walk was observed between n-side and p-side strips, and energy threshold levels on ASICs were altered multiple times throughout the experiment to reduce unwanted noise. This changed the behaviour of the time walk and the effects of this can be seen in Figure 4.4. To include all events, a p-side and n-side coincidence time window of $\Delta t_{\mathrm{pn}} = 2800$ ns was used. A p-side event was then accepted if another event in an overlapping n-side strip was detected within $\pm\Delta t_{\mathrm{pn}}$. Data collected with this condition applied is shown

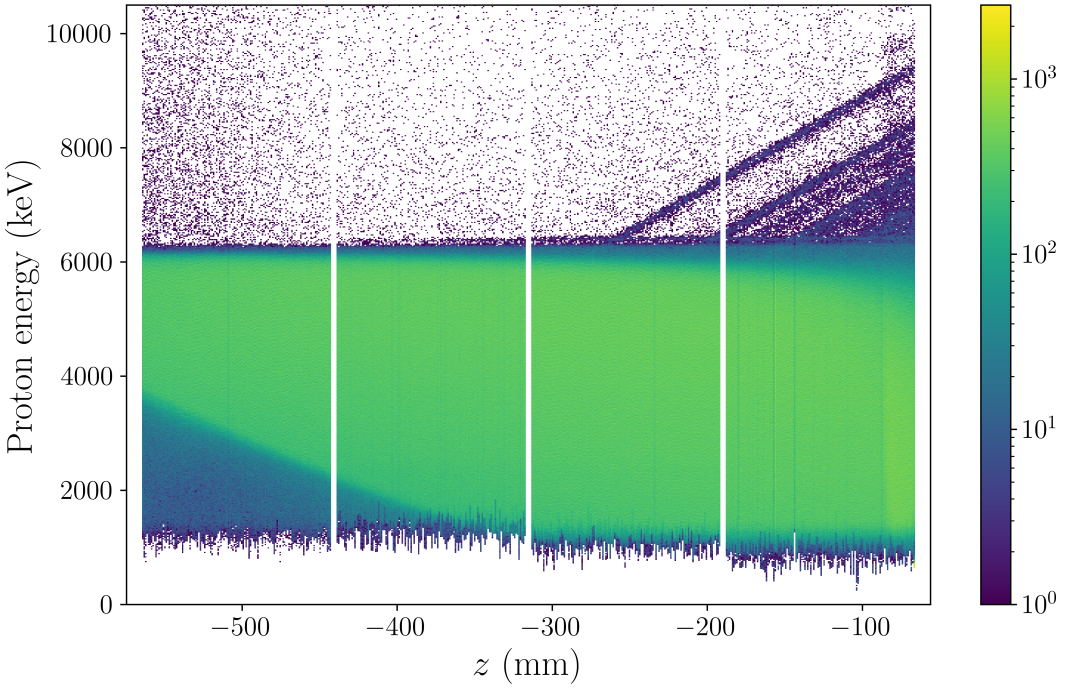


Figure 4.5: Measured proton energy against z with p-side and n-side timing cuts applied.

in Figure 4.5. The broad continuum of counts below ~ 6 MeV originates from the α-decay of ^{212}Rn beam particles scattered within ISS.

4.2.2 Background subtraction

After p-side and n-side coincidence verification, the background of α particles was reduced with the help of a timing signal associated with the release of ions from the EBIS. The number of counts detected in the luminosity detector as a function of time from this signal for both extraction modes can be seen in Figure 4.6. From this, a beam-on time window to accept Si array events was defined as 1.04 ms for both extraction modes. In addition to this, a total beam-off time window of 68.96 ms was selected. Events recorded in the beam-off time window were scaled by the ratio of the beam-on to beam-off times and used to perform a background subtraction of beam-on data. The application of the beam-on window reduces, but does not exclude α decays, as seen in Figure 4.7. The subtraction of data using the beam-off window clearly removes these events.

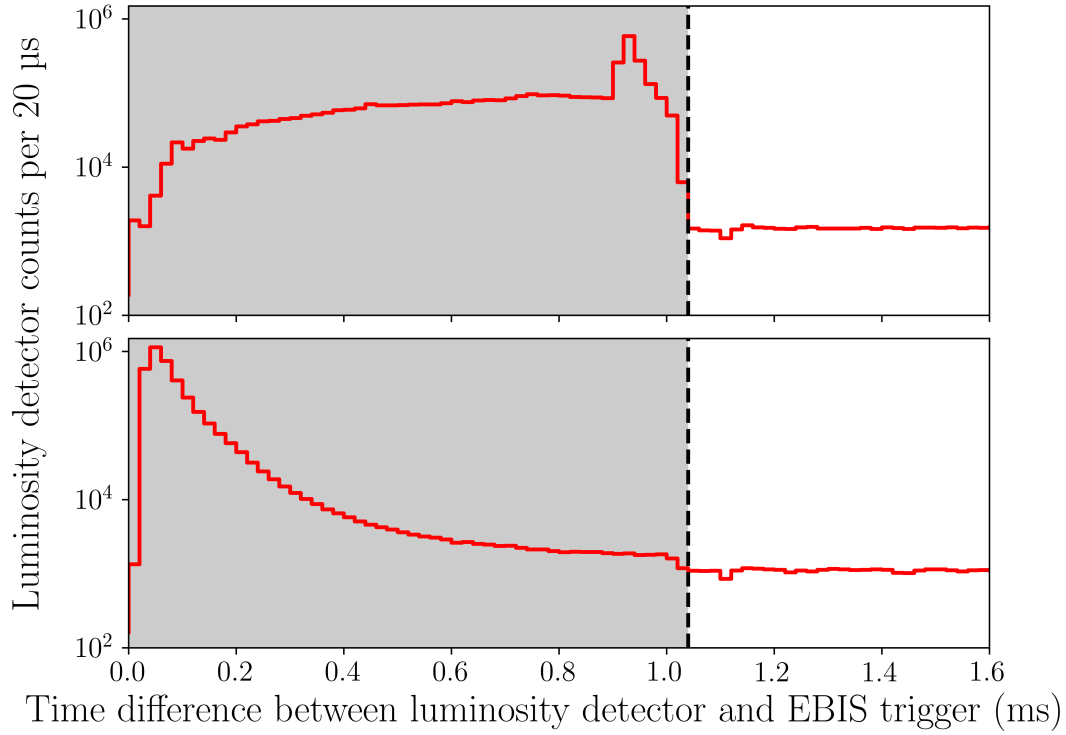


Figure 4.6: Counts in the luminosity detector as a function of time from the EBIS trigger signal. The top figure shows data from all runs using the slow extraction mode. The bottom figure is that using data from the fast extraction mode.

4.3 Excitation energies

When reconstructing the excitation energy of the residual nucleus from the measured proton energy, several energy corrections were applied. These accounted for energy losses of protons and beam nuclei in the CD_2 target material, energy losses of protons and α particles in the Al dead layer of the Si array and PHCs between protons and the α-source calibration. Stopping powers, $S(E)$, for charged particles moving through a material were taken from the software package, Stopping and Range of Ions in Matter (SRIM) [116]. With these, the energy loss, ΔE, was calculated from

$$\Delta E = \int_0^d S(E)\,\mathrm{d}x\,, \tag{4.3}$$

where d is the distance the charged particle travelled through the material.

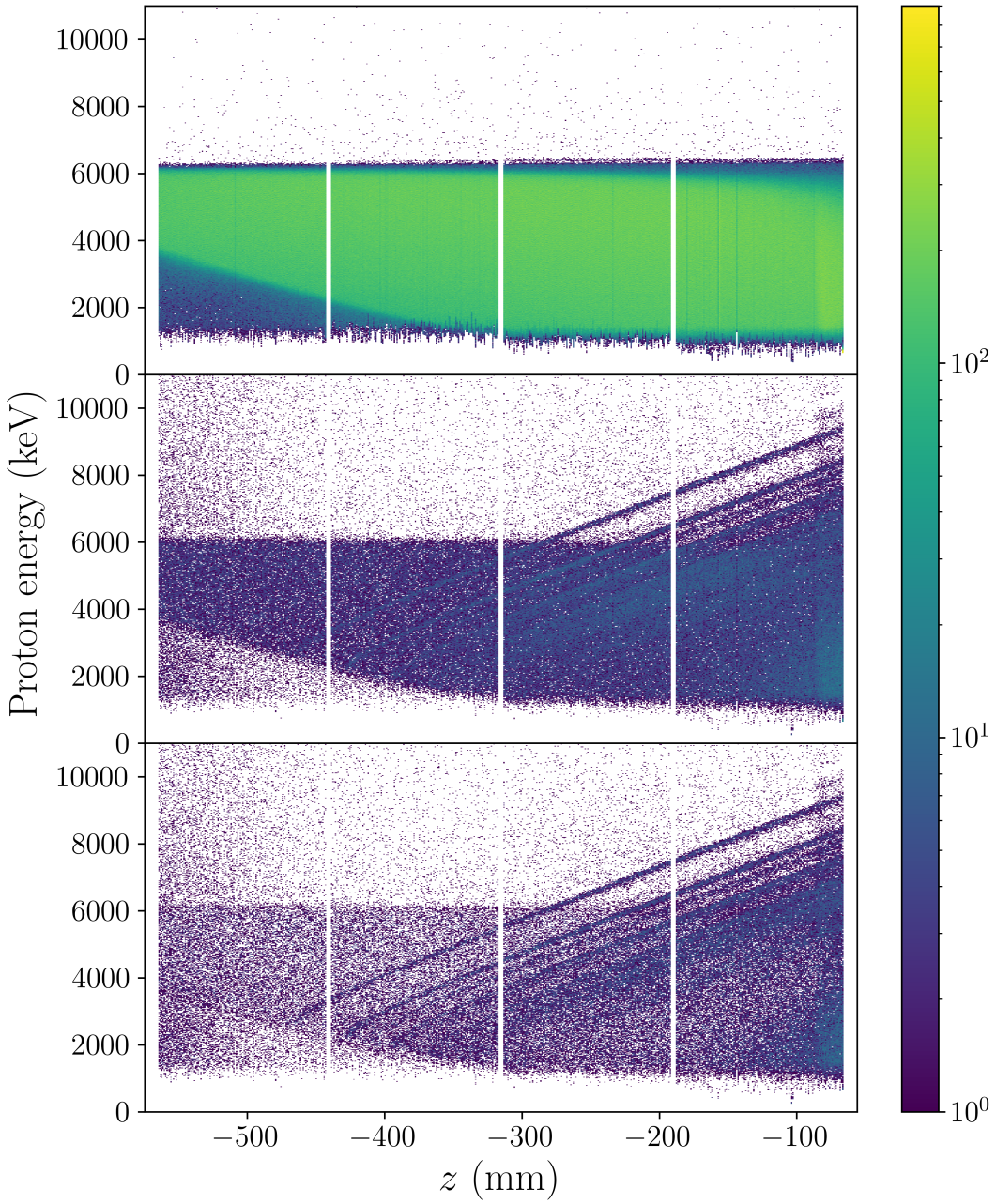


Figure 4.7: The top figure shows data collected during the beam-off time window for all runs. The middle figure shows data collected for the beam-on time window for all runs. The bottom figure is a subtraction of data in the beam-off time window from data collected in the beam-on time window, where beam-off data has been weighted by the ratio of the beam-on to beam-off times.

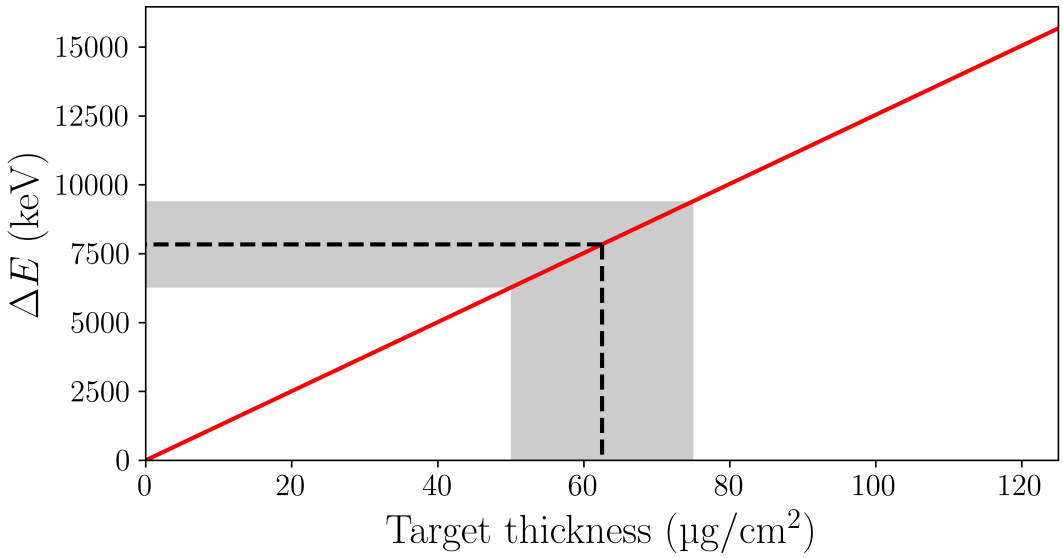


Figure 4.8: The energy loss of ^{212}Rn in CD_2 with an initial energy of 1617.13 MeV. The black dashed line shows the energy lost at 62.5 µg/cm^2 corresponding to half the nominal target thickness. The grey band shows ±20% the target thickness.

4.3.1 Beam-energy losses

The energy loss of the beam in CD_2 was calculated assuming beam nuclei traveled through 50% of the target material before interacting with target nuclei. A total of 17 different CD_2 targets were used throughout the experiment and each target was labelled with a thickness and assigned an estimated uncertainty of 10–15%. Additionally, target material was assumed not to be perfectly uniform. Considering this and using the labelled target thickness values, a nominal target thickness of 125 µg/cm^2 was used for energy loss calculations with an estimated uncertainty of 20%. Energy loss calculations of beam nuclei in the target are shown in Figure 4.8. With a kinetic energy of 1617.13 MeV, the energy loss of the beam through 50% of the target is 7.83 MeV, giving a beam energy value of 1609.30 MeV used in calculations to reconstruct excitation energies of the residual nucleus.

4.3.2 Pulse-height corrections

It has been shown that there is a non-linear response of pulse heights in Si detectors when measuring light charged particles [117, 118, 119] and, for a given energy, the pulse height of α particles is larger compared to protons with all other effects such as dead-layer energy losses taken into account [120]. If this is not accounted for

in this work, when α particles are used to calibrate the Si array, observed proton energies using that calibration will differ from the true energy of the proton. To correct this, Reference [117] proposes a semi-empirical model which suggests that the energy required to produce an electron-hole pair in the detector depends on the ionisation density in the path of the charged particle and therefore the electronic stopping power of the charged particle in the detector medium, $S_{\mathrm{e}}(E)$. The model for the measured pulse-height, H, is

$$H = \varepsilon_0 \int_0^{E_0 - \Delta E_{\mathrm{n}}} \frac{\mathrm{d}E}{\varepsilon_0 - kS_{\mathrm{e}}(E)}, \tag{4.4}$$

where E_0 is the kinetic energy of the charged particle, ε_0 is the average energy needed to produce an electron-hole pair for electrons in Si, ΔE_{n} is the nuclear energy loss of the charged particle in Si and k is a constant independent of the atomic number of the charged particle. Reference [118] uses older stopping power formulations and determines the value of this constant to be $(2.8 \pm 0.3) \times 10^{-4}$ nm/electron-hole pair. Using modern stopping powers from SRIM, and varying k so that pulse-height corrections calculated using modern stopping powers were consistent with data in Reference [118], the corresponding value of k was determined to be $(2.9 \pm 0.3) \times 10^{-4}$ nm/electron-hole pair [121].

In practice, after applying energy losses (which are discussed in the next section) PHCs were used in this work to determine the expected detected energy, E_{det}, of α particles to correct the α-source calibration so that it properly corresponds to protons. To illustrate the size of the PHCs, Figure 4.9 shows the difference between E_{det} and E_0 for protons and α particles, and also the difference between the two sets of calculations, $\Delta(E_{\mathrm{det}} - E_0)$. Between energies of 1–10 MeV, $\Delta(E_{\mathrm{det}} - E_0)$ ranges from approximately -20 keV to -120 keV. The figure also shows calculations using a value of k at plus and minus one standard deviation.

4.3.3 Iterative calculations

After implementing PHCs, energy-loss corrections were applied to account for protons travelling through target material and the Al dead layer of the Si array. An iterative method was used to calculate the distance the proton travels through the target and dead layer due to the angle of its trajectory, θ_{lab}, allowing the corrected energy of the proton and therefore the excitation energy of the residual nucleus to be obtained. For the first iteration, z_{det} was used in Equation 3.36

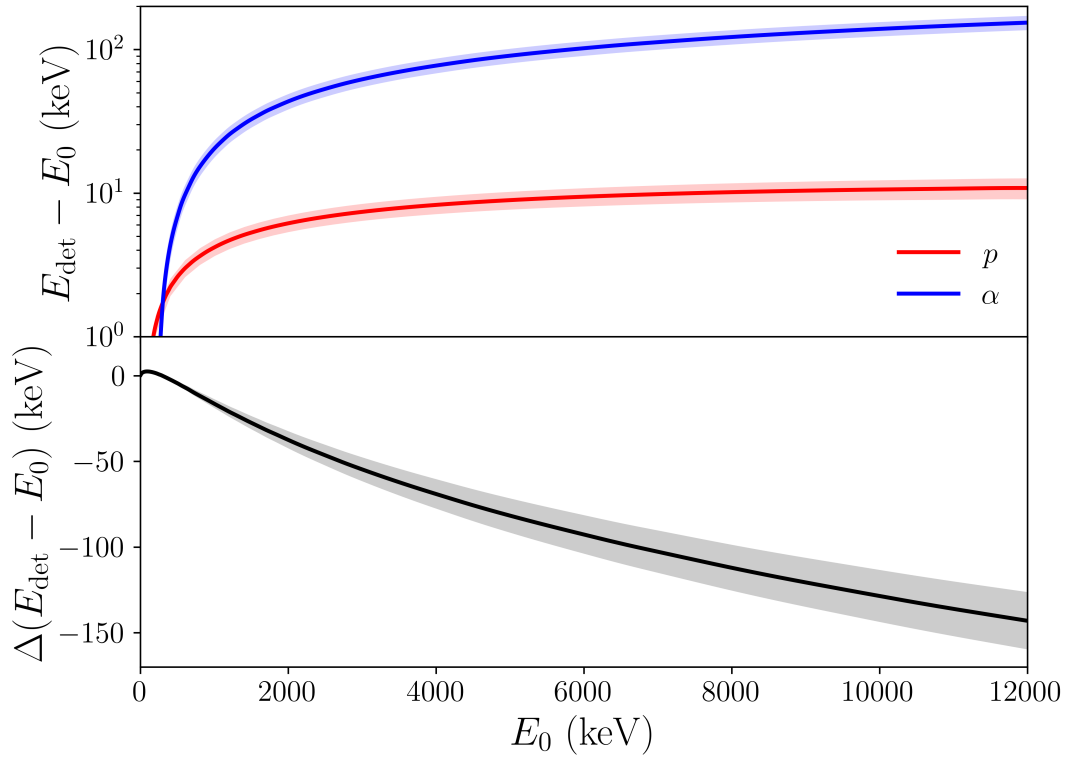


Figure 4.9: The top figure shows the difference between the detected energy true energy of protons and α-particles in a Si detector using Equation 4.4. The bottom figure shows the blue line subtracted from the red line. Bands show calculations with k at a value of plus and minus one standard deviation.

to calculate an initial guess of the angle, α, and therefore θ_{lab}. From this, the distance the proton travelled through the target, d_{t}, was calculated from

$$d_{\mathrm{t}} = \frac{t_{\mathrm{t}}}{2\sin\left(\theta_{\mathrm{lab}} - \frac{\pi}{2}\right)}, \tag{4.5}$$

where t_{t} is the nominal target thickness. This assumes that the reaction occurred at the centre of the target. Similarly, an initial guess for the distance the proton travelled through the Si array dead layer, d_{dl}, was calculated using

$$d_{\mathrm{dl}} = \frac{t_{\mathrm{dl}}}{\cos\left(\theta_{\mathrm{lab}} - \frac{\pi}{2}\right)}, \tag{4.6}$$

where $t_{\mathrm{dl}} = 0.49 \pm 0.01$ µm is the Al dead layer thickness [121]. Using these distances, the energy loss was calculated from Equation 4.3 and added back on to the energy determined from PHCs. Energy loss calculations for a proton travelling through CD_2 and Al are given in Figure 4.10 and Figure 4.11 and show that as θ_{lab} increases for a given proton energy, the proton loses more energy through the dead layer and less through the target. The corrected energy of the proton and

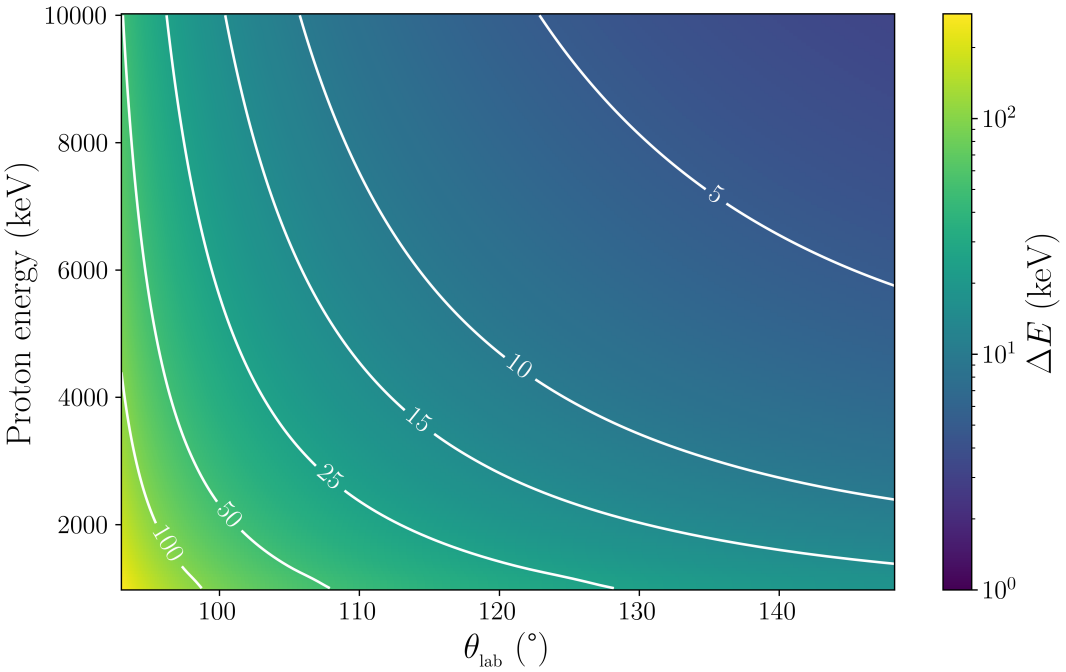


Figure 4.10: Proton energy loss in CD_2 as a function of proton energy and θ_{lab} for a target thickness of 62.5 µg/cm^2. The angle, θ_{lab}, is defined in Figure 3.14.

z_{det} could then be used in Equation 3.47. Rearranging this equation to

$$f(z) = z_{\mathrm{det}} - z\left[1 - \frac{1}{\pi}\sin^{-1}\left(\frac{\pi r_{\mathrm{det}}}{z}\tan\left(\sin^{-1}\left(\frac{qBz}{2\pi p_{\mathrm{e}}}\right)\right)\right)\right] = 0 \tag{4.7}$$

allows it to be solved using the Newton-Raphson method where z is iteratively calculated using values from the ith iteration such that

$$z_{i+1} = z_i - \frac{f(z_i)}{f'(z_i)}. \tag{4.8}$$

The derivative of the function was calculated numerically, and iterations continued until the difference between two iterations was smaller than a defined threshold. With this new distance obtained from the Newton-Raphson method, θ_{lab} and energy losses were recalculated, followed again by z using the Newton-Raphson method. This was repeated until the difference between two iterations of this whole process was less than a defined threshold. From this double-iteration method, the determined values for the energy of the proton and z from the final iteration were used in Equation 3.6 and Equation 3.9 to calculate the excitation energy of the residual nucleus as a function of z.

Data from α particles used to calibrate the Si array were also corrected for energy loss in the dead layer in a similar way. With the known kinetic energy of the α par-

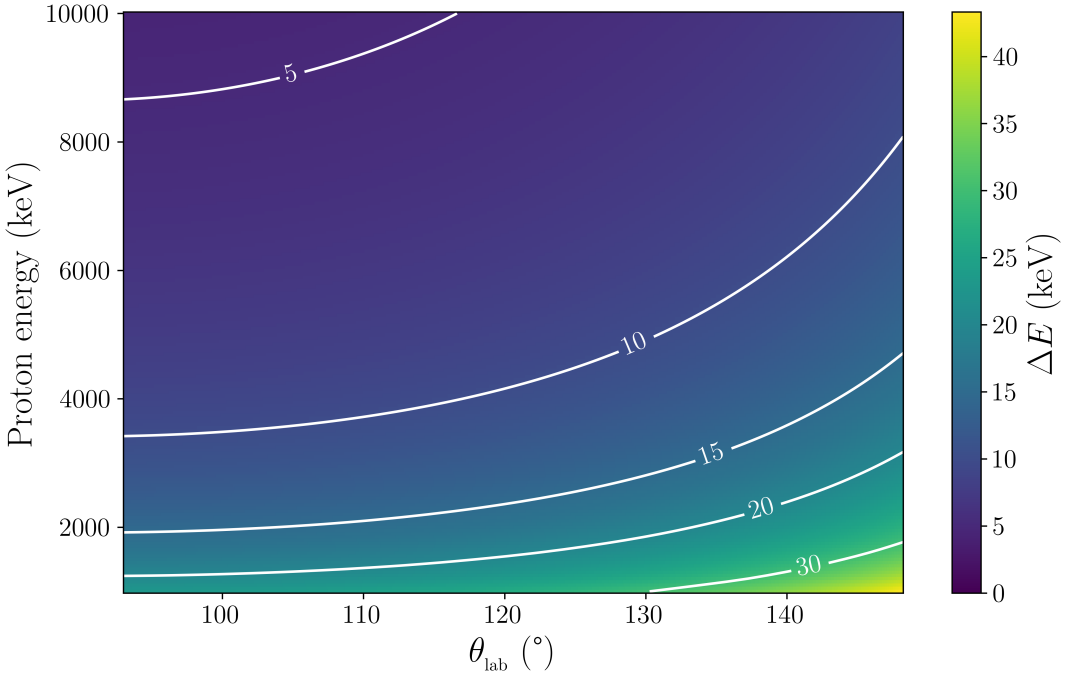


Figure 4.11: Proton energy loss in Al as a function of proton energy and θ_{lab}. A dead layer thickness of 0.49 µm has been used for these calculations.

ticle and z_{det} for each channel, the Newton-Raphson method was used to calculate z and therefore θ_{lab}. The energy loss through the dead layer was then subtracted from the known energy of the α particle in Table 4.1. After applying PHCs, this gave an expected detected energy which could be used in the calibration.

4.3.4 Additional cuts

In Figure 4.7, an excess of counts compared to the rest of the histogram can be seen at distances greater than approximately −90 mm. These data can be attributed to protons that completed multiple helical orbits before hitting the Si array. Ideally, the timing resolution of the data acquisition (DAQ) system would allow these events to be distinguished from single-orbit data. However, the timing resolution of the detector did not allow multiple-orbits to be removed and including these data would contribute to an additional background at large z. Consequently, a cut was applied to remove all data at distances greater than −87.5 mm from the target. A θ_{cm} cut was also used to discard all data calculated to be emitted at an angle of less than 14°, removing kinematic 'knees' from kinematic lines which were discussed in Section 3.2.5. The results of these cuts for the measured proton energy and excitation energy as a function of z are shown in Figure 4.12. Projections of

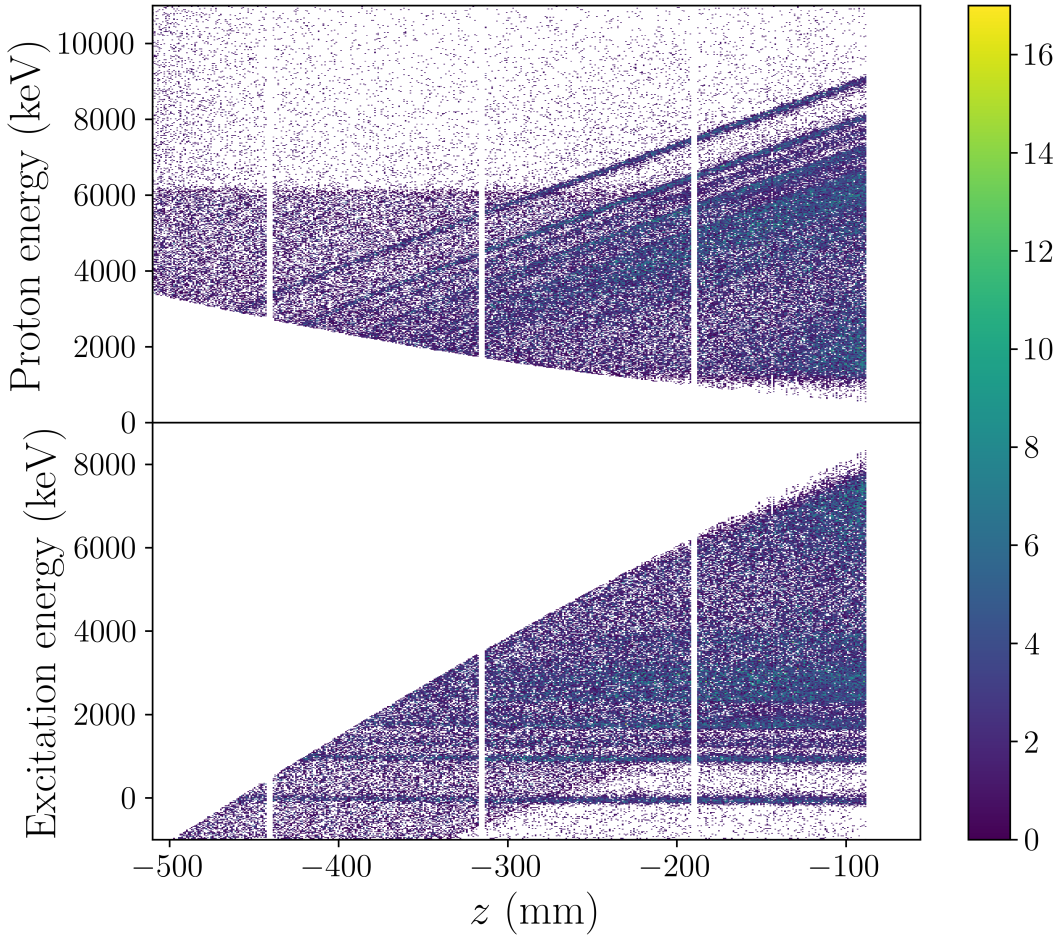


Figure 4.12: Data from the Si array that have been transformed to show the excitation energy of ^{213}Rn as a function of z with z and θ_{cm} cuts applied.

the bottom figure in Figure 4.12 showing total excitation energy spectra with and without cuts are shown in Figure 4.13. Using these cuts, the full width at half maximum (FWHM) of the ground state peak is reduced from 147.1 ± 1.7 keV to 142.9 ± 1.7 keV. These cuts also allowed a linear background function to be fitted more easily to regions either side of peaks in the spectrum, and more reliable results of energies of states and cross sections could be obtained. Solid-angle calculations, which will be discussed in Section 4.4.4, were also modified to take into account these cuts.

4.3.5 Uncertainties in centroids of excited states

Changing the value of parameters used in calculations to reconstruct excitation energies of the residual nucleus, such as target thickness, magnetic field strength and beam energy, shifts the deduced excitation energies. Using nominal parameter

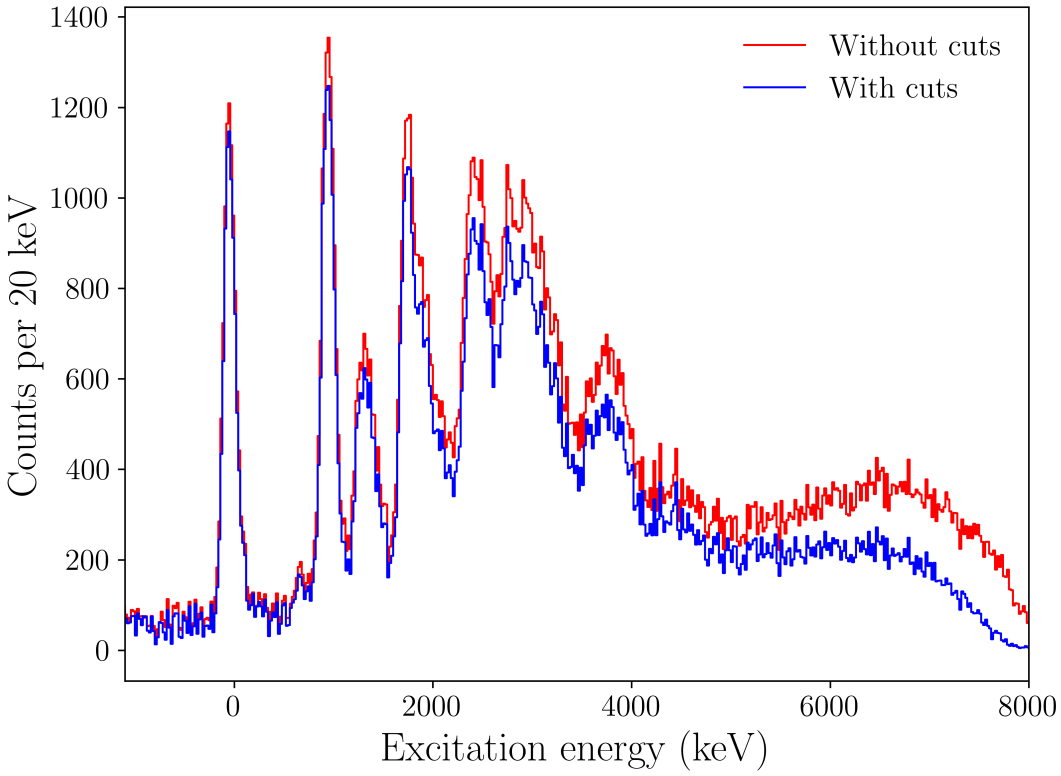


Figure 4.13: The excitation energy spectrum of ^{213}Rn with and without cuts using data from the EBIS beam-on time window with beam-off data subtracted. The neutron separation energy of ^{213}Rn is 5.108(4) MeV [122].

values, the observed centroid of the ground state is -41.4 ± 0.8 keV, where the quoted uncertainty is purely statistical. To investigate this, the data were resorted using values that differed from those given nominally. As information on the energies of excited states is limited for ^{213}Rn, only the ground state was used to compare the shift in centroids from the nominal centroid. This assumes that there are no unresolved states near the ground state, which is consistent with information of excited states for other nuclei in this isotonic chain. Results of these investigations are shown in Figure 4.14. Within $\pm 1\sigma$, independently varying the beam energy, target thickness and k used in PHCs each show a deviation from the nominal centroid of approximately 10 keV. A variation of 1% of the magnetic field strength contributes to a deviation of approximately 40 keV. Varying the distance of the Si array by ± 1 mm moves the ground state by approximately 20 keV and varying the dead layer thickness by $\pm 1\sigma$ contributes to an approximate 2-keV deviation of the nominally observed ground state centroid. Combining all of these in quadrature, assuming no correlations between parameters, gives an uncertainty on the ground state of approximately 50 keV. The observed centroid of the ground state using nominal parameter values is therefore consistent with the true energy, and energies of all excited states will be quoted with an uncertainty of 50 keV.

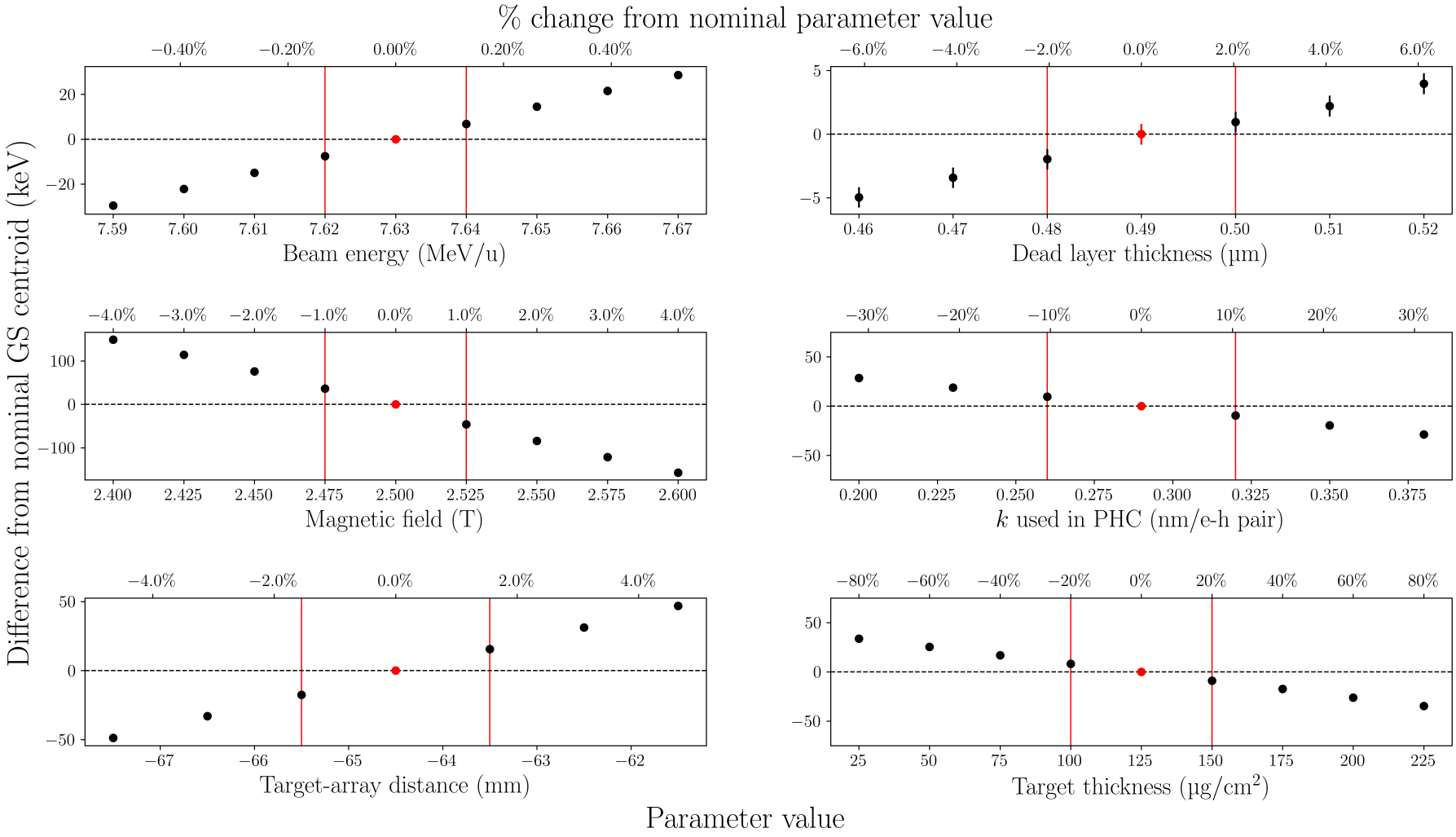


Figure 4.14: The difference of ground state centroids using different parameter values in excitation energy calculations. The red dot in each plot shows the ground state centroid using nominal parameter values and red vertical lines show approximate values at $\pm 1\sigma$ of each parameter.

Excitation energy centroids were extracted by fitting Gaussian peaks using the software package, HDTV [123]. The widths of peaks were fixed according to that of the ground state and a linear background was assumed in regions either side of peaks. The result of this fit can be seen in Figure 4.15. When extracting centroids of excited states, a systematic offset originating from errors of parameter values used to reconstruct excitation energies was assumed for all excited states. Consequently, all centroids were shifted by the 41.4 ± 0.8 keV offset of the ground state from its true value. Centroids of observed excited states are given in Table 4.6.

4.3.6 Contributions to excitation energy resolution

There are many factors that contribute to the observed resolution of excited states in the excitation energy spectrum. Using data from α particles, the intrinsic resolution of the detector is approximately 50 keV. From Section 3.3.1, a z position resolution of 1 mm contributes to a spread of approximately 15 keV in the measured proton energy. The energy loss of the beam and the ejected proton in the target material also contributes to the observed resolution. If the beam travels through all the target material, the energy loss is approximately 15.7 MeV. This introduces an energy spread of 19 keV for protons emitted from the ground state at an angle of $\theta_{\mathrm{cm}} = 15^\circ$ and 61 keV for protons emitted at an angle of $\theta_{\mathrm{cm}} = 40^\circ$. The energy loss of protons in the target material depends on the angle of emission and the energy of the proton. Considering extremes of emission angles and proton energies measured in the experiment and, as before, assuming the proton travels through all the target material, a proton emitted from the ground state of ^{213}Rn at $\theta_{\mathrm{cm}} = 15^\circ$ ($T_{\mathrm{e}} = 3.032$ MeV $\theta_{\mathrm{lab}} = 141^\circ$) loses approximately 18 keV. This increases to 38 keV if the proton is emitted at $\theta_{\mathrm{cm}} = 40^\circ$ ($T_{\mathrm{e}} = 7.724$ MeV and $\theta_{\mathrm{lab}} = 100^\circ$). For a proton emitted from a state at 3 MeV, energy losses in the target material increase to 28 keV at $\theta_{\mathrm{cm}} = 15^\circ$ ($T_{\mathrm{e}} = 6.285$ MeV and $\theta_{\mathrm{lab}} = 135^\circ$) and 95 keV at $\theta_{\mathrm{cm}} = 40^\circ$ ($T_{\mathrm{e}} = 2.002$ MeV and $\theta_{\mathrm{lab}} = 95^\circ$). The energy loss of protons in the dead layer of the Si array will also contribute to an energy shift of approximately 10–15 keV, where calculations have been performed using the same angles as above. The energy spread of the beam was 0.4% (FWHM), and this contributes to a relatively small spread in proton energy of around 5 keV. Combining these values in quadrature using extreme values, where the beam and proton travel through all the target material, gives an energy spread of $\sim$90 keV for protons emitted from the ground state at $\theta_{\mathrm{cm}} = 40^\circ$. This corresponds to an excitation energy spread of $\sim$180 keV. This reduces to a spread in excitation energy

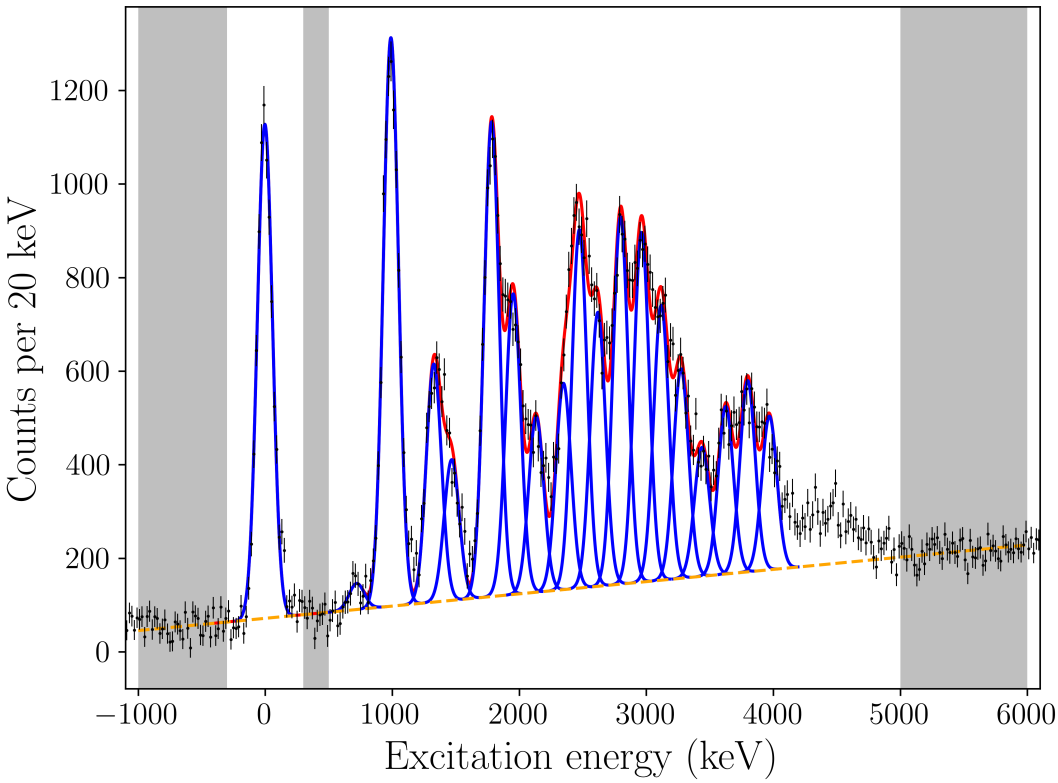


Figure 4.15: The excitation energy spectrum of ^{213}Rn using EBIS beam-on data with beam-off data subtracted. The spectrum has been fitted with Gaussian peaks and a linear background. The red line shows the combined model of the Gaussian peaks and the linear background. A decomposition of peaks is shown in blue and the linear background is represented by the dashed orange line. Grey regions indicate data selected to characterise the linear background.

of ∼150 keV for protons emitted at $\theta_{\mathrm{cm}} = 15°$. The overall observed resolution of the ground state was ∼140 keV (FWHM) and the FWHM of the ground state at different distances from the target is shown in 4.16. The dominating contribution to the resolution is energy losses in the CD_2 target material, and the observed FWHM of the ground state decreases at larger absolute distances from the target as protons are emitted at larger θ_{lab}, passing through less target material.

4.4 Cross sections

Cross sections were extracted from projections of regions of z across the Si array. In each projection, yields were extracted from peaks in Figure 4.15 using the same method as in the last section. Widths of peaks in each projection were fixed to the width of the ground state peak. Extracted yields were normalised using data

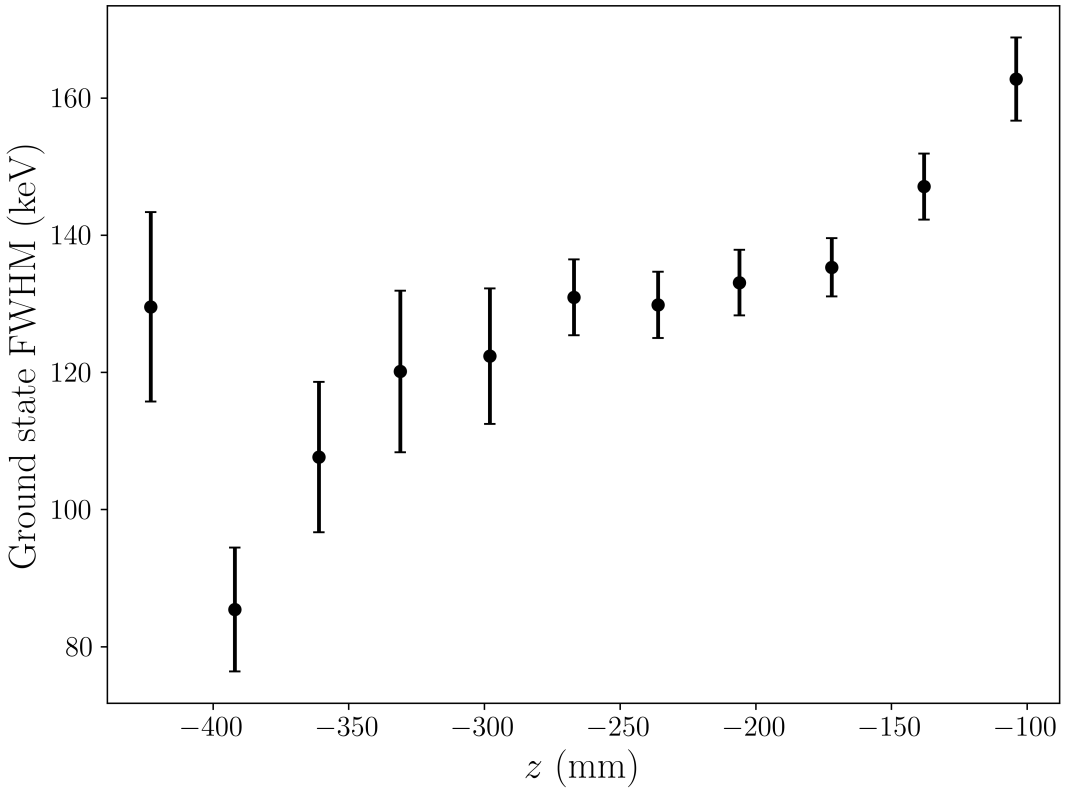


Figure 4.16: The FWHM of the ground state at different distances from the target.

from the luminosity detector and the solid angle covered by the region of z of the projection. Additionally, geometric efficiency corrections due to inactive channels of the Si array and pile-up corrections for the luminosity detector were applied.

4.4.1 Absolute normalisation using the luminosity detector

Elastically scattered deuterons measured by the luminosity detector were used to determine absolute cross sections for states populated in ^{213}Rn. Rearranging Equation 2.2 gives the product of the beam intensity and target thickness for elastic scattering as

$$N_{\mathrm{b}} N_{\mathrm{t}} = \frac{Y_d}{\frac{\mathrm{d}\sigma}{\mathrm{d}\Omega} \Delta\Omega \varepsilon}, \tag{4.9}$$

where Y_d corresponds to the number of elastically scattered deuterons measured by the luminosity detector, $\frac{\mathrm{d}\sigma}{\mathrm{d}\Omega}$ is the differential elastic scattering cross section of deuterons on ^{212}Rn, $\Delta\Omega$ is the solid angle covered by the luminosity detector and ε is the intrinsic efficiency of the detector, which was assumed to be 1. A similar

method as that described in Section 4.3.3 was used to calculate the angular range of the luminosity detector. Given that $E_{\mathrm{x}} = 0$ MeV for elastic scattering, the energy of the scattered deuteron in the centre-of-momentum (CM) frame, E'_{e} can be calculated by rearranging Equation 3.9 to

$$E'_{\mathrm{e}} = \frac{{E'_{\mathrm{tot}}}^{2} + m_{\mathrm{e}}^{2} - m_{\mathrm{r}}^{2}}{2E'_{\mathrm{tot}}} \tag{4.10}$$

With this, the momentum of the deuteron in the CM frame, p'_{e}, can be calculated from Equation 3.10. The only unknown to calculate the energy of the deuteron in the lab frame, E_{e}, from Equation 3.11, and therefore the momentum of the deuteron in the lab frame, p_{e}, is then θ_{cm}. Additionally, from Equation 3.36, z is a function of p_{e} and θ_{lab}. The angle θ_{lab} can be related to θ_{cm} through

$$\tan\theta_{\mathrm{lab}} = \frac{p'_{\mathrm{e}}\sin(\pi - \theta_{\mathrm{cm}})}{\gamma_{\mathrm{cm}}[p'_{\mathrm{e}}\cos(\pi - \theta_{\mathrm{cm}}) + \beta_{\mathrm{cm}}E'_{\mathrm{e}}]}, \tag{4.11}$$

therefore, for elastic scattering, the only unknown to calculate z is also θ_{cm} [99]. Noting that both p_{e} and z can be calculated with θ_{cm} being the only unknown, and with z_{det} known from the distance of the luminosity detector from the target, the θ_{cm} range covered by the detector was calculated by inserting the minimum and maximum detector radii into Equation 4.7 and solving for θ_{cm}. From this, the angular range covered by the detector for single-orbit elastically scattered deuterons was found to be $29.18^{\circ} \leq \theta_{\mathrm{cm}} \leq 29.56^{\circ}$. The energy of elastically scattered deuterons in this angular range is 3822–3920 keV.

Data recorded by the luminosity detector across all runs are shown in Figure 4.17. In this spectrum, peaks corresponding to single- and double-orbit deuterons can be seen. At lower energies, peaks corresponding to multiple orbits greater than two can be seen and are unresolved. Peaks at higher energies originate from deuterons elastically scattering from ^{12}C of different charge-states. A double-peak structure appears in the spectrum for data corresponding to single-orbit deuterons. The yield of both peaks was extracted by integrating the region of the peaks and performing a background subtraction by fitting a linear background either side. The potential source of this double-peak structure is explained in the next section. Different global optical models were used to calculate expected cross sections using the reaction code PTOLEMY [58]. Calculations were performed using seven different optical-model parameter sets, given in Table 4.2, and the results of calculations are shown in Figure 4.18. The integrated cross section was numerically calculated in the θ_{cm} range covered by the luminosity detector and

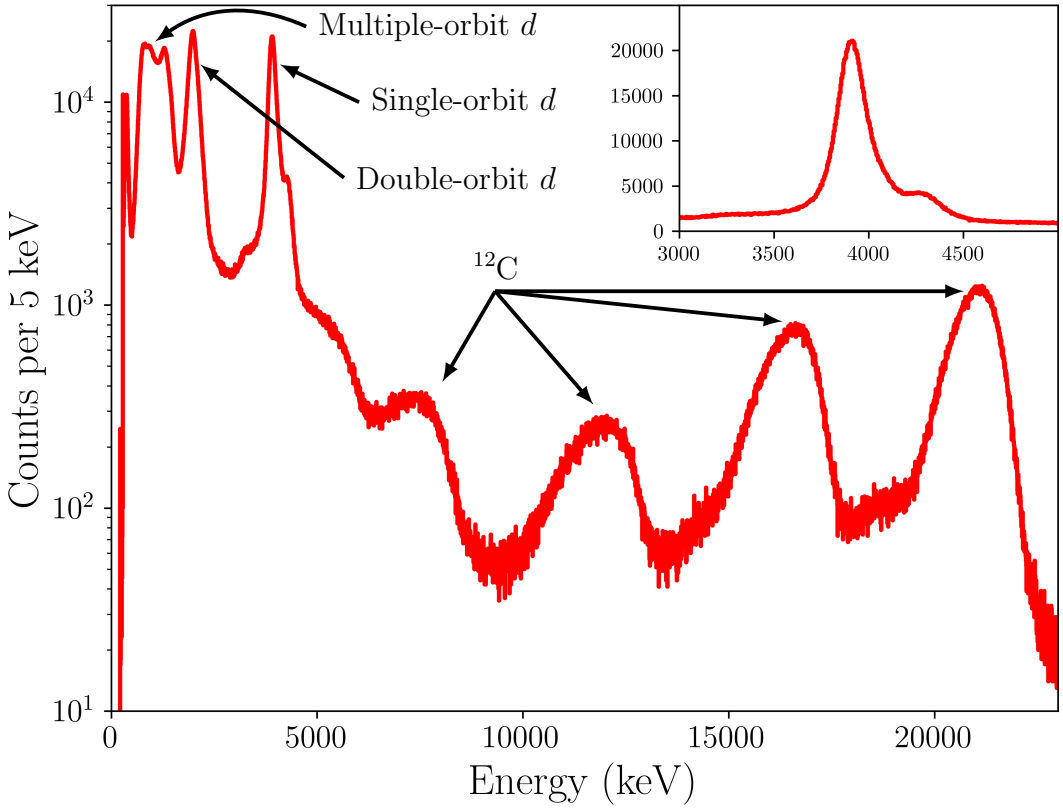


Figure 4.17: An energy spectrum using data from the luminosity detector across all runs. Data is from the EBIS beam-on time window and a background subtraction using data from the beam-off window has been applied in the same way as described in Section 4.2.2. The inset plot shows the region for single-orbit deuterons, where the double-peak structure can be seen more clearly.

used to calculate $N_\mathrm{b}N_\mathrm{t}$ from

$$N_\mathrm{b}N_\mathrm{t} = \frac{Y_\mathrm{d}}{\int \frac{\mathrm{d}\sigma}{\mathrm{d}\Omega}\,\mathrm{d}\Omega}. \tag{4.12}$$

The average integrated cross section across all models was used for these calculations giving a value of $N_\mathrm{b}N_\mathrm{t} = 4680 \pm 42 \pm 5$ mb^{-1}, where the first uncertainty is systematic from the variance of calculations using different optical models and the second uncertainty is statistical.

4.4.2 Pile-up corrections

In Figure 4.17, a double-peak structure can be seen for data corresponding to single-orbit deuterons. To investigate this behaviour, different EBIS beam-on time

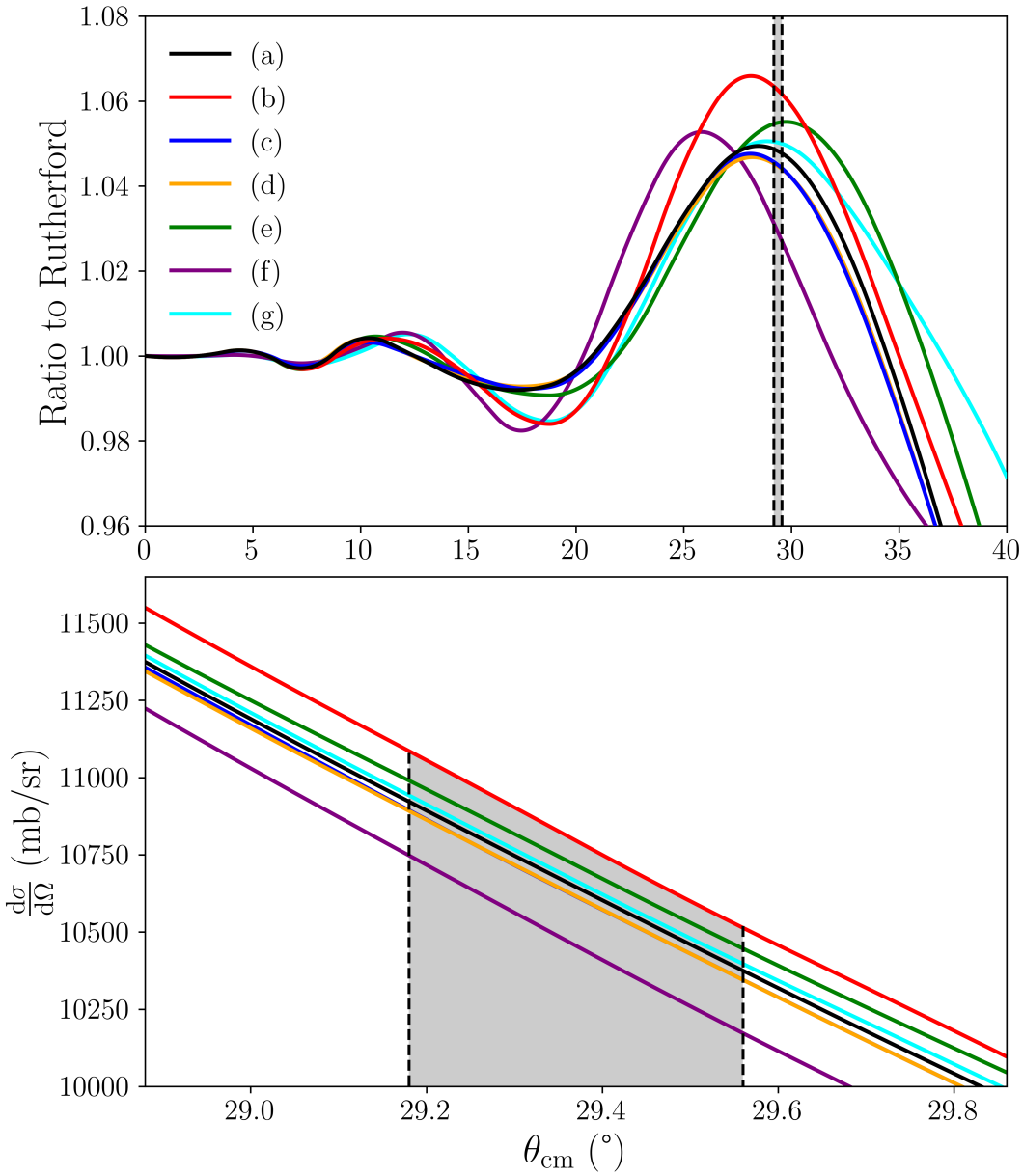


Figure 4.18: Calculations of $d(^{212}\text{Rn},d)^{212}\text{Rn}$ at 7.63 MeV. The top figure shows the ratio of the cross section to Rutherford scattering for different optical model parameter sets. The bottom figure shows calculations of cross sections using these optical model parameter sets. The grey region shows the angular range covered by the luminosity detector and the legend refers to optical model parameters sets in Table 4.2.

	Real volume			Imaginary volume			Imaginary surface			Real spin orbit			Imaginary spin orbit				
Optical Model	V_{v}	r_{v}	a_{v}	W_{v}	$\tilde{r}_{\mathrm{v}}$	$\tilde{a}_{\mathrm{v}}$	W_{s}	$\tilde{r}_{\mathrm{s}}$	$\tilde{a}_{\mathrm{s}}$	V_{so}	r_{so}	a_{so}	W_{so}	$\tilde{r}_{\mathrm{so}}$	$\tilde{a}_{\mathrm{so}}$	r_{c}	References
(a)	97.337	1.151	0.794	2.053	1.322	0.259	10.363	1.359	0.901	3.557	0.972	1.011	0	0	0	1.303	[124]
(b)	98.292	1.18	0.845	0	1.27	0.893	14.001	1.27	0.893	6	1.007	1.007	0	0	0	1.3	[125]
(c)	97.225	1.17	0.735	0.290	1.325	0.907	12.307	1.325	0.907	6.887	1.07	0.66	0	0	0	1.3	[126]
(d)	96.374	1.17	0.735	0.287	1.337	0.897	12.186	1.337	0.897	6.712	1.07	0.66	0	0	0	1.3	[126]
(e)	88.407	1.174	0.809	2.545	1.563	0.968	11.568	1.328	0.733	3.703	1.234	0.813	−0.206	1.234	0.813	1.698	[127]
(f)	122.86	1.05	0.86	0	0	0	6.131	1.43	0.962	7	0.75	0.5	0	0	0	1.3	[128]
(g)	106.489	1.15	0.81	0	0	0	18.062	1.34	0.68	0	0	0	0	0	0	1.15	[96]

Table 4.2: Optical model parameters used to calculate cross sections for the $d(^{212}\mathrm{Rn},d)^{212}\mathrm{Rn}$ reaction at 7.63 MeV/u.

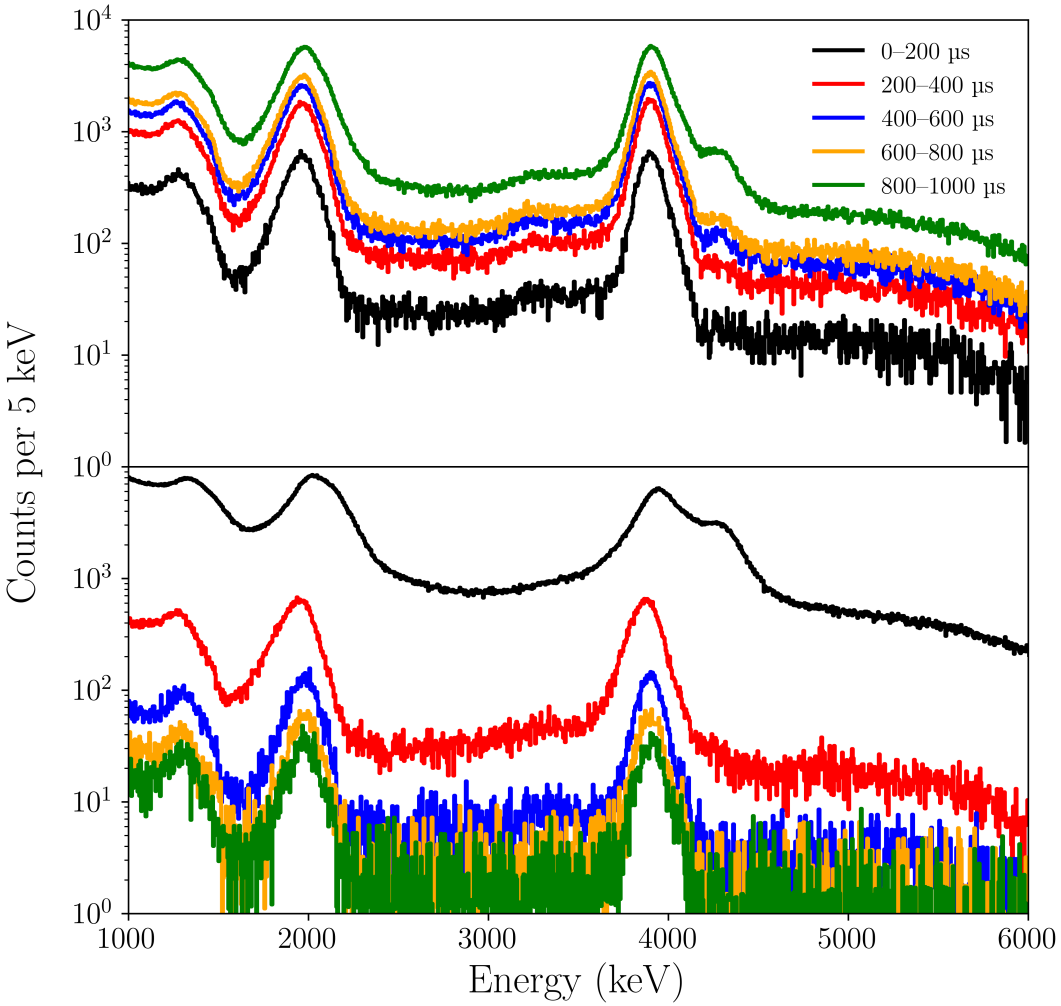


Figure 4.19: Energy spectra in the luminosity detector gated on different EBIS beam-on time windows. A background subtraction has also been applied using beam-off data. The top figure shows data from slow extraction, the bottom figure is from fast extraction.

windows were selected for fast and slow extraction data to sample the behaviour of the luminosity detector at different instantaneous beam rates. Figure 4.19 shows these spectra. For slow extraction, it can be seen that the double-peak structure is most prominent towards the end of the EBIS release profile using EBIS beam-on window of 800–1000 µs when the instantaneous rate is highest, referring back to Figure 4.6. Similarly, for fast extraction the double-peak structure in Figure 4.19 is more prominent at the beginning of the EBIS release profile where instantaneous rates are highest. Assuming that each beam pulse released from the EBIS contains the same number of ions, the instantaneous rate in the luminosity detector across the release profile can be calculated from the known total number of EBIS pulses that occurred across all runs for each extraction mode. These rates are shown Figure 4.20. For fast extraction, the highest observed instantaneous rate is approximately 100 kHz. For slow extraction it is approximately 50 kHz. The

probability of two random events occurring in the trigger hold-off time of the digitiser, P, is given by

$$P = 1 - e^{-RT}, \tag{4.13}$$

where R is the instantaneous rate and T is the trigger hold-off time [102]. For an observed instantaneous rate in the luminosity detector of 100 kHz and a trigger hold-off time of 3.176 µs, given in Section 3.3.4, $P = 0.27$. For $R = 50$ kHz, $P = 0.15$, indicating that there was likely pile-up in the luminosity detector during periods of high instantaneous beam rates. Consequently, observed cross sections calculated using the method described in the previous section will be affected by pile-up.

To correct this, the integrated cross section for the ground state across the whole Si array, $\sigma_{\Delta\Omega}$, was calculated using data only from the slow extraction mode within an EBIS beam-on time window covering 0–900 µs, where the luminosity detector was least affected by pile-up. This can be calculated from

$$\sigma_{\Delta\Omega} = \frac{Y_{\Delta\Omega}}{N_{\mathrm{b}} N_{\mathrm{t}} \Delta\Omega \varepsilon}, \tag{4.14}$$

where $Y_{\Delta\Omega}$ is the total yield of the ground state from data across the Si array and $N_{\mathrm{b}}N_{\mathrm{t}}$ is the product of the target thickness and beam intensity calculated by the method described in the previous section. The ratio, K, of $\sigma_{\Delta\Omega}$ to the observed integrated cross section of the ground state affected by pile-up from all data in slow extraction and fast extraction, $\sigma'_{\Delta\Omega}$, can be calculated from

$$K = \frac{Y_{\Delta\Omega}(N_{\mathrm{b}}N_{\mathrm{t}})'}{Y'_{\Delta\Omega}(N_{\mathrm{b}}N_{\mathrm{t}})}. \tag{4.15}$$

Prime symbols indicate quantities which have been extracted using data affected by pile-up. This factor can then be used to correct observed cross sections of excited states which have been incorrectly normalised using data from the luminosity detector affected by pile-up. A beam-on time window unaffected by pile-up but still giving large enough statistics to reduce uncertainties was chosen from slow extraction data in the range 0–900 µs. The maximum instantaneous rate in this beam-on window is approximately 5 kHz for which $P = 0.02$. The correction factor applied to cross sections from the ratio of $\sigma_{\Delta\Omega}$ using all data to $\sigma'_{\Delta\Omega}$ using data from slow extraction in the beam-on range of 0–900 µs was found to be $K = 0.73 \pm 0.02$. The uncertainty is statistical and has contributions from the fit to the ground state and from the integration of the single-orbit deuteron peak in the luminosity detector spectrum.

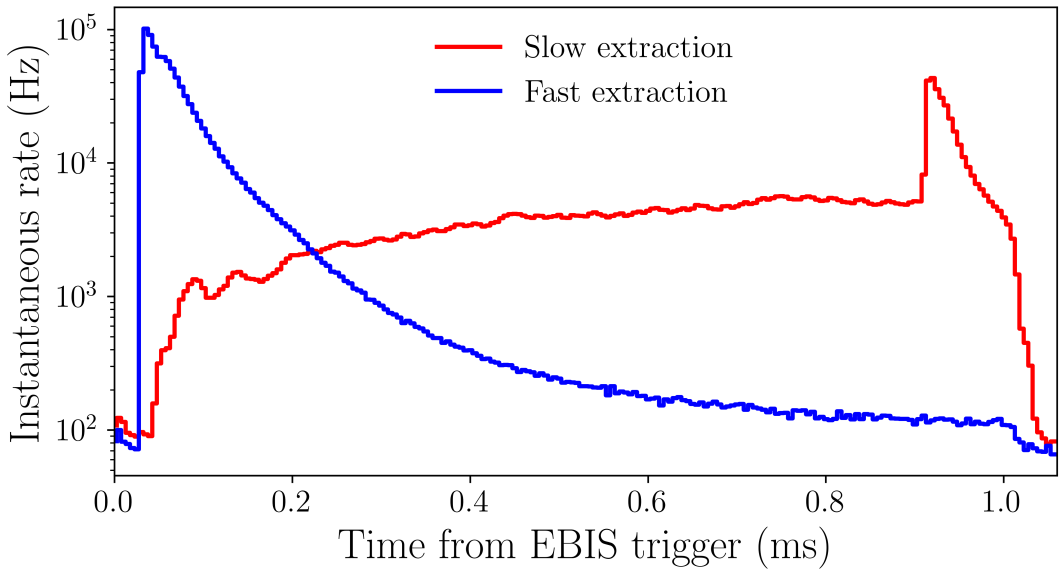


Figure 4.20: The observed rate in the luminosity detector for fast and slow extraction.

4.4.3 Geometric efficiency corrections

Further corrections needed to be applied to cross sections to account for channels in the Si array that were disabled during the experiment, reducing the geometric efficiency of the detector. A map showing inactive channels for each run in a module of the Si array is given in Figure 4.21. It can be seen that some channels were turned off only for a subset of runs, therefore this correction needed to be applied considering data on a run-by-run basis.

Channels that were powered down were determined for each run and efficiencies were calculated normalising by elastic scattering data. As coincident p-side and n-side signals were required to accept an event, the geometric efficiency in a region of z for the Si array (ignoring losses of coverage due to gaps between Si wafers), ε_{z}, is the product of the efficiencies of all p-side channels, ε_{p}, and n-side channels, ε_{n}, in that region. This can can be calculated from

$$\varepsilon_{\mathrm{z}} = \varepsilon_{\mathrm{p}}\varepsilon_{\mathrm{n}} = \frac{\sum_i \varepsilon_i^{\mathrm{p}}}{N_{\mathrm{p}}} \frac{\sum_i \varepsilon_i^{\mathrm{n}}}{N_{\mathrm{n}}}, \tag{4.16}$$

where i runs over all channels in the region of z, $\varepsilon_i^{\mathrm{p}}$ and $\varepsilon_i^{\mathrm{n}}$ are the efficiencies of channel i for p sides and n sides, respectively, and $N_{\mathrm{p,n}}$ are the number of p-side and n-side channels in the region of z. Here, it has been assumed that each channel in a region of z covers the same solid angle. For each module, the efficiency of a channel in a projection was calculated by first determining if it was turned

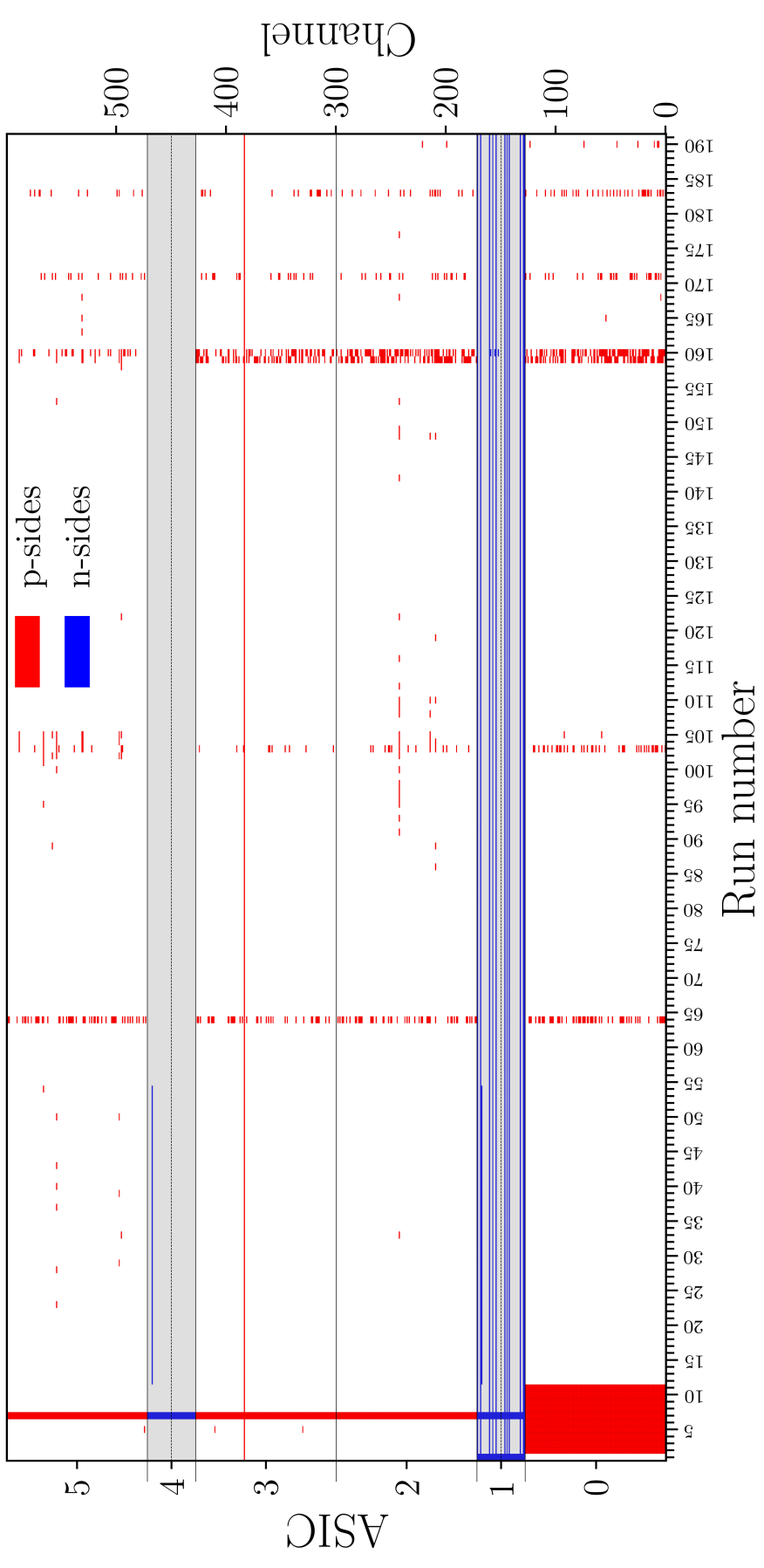


Figure 4.21: A map showing inactive channels in Module 1 for each sub-run during the experiment. Coloured regions indicate the channel was turned off for a particular run. Array modules have 600 channels covering six Si wafers. Each p-side ASIC has 128 channels aligned perpendicularly to the beam axis covering one pair of Si wafers allowing the distance from the target to be measured. Each n-side ASIC has 44 channels running parallel to the beam axis with 11 channels covering a Si wafer, as shown in Figure 3.19. A projection of excitation energy against z will therefore always cover 22 n-side channels for each module. Grey regions indicate n-side channel locations.

	Efficiency		
ASIC	Module 0	Module 1	Module 2
0	0.99	0.95	1.00
1	0.99	0.74	1.00
2	1.00	1.00	0.97
3	1.00	0.99	0.96
4	1.00	0.99	1.00
5	0.99	1.00	0.98

Table 4.3: Efficiencies of ASICs in each module due to channels being turned off. ASICs 1 and 4 correspond to n-side channels. The average across all modules was taken for each projection covering a region of z.

on through checking if any counts were recorded. Each channel in a projection was then weighted by the number of counts recorded in the single-orbit deuteron peak from the luminosity detector in that run. This was repeated for all channels across all runs of the experiment for each projection. For example, considering p-side channels, the efficiency over a region of z across j runs is

$$\varepsilon_{\mathrm{p}} = \frac{\sum_i \left(\frac{\sum_j I_{ij} N_j}{\sum_j N_j} \right)}{N_{\mathrm{p}}} = \frac{\sum_i \left(\frac{\sum_j I_{ij} N_j}{N_{\mathrm{LUM}}} \right)}{N_{\mathrm{p}}}, \tag{4.17}$$

where N_j is the integral of single-orbit deuteron data in run j and N_{LUM} is the total number of single-orbit deuteron counts in the luminosity detector across all runs. The symbol I_{ij} is a binary variable representing channel i being on or off in run j. The efficiency for n-side channels can be calculated in the same way as ε_{p} where N_{n} will always be 22 as each projection in a region of z will cover all n-side channels. The efficiencies of each ASIC are shown in Table 4.3. Efficiencies for projections of regions of z used to calculate cross sections ranged from 0.90–0.99.

Additionally, a systematic reduction in cross sections was seen for all states at points corresponding to the highest θ_{cm} angle. This was attributed to larger trajectory protons support structures at the base of the magnet which held the detectors and target frame. For the ground state, data was taken from only one module of the Si array which did not see a reduction in cross section due the orientation of trajectories hitting that section of the Si array.

4.4.4 Solid angles

With the known excitation energy of each state, the angles θ_1 and θ_2 at the limits of a projected region of z were calculated for projections of excitation energy versus z in a similar way as that described in Section 4.4.1. With these angular limits, the solid angle of each projection was calculated from

$$\Delta\Omega = \varepsilon_\theta \varepsilon_\phi \int \mathrm{d}\Omega = \varepsilon_\theta \varepsilon_\phi 2\pi \int_{\theta_1}^{\theta_2} \sin\theta \, \mathrm{d}\theta = \varepsilon_\theta \varepsilon_\phi 2\pi (\cos\theta_1 - \cos\theta_2), \tag{4.18}$$

where ε_θ and ε_ϕ are polar and azimuthal efficiencies of the Si array due to gaps in Si wafers with values of 1 and 0.7, respectively, for all projections. From Figure 3.13, it can be seen that θ_{cm} does not map linearly to z, therefore the average of the angular range of a region of z was calculated from

$$\bar{\theta}_{\mathrm{cm}} = \frac{\int \theta \mathrm{d}\Omega}{\int \mathrm{d}\Omega} = \frac{\int_{\theta_1}^{\theta_2} \theta \sin\theta \mathrm{d}\theta}{\int_{\theta_1}^{\theta_2} \theta \mathrm{d}\theta} = \frac{\sin\theta_2 - \sin\theta_1 + \theta_1 \cos\theta_1 - \theta_2 \cos\theta_2}{\cos\theta_1 - \cos\theta_2} \tag{4.19}$$

for each state in every region of z.

4.5 Angular momentum assignments and spectroscopic factors

Using experimental cross sections, angular distributions were produced for each state. By comparing experimental distributions to those calculated using the distorted-wave Born approximation (DWBA) code, PTOLEMY, the orbital angular momentum transferred to excited states can be inferred. For these calculations, different optical-model parameter sets can be used to model incoming and outgoing optical potentials. Variations of cross section calculations resulting from the use of different parameter sets is discussed in Section 4.5.1. The Argonne v_{18} potential [64] was used to describe the deuteron bound state, with parameters of $r_0 = 1.28$ fm, $a_0 = 0.65$ fm, $V_{\mathrm{so}} = 6$ MeV, $r_{\mathrm{so}} = 1.1$ fm, $a_{\mathrm{so}} = 0.65$ fm chosen for the neutron bound to ^{212}Rn. This combination of bound-state parameters was chosen to be consistent with a systematic study of cross sections from Reference [63].

Two model-dependent assumptions were made when assigning angular momentum transfers to different states. First, it was assumed that the population of states in ^{213}Rn corresponded to orbitals above the $N = 126$ shell closure. Experimental cross sections were therefore compared to calculations corresponding to orbitals $2g_{9/2}$, $2g_{7/2}$, $3d_{5/2}$, $3d_{3/2}$, $1i_{11/2}$, $4s_{1/2}$, and $1j_{15/2}$. Additionally, as the ground state of ^{212}Rn has a spin of 0^+, in some cases the total spin of an excited state can be inferred from the ℓ transferred to the state. Transfers of $\ell = 0, 6, 7$ can be attributed to the population of orbitals $4s_{1/2}$, $1i_{11/2}$ and $1j_{15/2}$, respectively. Transfers of $\ell = 2$ and $\ell = 4$ correspond to one of the spin-orbit partners in $3d$ and $2g$ shells, respectively, which cannot be distinguished.

As there is limited information on the spins of states in ^{213}Rn, assignments were guided by calculating the χ^2 for distributions of states for different ℓ transfers. Generally, the angular distribution with the smallest χ^2 was used as the assignment of ℓ transfer to a state. For distributions showing no clear best fit, a number of potential ℓ-transfer candidates are given.

4.5.1 Comparing optical models

The $d(^{212}\text{Rn},p)^{213}\text{Rn}$ reaction was modelled using different global optical-model parameter sets. Such parameters are deduced by fitting data from elastic-scattering experiments for different masses of nuclei at different projectile energies. Parameters for the ground state in ^{213}Rn for seven incoming and five outgoing optical models are given in Table 4.4. For deuteron parameter sets, Models (a), (c), (d) and (g) are derived from data in the appropriate mass and energy range consistent with this experiment. For proton models, only model (A) has parameters derived from data in the appropriate mass and energy range.

Figure 4.22 shows cross section calculations fit to experimental data for the ground state in ^{213}Rn using different optical-model combinations. These informed the choice of the optical models to be used for the rest of the analysis process by identifying which model combination reproduced ground state data best. Ideally, this process would be done using known states of different ℓ-transfers. However, as information on the spins of states is limited in ^{213}Rn this was not possible, and so only the ground state was used. For this, data were compared to calculations for an $\ell = 4$ transfer to the $2g_{9/2}$ orbital — consistent with other nuclei in this isotonic chain [40, 48]. The combination of optical models with the best fit of the ground

Optical Model	Real volume			Imaginary volume			Imaginary surface			Real spin orbit			Imaginary spin orbit				
	V_v	r_v	a_v	W_v	$\tilde{r}_v$	$\tilde{a}_v$	W_s	$\tilde{r}_s$	$\tilde{a}_s$	V_{so}	r_{so}	a_{so}	W_{so}	$\tilde{r}_{so}$	$\tilde{a}_{so}$	r_c	References
(a)	97.337	1.151	0.794	2.053	1.322	0.259	10.363	1.359	0.901	3.557	0.972	1.011	0	0	0	1.303	[124]
(b)	98.292	1.18	0.845	0	1.27	0.893	14.001	1.27	0.893	6	1.007	1.007	0	0	0	1.3	[125]
(c)	97.225	1.17	0.735	0.290	1.325	0.907	12.307	1.325	0.907	6.887	1.07	0.66	0	0	0	1.3	[126]
(d)	96.374	1.17	0.735	0.287	1.337	0.897	12.186	1.337	0.897	6.712	1.07	0.66	0	0	0	1.3	[126]
(e)	88.407	1.174	0.809	2.545	1.563	0.968	11.568	1.328	0.733	3.703	1.234	0.813	−0.206	1.234	0.813	1.698	[127]
(f)	122.86	1.05	0.86	0	0	0	6.131	1.43	0.962	7	0.75	0.5	0	0	0	1.3	[128]
(g)	106.489	1.15	0.81	0	0	0	18.062	1.34	0.68	0	0	0	0	0	0	1.15	[96]
(A)	59.414	1.17	0.75	0.657	1.32	0.642	10.249	1.32	0.642	6.2	1.01	0.75	0	0	0	1.3	[129]
(B)	57.571	1.236	0.646	0.836	1.236	0.646	10.014	1.248	0.629	6.036	1.077	0.590	−0.051	1.077	0.59	1.219	[62]
(C)	57.293	1.16	0.75	2.573	1.37	0.807	6.362	1.37	0.807	6.04	1.064	0.78	0	0	0	1.25	[130]
(D)	55.771	1.25	0.65	0	0	0	13.5	1.25	0.47	7.5	1.25	0.47	0	0	0	1.25	[97]
(E)	56.729	1.212	0.69	0.608	1.26	0.69	10.04	1.26	0.69	5.9	1.139	0.63	0	0	0	1.26	[131]

Table 4.4: Optical model parameters used to calculate cross sections for the ground state in the $d(^{212}\mathrm{Rn},p)^{213}\mathrm{Rn}$ reaction at 7.63 MeV/u. Symbols are defined in Section 2.2.1

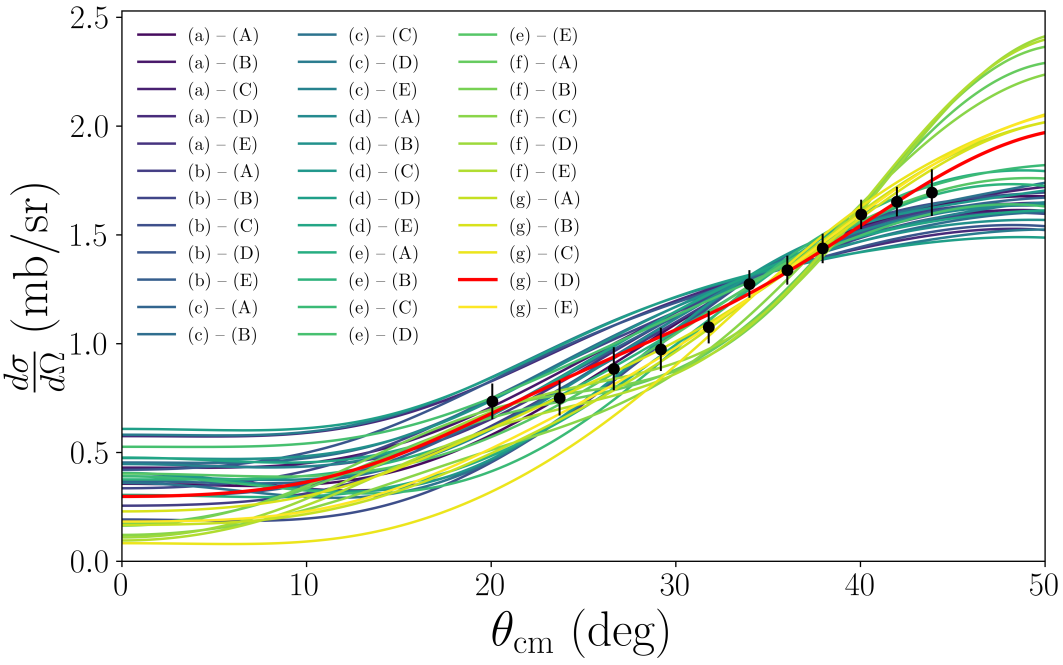


Figure 4.22: Angular distributions using different combinations of optical-model parameter sets. Data from the ground state of ^{213}Rn has been fit to PTOLEMY calculations of an $\ell = 4$ transfer to the $2g_{9/2}$ orbital. The red line shows the combination of models with the best fit to data.

state and selected to analyse unknown states in ^{213}Rn were from Reference [96] and Reference [97] for deuteron and proton parameters, respectively.

Cross section data for states with known spin assignments in ^{209}Pb from Reference [40] populated using the ^{208}Pb(d,p)^{209}Pb reaction were also compared to DWBA calculations using optical-model parameters from References [96, 97]. Data were extracted using the software package, WebPlotDigitizer [132]. This study was chosen as the reaction was performed at a similar energy of 7.4 MeV/u. Additionally, data in similar angular ranges as those measured for states in ^{213}Rn was selected. Fits of experimental data to DWBA calculations are shown in Figure 4.23, and it can be seen that angular distributions adequately follow calculations for all ℓ transfers, further justifying the choice of these optical-model parameter sets.

4.5.2 Dependency of absolute spectroscopic factors on optical-model parameters

Calculations for DWBA reactions require optical-model input parameters and are therefore model dependent. Absolute spectroscopic factors are usually very model

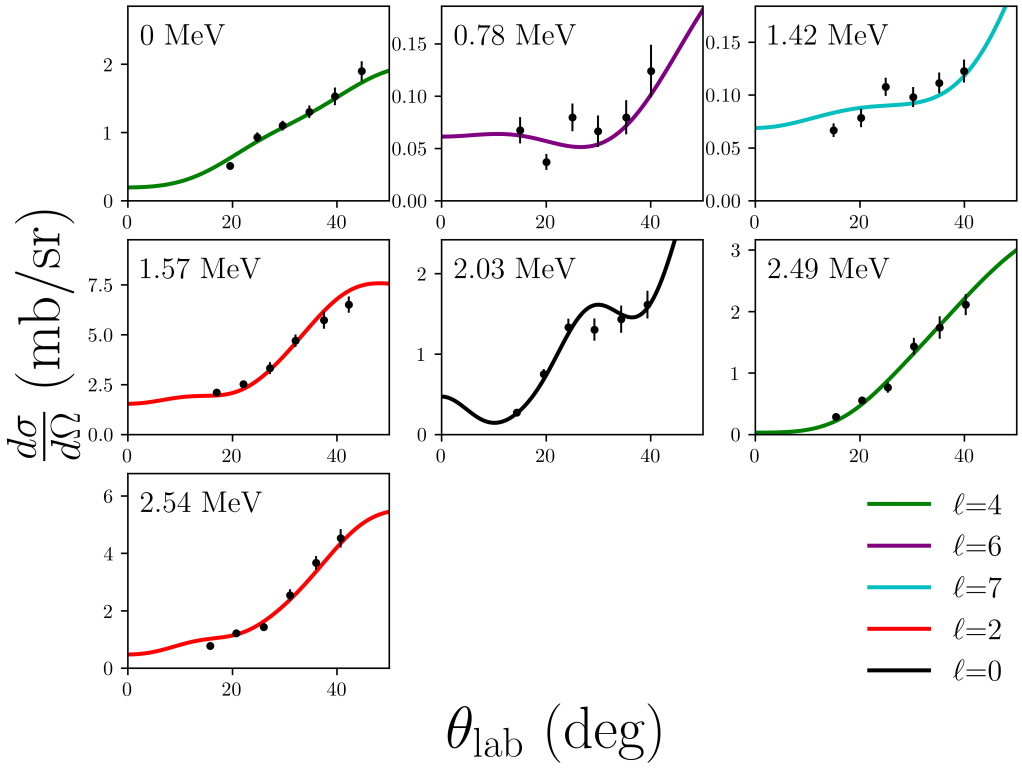


Figure 4.23: Experimentally measured angular distributions of states observed in ^{209}Pb fitted to DWBA calculations using optical-model parameters from References [96, 97]. Experimental data taken from Reference [40]. Each angular distribution has been labelled with the energy of the state in ^{209}Pb.

dependent, but relative spectroscopic factors tend to vary less. To investigate this effect, DWBA calculations have been performed with various combinations of optical-model parameter sets. Absolute spectroscopic factors from all model combinations calculated for strong states where an ℓ transfer has been firmly assigned using the model combination of Reference [96] and Reference [97] are shown in Figure 4.24. The average and standard deviation of absolute spectroscopic factors weighted by statistical uncertainties from fits of DWBA calculations to cross sections for these states are also given in Table 4.5. The absolute spectroscopic factor of the ground state is shown to vary considerably with a weighted standard deviation of ±23% as a ratio of the weighted average. Across strong states that could be assigned an ℓ-transfer, the ratio of the weighted standard deviation to the weighted average is approximately ±17%.

Relative spectroscopic factors were also obtained with respect to the ground state for each optical-model combination. These are shown in Figure 4.25. For the state at 0.99 MeV, the variation of relative spectroscopic factors was considerably less, with a weighted standard deviation of ±8% the ratio of the weighted average

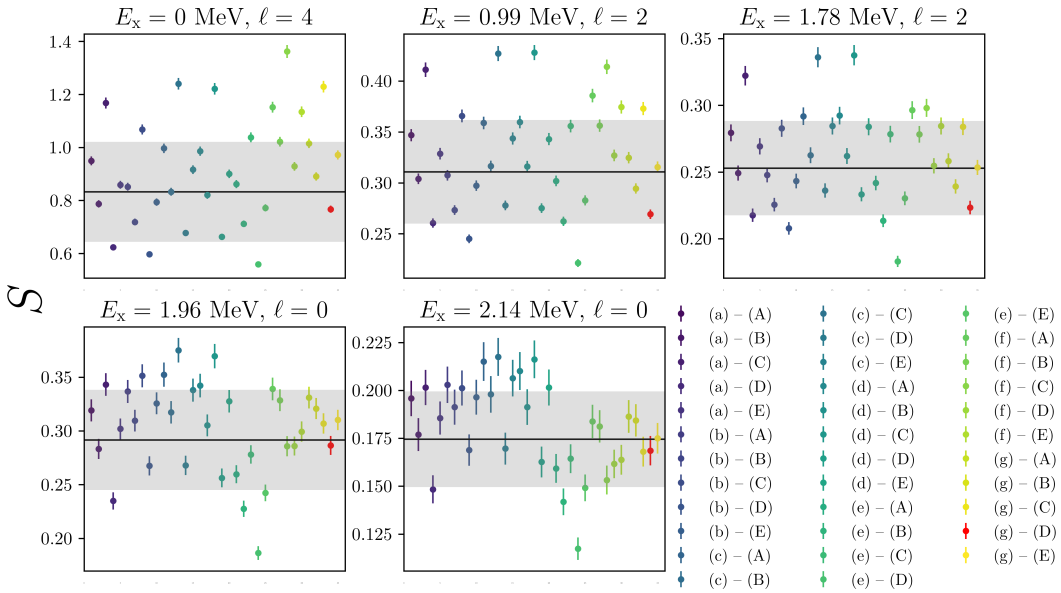


Figure 4.24: Absolute spectroscopic factors for states in ^{213}Rn using different optical-model parameter sets. Red data points are using optical-model parameters that produced the best fit in Figure 4.22. Black horizontal lines and grey regions show weighted averages and weighted standard deviations, respectively.

compared to ±16% using absolute spectroscopic factors. The weighted average and weighted standard deviation of relative spectroscopic factors are given in Table 4.5 and, across all states, show a slightly smaller variation of ±14% compared to the variation of absolute spectroscopic factors.

4.5.3 States in ^{213}Rn

Information about states observed in ^{213}Rn is summarised in Table 4.6. This contains assignments of the ℓ transferred to each state, cross sections measured at

		S		S_{rel}	
E_x (MeV)	ℓ	Weighted average	Weighted SD (%)	Weighted average	Weighted SD (%)
0	4	0.83	23	—	—
0.99	2	0.31	16	0.36	8
1.79	2	0.25	14	0.28	12
1.96	0	0.29	16	0.32	17
2.14	0	0.17	14	0.19	21

Table 4.5: The variation of absolute and relative spectroscopic factors for states in ^{213}Rn that could be assigned an ℓ-transfer.

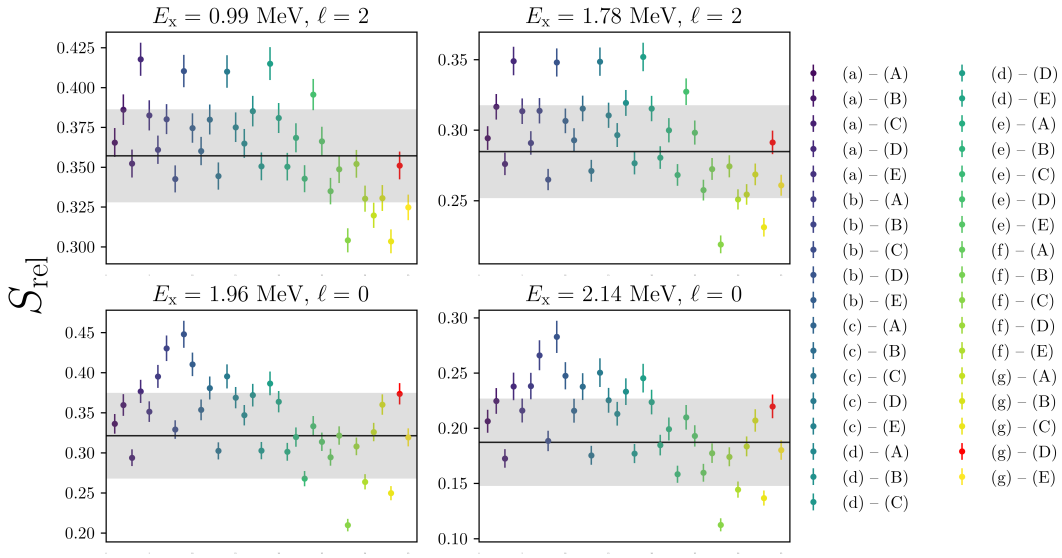


Figure 4.25: Relative spectroscopic factors for states in ^{213}Rn using different optical-model parameter sets. Each optical-model combination has been normalised to the absolute spectroscopic factor calculated for the ground state. The red data point is using optical-model parameters that produced the best fit in Figure 4.22. Black horizontal lines and grey regions show weighted averages and weighted standard deviations, respectively.

the largest θ_{cm} and absolute spectroscopic factors. Raw spectroscopic factors are the ratio of the experimental to DWBA cross sections. For states with multiple possible assignments, this information is given for each ℓ transfer. Figure 4.26 shows angular distributions calculated using PTOLEMY normalised to experimental data for each state. Several possible distributions are shown when an ℓ assignment was not possible. States will be discussed alongside firm and tentative spin assignments from previous studies on states in ^{213}Rn.

The strongest resolved states observed in ^{213}Rn correspond to the ground state, State 3 and State 6. As discussed in Section 4.5.1, the ground state is firmly assigned as an $l = 4$ state based on the shape of its angular distribution — agreeing with other nuclei in the isotonic chain. State 3 and State 6 are both assigned as $\ell = 2$ states based on the shapes of their angular distributions (see Figure 4.26).

State 2 is tentatively assigned as an $\ell = 6$ state based on its angular distribution. The energy and spin of this state is consistent with an assignment of a 705 keV state from heavy-ion fusion evaporation reactions in Reference [50]. In this study, conversion coefficients were inferred from intensity balances in γ-ray coincidence measurements and compared to theoretical calculations. A state was also observed

State	E_x (MeV)	$\frac{d\sigma}{d\Omega}$ (mb/sr)	θ_{cm} (°)	ℓ	S
1	0	1.65(7)	41.98	4	0.77(1)
2	0.72(5)	0.11(1)	41.99	(6)	0.64(6)
3	0.99(5)	1.96(8)	40.15	2	0.27(1)
4	1.33(5)	0.63(5)	39.46	(2, 0)	0.092(4), 0.20(1)
5	1.47(5)	0.51(5)	39.17	(2, 0)	0.062(3), 0.13(1)
6	1.78(5)	1.77(9)	38.51	2	0.22(1)
7	1.96(5)	1.12(7)	38.11	0	0.29(1)
8	2.14(5)	0.51(5)	37.70	0	0.17(1)
9	2.36(5)	0.81(18)	37.18	(4, 2, 0)	0.38(2), 0.13(1), 0.21(1)
10	2.48(5)	1.16(17)	36.89	(4, 2, 0)	0.51(2), 0.18(1), 0.32(1)
11	2.63(5)	1.17(14)	36.52	(2)	0.14(1)
12	2.80(5)	1.50(9)	36.09	(4, 2)	0.50(1), 0.17(1)
13	2.97(5)	1.39(10)	35.65	(2)	0.18(1)
14	3.12(5)	1.12(9)	35.25	(2)	0.15(1)
15	3.28(5)	0.75(9)	34.81	(2, 0)	0.12(1), 0.25(1)
16	3.44(5)	0.44(8)	34.36	(2)	0.08(1)
17	3.63(5)	0.66(7)	33.80	(2)	0.11(1)
18	3.80(5)	0.85(8)	33.29	(2)	0.13(1)
19	3.97(5)	0.59(7)	32.76	(4, 2)	0.22(1), 0.08(1)

Table 4.6: States in ^{213}Rn populated in the $d(^{212}\mathrm{Rn},p)^{213}\mathrm{Rn}$ reactions at 7.63 MeV/u. Cross sections at the largest value of θ_{cm}, angular momentum transfers and spectroscopic factors for each state have been listed. Spectroscopic factors for all ambiguous assignments have also been shown. Uncertainties given for cross sections and spectroscopic factors are purely statistical.

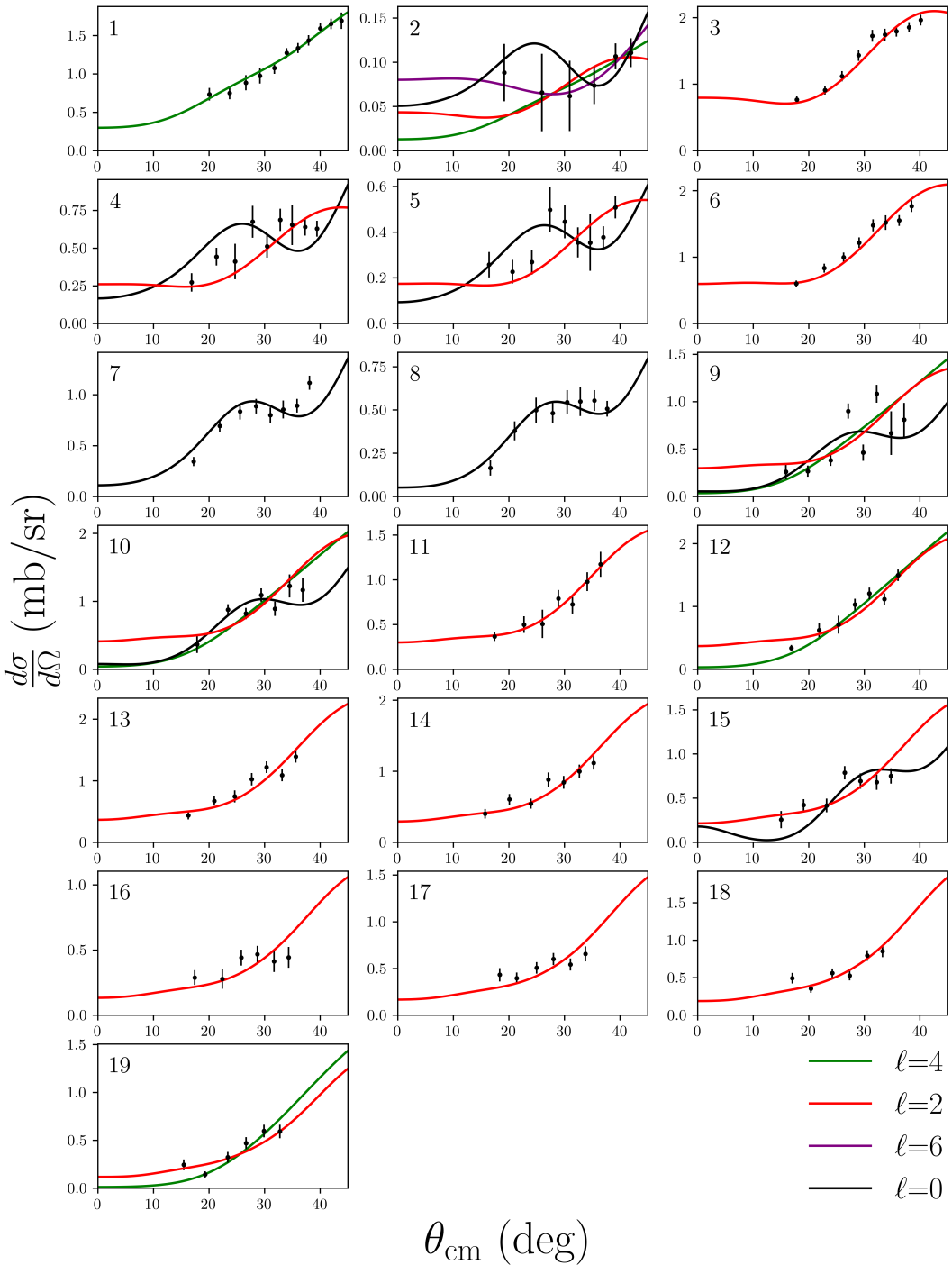


Figure 4.26: Angular distributions of states observed in ^{213}Rn. Error bars include only statistical uncertainties from fits to spectra. Multiple cross section calculations are shown for states that could not be assigned an ℓ transfer.

at 705 keV and tentatively assigned as $\ell = 6$ in Reference [51]. Conversion coefficients were also measured here following the EC/β^+ decay of ^{213}Fr. All possible angular distributions have been shown for this state in Figure 4.26. States 7 and 8 are assigned as $\ell = 0$. States 11, 13, 14, 16, 17 and 18 have been tentatively assigned as $\ell = 2$. Distributions of $\ell = 2$ and $\ell = 4$ are similar for these states, however, the data point at the lowest θ_{cm} point follows $\ell = 2$ distributions more closely than $\ell = 4$. They have been tentatively assigned as states are unresolved in excitation energy spectra.

The distributions for states 4, 5 and 15 appear to rule out $\ell = 4$ but are assigned as either $\ell = 2$ or $\ell = 0$ and could not be distinguished due to large uncertainties. State 4 appears to be consistent with States 12 and 19 have been assigned as either $\ell = 4$ or $l = 2$. Angular distributions indicate that the ℓ-transfer to states 9 and 10 are either $\ell = 4$, $\ell = 2$ or $\ell = 0$.

States observed in this work have also been compared with states observed via the EC/β+ of ^{213}Fr [51] in Table 4.7. As mentioned above, the ground state angular momentum assignment in this work is consistent with data in Reference [51], as is the excitation energy and tentatively assigned angular momentum of the first-excited state. State 4 at 1.33 MeV is comparable to the two states at approximately 1.35 MeV in Reference [51], however as they are separated by 6 keV they are not able to be resolved in this work. Additionally, the state at 1.79 MeV in Reference [51] is consistent with State 6 at 1.78 MeV. The state at 1.83 MeV in Reference [51] appears to have no obvious comparison to any state observed in this work. The authors in Reference [51] assume that states observed in ^{213}Rn from the EC/β+ decay of the $9/2^-$ ground state in ^{213}Fr are populated by first-forbidden transitions, and therefore give tentative spin assignments of either $7/2^+$, $9/2^+$ or $11/2^+$ to all states above the first-excited state, disagreeing with the assignments of corresponding states in this work.

The difficulty in assigning angular momentum to states in this work comes from the flattening of angular distributions as the excitation energy of the residual nucleus increases. This has the effect of making angular distributions less distinguishable from one another. Increasing the beam energy to increase the difference of shapes of distributions, as shown in Figure 3.7, or having access to cross sections at larger θ_{cm} where angular distributions of $\ell = 0$ diverge more from $\ell = 2$ and $\ell = 4$ is likely to have improved the situation. However, 7.63 MeV/u was the highest practicable beam energy and the length of the Si array limits the angular dependence. Additionally, above State 8, the density of peaks becomes large and

This Work			^{213}Fr EC/β^+ [51]		
E_x (MeV)	ℓ	J^π	E_x (MeV)	ℓ	J^π
0.0	4	$9/2^+$	0	(4)	$(9/2^+)$
0.72	(6)	$(11/2^+)$	0.7043	(6)	$(11/2^+)$
1.33	(2, 0)	$(5/2^+, 3/2^+, 1/2^+)$	1.3470	(4, 6)	$(7/2^+, 9/2^+, 11/2^+)$
			1.3527	(4, 6)	$(7/2^+, 9/2^+, 11/2^+)$
1.78	2	$5/2^+, 3/2^+$	1.7850	(4, 6)	$(7/2^+, 9/2^+, 11/2^+)$
—	—	—	1.8341	(4, 6)	$(7/2^+, 9/2^+, 11/2^+)$

Table 4.7: Excitation energies and angular momentum assignments of states extracted in this work compared to states observed in the EC/β^+ decay of ^{213}Fr [51]. Uncertainties in excitation energies from Reference [51] are 0.5 keV. The two states at approximately 1.35 MeV in Reference [51] have been compared to the state at 1.33 MeV as they would not be resolved using data in this work.

peaks are less well resolved, making the fitting procedure more challenging. The ^{210}Po(d,p)^{211}Po reaction performed 8.5 MeV/u [48] had a much greater resolving power compared to this experiment due to being performed in normal kinematics and experiencing less pronounced kinematic effects. In the region of excitation energy between 2–4 MeV, 27 states were observed in ^{211}Po compared to 12 in this study. It would be expected that states become more fragmented as protons are added to the $\pi 1h_{9/2}$ orbital on top of the $Z = 82$ closed shell, suggesting there are states in ^{213}Rn in this excitation energy range which could not be resolved. Theoretical calculations will be compared and discussed in the next chapter.

Blank page

Chapter 5

Discussion

This chapter will discuss results obtained from the $d(^{212}\mathrm{Rn},p)^{213}\mathrm{Rn}$ experiment with a particular focus on $\nu 2g_{9/2}$ and $\nu 1i_{11/2}$ orbitals. Uncertainties of spectroscopic factors will be discussed, and binding energies of single-particle centroids will be compared to two-body matrix elements and shell-model calculations.

5.1 Uncertainties in spectroscopic factors

Before discussing the interpretation of data in detail, it is important to put spectroscopic factors and their uncertainties into context. These uncertainties come from both experimental cross sections and from model dependencies in DWBA calculations that are needed to extract the spectroscopic factor. Whilst this model dependence means that spectroscopic factors are not strictly observable quantities, the model dependence is relatively well understood and their value in the historical development of an understanding of single-particle structure is clear. Several more recent analyses have illustrated the value of spectroscopic factors in understanding single-particle trends and nucleon occupancies [63, 133, 134].

Considering contributions of uncertainties to cross sections, there is an error associated with the solid angle coverage, $\Delta\Omega$. The uncertainty in the position of the Si array is at most ± 1 mm. This translates into an uncertainty in the associated solid angle of approximately 5%. A contribution to uncertainties in measured cross sections also comes from the normalisation factor $I_0 N_\mathrm{t}$. Again assuming ± 1 mm

uncertainty in the position of the luminosity detector contributes to a relatively small uncertainty in $N_\mathrm{b}N_\mathrm{t}$ of around 0.5%. The largest contributing uncertainty to $N_\mathrm{b}N_\mathrm{t}$ is the variation in elastic-scattering calculations from different optical models. This is discussed in Section 4.4.1, and a systematic uncertainty of around 1% was found. The largest overall contributing uncertainty to measured cross sections is the uncertainty in the yield of peaks when fitting excitation energy spectra. Depending on the state and the particular projection, uncertainties of yields from the fitting procedure tended to be around 5–20%, and larger when fitting weaker, less-resolved states such as the tentatively assigned $\ell = 6$ state at 720 keV. Uncertainties of cross sections contribute to uncertainties in spectroscopic factors through fits to DWBA calculations and statistical uncertainties of spectroscopic factors from these fits are shown in Table 4.6.

The variation in absolute spectroscopic factors from the choice of optical-model parameters in DWBA calculations was discussed in Section 4.5.2. For the ground state, a weighted standard deviation of ±23% as a ratio of the weighted average was found, where statistical uncertainties from fits of cross sections to DWBA calculations were used as weights. This is the largest contributor to the overall uncertainty in spectroscopic factors.

Considering these contributions, uncertainties of 25–30% can be expected in the absolute values of spectroscopic factors in a single experiment, although the relative values within a particular dataset are generally good to 15–20%.

5.2 Spectroscopic factors of $\nu 2g_{9/2}$ and $\nu 1i_{11/2}$ orbitals along $N = 126$

This section will focus on comparing the current data on ^{213}Rn to existing data for $N = 127$ isotopes ^{209}Pb and ^{211}Po. For consistency, published cross section data are reevaluated using the same DWBA reaction model with optical-model parameters from Reference [96, 97]. Absolute spectroscopic factors were extracted by comparing calculations to cross section data from (d,p) transfer reactions on ^{208}Pb and ^{210}Po. Spectroscopic factors extracted using data from a range of papers are shown in Table 5.1 for the ground state and lowest-lying $\ell = 6$ state in ^{209}Pb. Uncertainties in spectroscopic factors from fits of cross sections to DWBA calculations are smaller than the variation between datasets and have been omitted in

	Spectroscopic Factor		
Beam energy (MeV/u)	Ground state	$\ell = 6$	Reference
4	0.75	0.45	[41]
6	0.67	0.45	[42]
7.5	0.65	0.43	[45]
9.35	0.61	0.42	[46]
10	0.63	0.45	[43]
11	0.58	0.45	[47]
12.4	0.43	0.35	[40]
Average	0.61	0.43	
Standard deviation	0.09	0.03	

Table 5.1: Absolute spectroscopic factors of the ground state and lowest-lying $\ell - 6$ state in ^{209}Pb from different experiments. Spectroscopic factors have been extracted by comparing to DWBA calculations using optical-model parameters from References [96, 97].

the table. Taking an average of all of these values gives 0.61 for the ground state with a standard deviation of 0.09. For the observed lowest-lying $\ell = 6$ state, the average is 0.43 with a standard deviation of 0.03 and these deviations are within normal expectations for spectroscopic factors. For ^{211}Po, spectroscopic factors were extracted using cross section data from Reference [48], where values of 0.7 and 0.45 were found for the ground state and the observed lowest-lying $\ell = 6$ state, respectively. The uncertainty of absolute cross sections was quoted as ∼15% in this study. Given the uncertainties in spectroscopic factors discussed in the previous section, those extracted for ^{209}Pb and ^{211}Po are broadly consistent with the values of 0.77 and 0.64 extracted in ^{213}Rn for the ground state and lowest-lying $\ell = 6$ state. It can also be noted that all of these values are consistent with the quenching level of ∼0.55 with a RMS variation of 0.1 (18%) often observed in studies using the same bound-state parameters in DWBA calculations [63].

The adoption of another commonly used bound state was also investigated using a fixed geometry with $r = 1.25$, $a = 0.65$ and $V = 6.25$ for both Woods-Saxon and spin-orbit components. Conclusions are not significantly altered and the ^{209}Pb data gives a mean spectroscopic factor for the ground state and the lowest-lying $l = 6$ state of 0.66 and 0.76, respectively, with variations of 15% and 10% across datasets. The ^{211}Po dataset yielded spectroscopic factors of 0.81 and 0.75, whilst for ^{213}Rn they are 0.70 and 0.90. Again, this suggests all states carry a significant fraction of single-particle strength.

In conclusion, comparing the numerous studies on ^{209}Pb and the previous study

of ^{211}Po to the current work for ^{213}Rn indicates that the ground state and lowest-lying $\ell = 6$ state carry significant fractions of the full single-particle strength. This is expected at low excitation energies to within typical levels of uncertainties for spectroscopic factors extracted in this way. There has been no observation of fragmentation associated with $\ell = 4$ and $\ell = 6$ strengths that might arise from particle-vibration coupling or other similar effects at low excitation energy. On the assumption that the effects of short-range correlations move the same fraction of strength to similar high excitation energies in each nucleus, as appears to be the case from several studies such as Reference [63], the excitation energies of these two states may be taken as estimates for the effective single-particle states of the $\nu 2g_{9/2}$ and $\nu 1i_{11/2}$ orbitals.

5.2.1 Two-body matrix element calculations

As discussed in Chapter 1, the evolution of single-particle energies in different regions of the nuclear chart has been attributed to changing nucleon-nucleon interactions as nucleons of the other type fill orbitals across an isotopic or isotonic chain. This interpretation can be applied to data along $N = 126$. Although no data exists for proton occupancies in this region, it is expected that, as protons are added outside the $Z = 82$ closed shell, they will predominantly fill the $\pi 1h_{9/2}$ orbital. Observed trends of neutron single-particle energies may then be described by their interaction with these protons. Figure 5.1 shows the difference in binding energies between $\nu 2g_{9/2}$ and $\nu 1i_{11/2}$ orbitals. As discussed in the previous section, the centroid of each orbital has been taken as the lowest-lying state. These are also compared to theoretical calculations in Figure 5.1. Monopole matrix elements have been calculated for two-body forces using central and spin-orbit terms, with and without a non-central tensor term. These calculations were performed with the computer code TBINT [135] using the HKT two-body force from Reference [136] and assuming protons only fill the $\pi 1h_{9/2}$ orbital. As $\pi 1h_{9/2}$ is a $j_>$ orbital and $\nu 2g_{9/2}$ and $\nu 1i_{11/2}$ are $j_<$ and $j_>$ orbitals, respectively, the effect of the interaction on neutrons with the increasing occupancy of protons is expected to be attractive for $\nu 2g_{9/2}$ and repulsive for $\nu 1i_{11/2}$. This effect is clear in Figure 5.1. Without the tensor term the prediction is substantially different, and calculations of the energy difference between $\nu 2g_{9/2}$ and $\nu 1i_{11/2}$ orbitals deviate from experimental data predicting that it decreases across the isotonic chain. Although still decreasing with the inclusion of the tensor term, the energy difference decrease has a much lower gradient due to the repulsive interaction between orbitals, and calculations

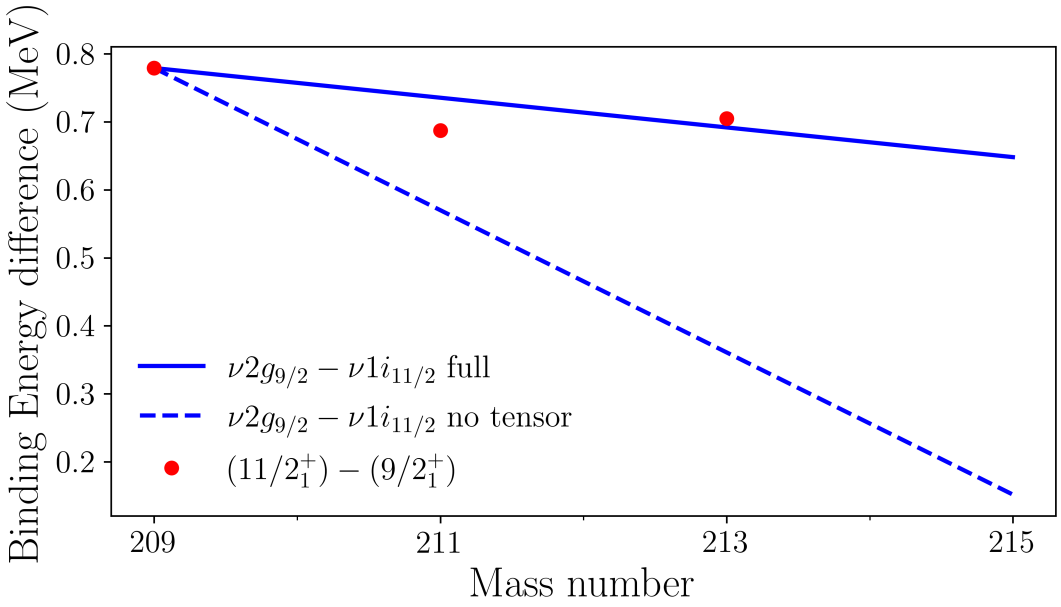


Figure 5.1: Two-body matrix element calculations of the difference of binding energies for $\nu 2g_{9/2}$ and $\nu 1i_{11/2}$ orbitals compared to experimental data across the $N = 127$ isotonic chain. Dashed lines are theoretical predictions using only a central term. Solid lines are calculations with a central and tensor term. Neutron separation energies of 3.9374(13) MeV, 4.5508(5) MeV, 5.108(4) MeV, 5.632(9) MeV for ^{209}Pb, ^{211}Po, ^{213}Rn and ^{215}Ra, respectively, have been used to create this figure and were taken from Reference [122].

are more in line with the experimental data suggesting that it plays an important role in nucleon-nucleon interactions. It should be noted that this interpretation assumes proton only occupy the $\pi 1h_{9/2}$ orbital. This is a reasonable assumption close to the ^{208}Pb double-shell closure, but could potentially be verified in the future using proton transfer reaction experiments.

5.3 Comparison to shell-model calculations

Experimental spectroscopic factors and excitation energies of states in ^{213}Rn have been compared to those predicted using shell-model calculations and are shown in Figure 5.2. Experimental spectroscopic factors and energies of states used in the figure can be found in Table 4.6. Spin assignments for all states are based on comparing experimental angular distributions to DWBA calculations as described in Chapter 4.

Shell-model calculations were performed and obtained from Reference [137] using

the Kuo-Herling interaction. Details of the methodology used for the calculations can be found in References [138].

The shell-model calculations are consistent with the discussion in Section 5.2.1, where the ground state and first-excited state carry significant fractions of $\nu 2g_{9/2}$ and $\nu 1i_{11/2}$ orbital strengths with spectroscopic factors of 0.87 and 0.80 for these states, respectively. However, they also predict smaller fragments at higher energies (see Table 5.2) and this raises the question of how much these fragments would affect the interpretation given in the previous section. In Table 5.2, running excitation energy centroids for $\nu 2g_{9/2}$ and $\nu 1i_{11/2}$ orbitals are presented with contributions from higher-lying states of the same spin and parity with $S \geq 0.01$. As can be seen in the table, the predicted fragments shift the centroids of orbitals by less than ∼150 keV from the centroid calculated using only the strongest state from each orbital. It should be noted that the predicted spectroscopic factors for both sets of fragmented states means that they are very unlikely to be observed and, indeed, are not seen in the current data. The uncertainty in the difference of effective single-particle energies of $\nu 2g_{9/2}$ and $\nu 1i_{11/2}$ orbitals can therefore be taken as $\sim$ 150keV.

The lowest-lying observed $\ell = 2$ state is in good agreement with shell-model calculations and is likely a $J^\pi = 5/2^+$. The strong $J^\pi = 5/2^+$ state at approximately 2 MeV also corresponds to a state assigned as $\ell = 2$ from the experimental data. Shell-model calculations agree somewhat with the two states assigned as either $\ell = 0$ or $\ell = 2$ at ∼1.5 MeV. If these states are close in energy and could not be resolved, their angular distributions may be combinations of $\ell = 0$ and $\ell = 2$. At just over 2 MeV, shell-model calculations roughly agree with experimental data

Orbital	E_x (MeV)	Spectroscopic factor	Running centroid (MeV)
$\nu 2g_{9/2}$	0.00	0.87	0.00
	1.38	0.06	0.09
	1.74	0.01	0.11
	2.071	0.01	0.12
$\nu 1i_{11/2}$	0.68	0.80	0.68
	2.00	0.03	0.72
	2.10	0.01	0.74
	2.17	0.06	0.82

Table 5.2: Excitation energies, spectroscopic factors and excitation energy centroids of states with $S \geq 0.01$ for $\nu 2g_{9/2}$ and $\nu 1i_{11/2}$ orbitals from shell-model calculations. The running centroid in the last column has been calculated using Equation 2.29.

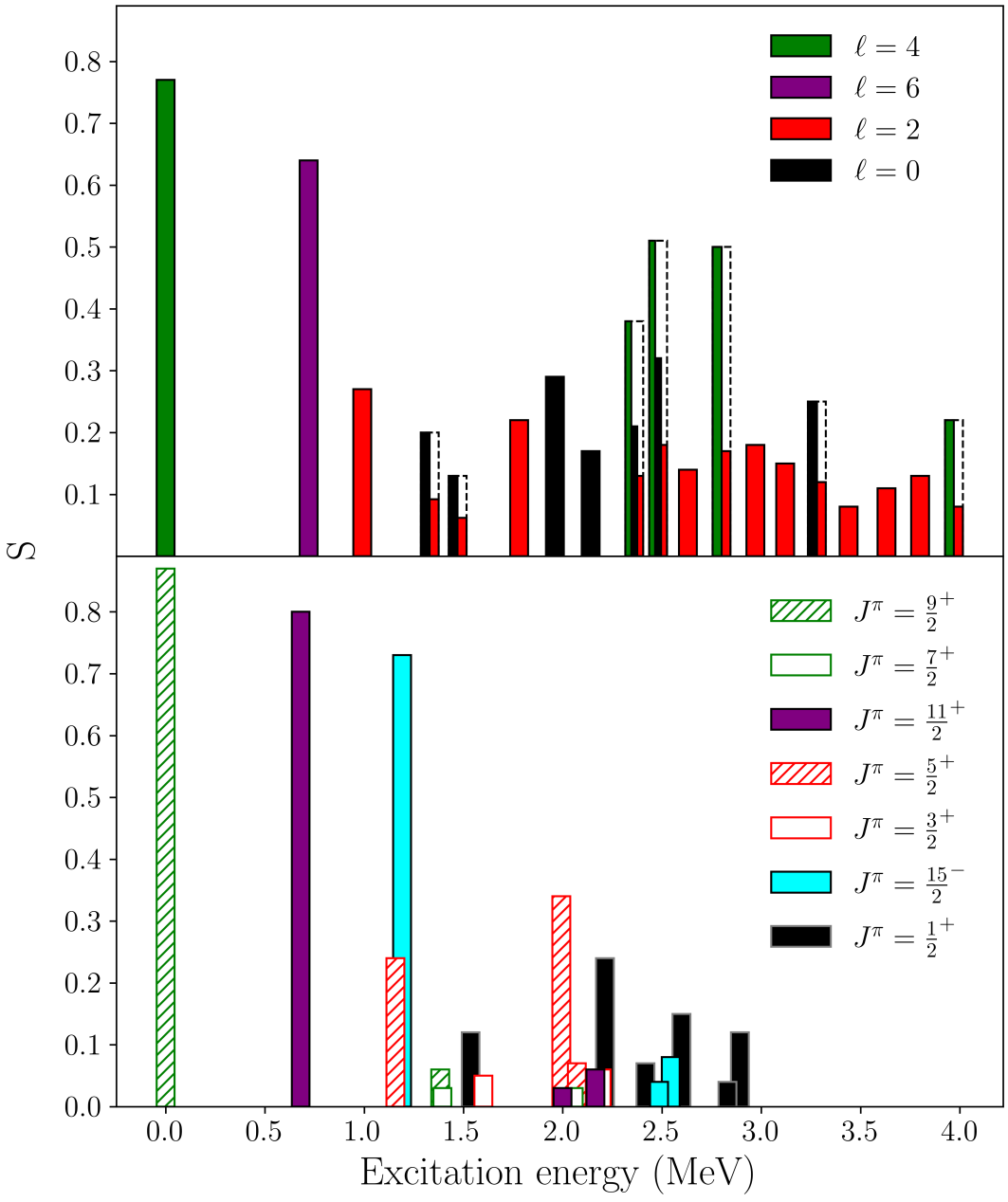


Figure 5.2: The top figure shows experimental spectroscopic factors for states in ^{213}Rn. Dashed bars indicate states that could not be assigned an ℓ transfer. Spectroscopic factors of possible ℓ transfers to these states are shown inside dashed bars. The bottom figure shows spectroscopic factors of states from shell-model calculations for states with $S \geq 0.03$.

for states assigned as $\ell = 0$. However, moving up to 2.5 MeV, more states have multiple possible experimental assignments and a comparison becomes difficult.

At higher excitation energies, the resolution of the data and the increasing level density hinder a detailed comparison between experimental results and calculations. Additionally, no states corresponding to $J^\pi = 15/2^-$ ($\ell = 7$) were observed from these experimental data. This is likely due to low cross sections and insufficient counts being recorded for states associated with this orbital.

To summarise, at excitation energies up to ∼2 MeV, shell-model calculations are in good agreement with experimental data both in describing the spectroscopic strength and energies of states in ^{213}Rn. There are slight differences in excitation energies for some states.

5.4 Future work and outlook

To conclude, a total of nineteen states have been observed in ^{213}Rn using data from the $d(^{212}\mathrm{Rn},p)^{213}\mathrm{Rn}$ reaction at 7.63 MeV/u performed at the ISOLDE facility using ISS. Cross sections were measured and compared to DWBA calculations allowing firm and tentative spin assignments to be made. For some states, multiple possible spin assignments have been suggested due to the similarity of angular distributions. The observed lowest-lying states for $\nu 2g_{9/2}$ and $\nu 1i_{11/2}$ orbitals have been estimated as the effective single-particle energy (ESPE) centroids; and comparing data to two-body matrix element calculations suggests the inclusion of a tensor term is important to reproduce binding energy differences for these orbitals across the $N = 127$ isotonic chain. Experimental data have also been compared to modern shell-model calculations and, in general, a good agreement of spectroscopic strengths and excitation energies have been found for states in ^{213}Rn. This is especially so for states up to ∼2 MeV where most could be firmly assigned an ℓ transfer when comparing experimental cross sections to DWBA calculations.

Extending the monopole-shift interpretation to higher lying, low-ℓ orbitals is difficult. Many of these states are unresolved, and it is not possible to make firm spin assignments to calculate binding energies of these orbitals. Regarding details of the experimental setup, the installation of a blocker device in between the Si array and CD_2 target, as has been done in more recent experiments at ISS, would pre-

vent trajectories of protons undergoing double- and higher-order orbits hitting the on-axis array, reducing unwanted events. This would give access to cross section measurements at larger θ_{cm}, helping with assignments of states that could not be distinguished as shapes of angular distributions diverge above $\theta_{\mathrm{cm}} \approx 40^{\circ}$ at this beam energy. Alternatively, as discussed in Section 3.1.4, performing the experiment at a higher beam energy would lead to less similar angular distributions in the angular range accessible in the experiment, which may also benefit assigning spins to states. Additionally, moving the luminosity detector to a position covering a solid angle region where it detects deuterons with a lower elastic-scattering cross section would have mitigated the effects of pileup in the detector as discussed in Section 4.4.2.

In the future, it would be interesting to extend studies along the $N = 127$ isotonic chain to further understand the evolution of shell structure in this region. An obvious next step is the $d(^{214}\mathrm{Ra},p)^{215}\mathrm{Rn}$ reaction to understand how orbitals evolve and fragment as more protons are added above the $Z = 82$ closed shell. The half-life of ^{214}Ra is 2.46 s and yields of $\sim 10^{7}$ pps/µC have previously been measured at ISOLDE [79] using 0.6 GeV protons from the Proton Synchrotron; lower in energy than the 1.4 GeV protons currently used from the Proton Synchrotron Booster. With a ∼10% efficiency through HIE-ISOLDE, beam intensities at ISS of up to 10^{6} pps can be expected, similar to the beam intensity of ^{212}Rn in this study. Understanding proton occupancies in this region is also important as two-body matrix element calculations were performed assuming protons only filled the $\pi 1h_{9/2}$ orbital. In the future, it may be possible to perform (t,α) experiments on ^{212}Rn with the Si array placed downstream of a tritium target. Extracting proton occupancies would then allow theoretical calculations to be constrained.

Blank page

Appendix A

Table of cross sections

State	E_x (MeV)	θ_{cm} (°)	$\frac{d\sigma}{d\Omega}$ (mb/sr)
1	0	43.87	1.69(11)
		41.98	1.65(7)
		40.04	1.59(7)
		37.95	1.44(7)
		36.04	1.34(7)
		33.99	1.27(6)
		31.78	1.08(8)
		29.19	0.97(10)
		26.64	0.88(10)
		23.71	0.75(8)
		20.06	0.73(8)
2	0.72(5)	41.99	0.11(1)
		39.20	0.11(1)
		35.36	0.07(2)
		30.94	0.06(3)
		25.97	0.07(4)
		19.17	0.09(3)
3	0.99(5)	42.17	1.82(11)
		40.15	1.96(8)
		38.06	1.85(8)
		35.80	1.79(8)
		33.72	1.74(9)

		31.45	1.72(9)
		28.97	1.43(8)
		25.99	1.12(8)
		22.92	0.91(7)
		17.85	0.77(5)
4	1.33(5)	39.46	0.63(5)
		37.32	0.64(6)
		34.99	0.65(13)
		32.83	0.69(7)
		30.48	0.51(8)
		27.87	0.67(11)
		24.71	0.41(12)
		21.36	0.44(6)
		16.88	0.27(6)
5	1.47(5)	39.17	0.51(5)
		37.01	0.38(5)
		34.64	0.35(12)
		32.45	0.35(7)
		30.06	0.45(7)
		27.40	0.50(10)
		24.14	0.27(6)
		20.65	0.23(5)
		16.43	0.26(6)
6	1.78(5)	38.51	1.77(9)
		36.28	1.55(8)
		33.85	1.52(11)
		31.58	1.48(9)
		29.09	1.22(8)
		26.29	1.00(7)
		22.80	0.83(7)
		17.76	0.60(5)
7	1.96(5)	38.11	1.12(7)
		35.85	0.89(7)
		33.37	0.86(9)
		31.05	0.80(8)
		28.49	0.89(7)
		25.61	0.84(8)

		21.96	0.69(6)
		17.23	0.34(5)
8	2.14(5)	37.70	0.51(5)
		35.40	0.55(6)
		32.87	0.55(8)
		30.50	0.54(7)
		27.88	0.48(6)
		24.89	0.50(7)
		21.05	0.38(6)
		16.66	0.16(4)
9	2.36(5)	37.18	0.81(18)
		34.83	0.67(23)
		32.24	1.08(9)
		29.81	0.46(9)
		27.09	0.90(8)
		23.95	0.38(6)
		19.82	0.27(6)
		15.88	0.26(8)
10	2.48(5)	36.89	1.17(17)
		34.51	1.23(17)
		31.89	0.89(10)
		29.41	1.09(10)
		26.64	0.82(8)
		23.42	0.88(8)
		17.87	0.37(13)
11	2.63(5)	36.52	1.17(14)
		34.11	0.98(10)
		31.44	0.73(10)
		28.91	0.79(10)
		26.05	0.51(16)
		22.72	0.50(9)
		17.42	0.37(5)
12	2.80(5)	36.09	1.50(9)
		33.63	1.12(9)
		30.91	1.21(9)
		28.31	1.03(9)
		25.37	0.71(14)

		21.87	0.62(11)
		16.88	0.34(5)
13	2.97(5)	35.65	1.39(10)
		33.15	1.09(10)
		30.36	1.22(9)
		27.69	1.02(10)
		24.64	0.74(10)
		20.96	0.67(8)
		16.28	0.44(6)
14	3.12(5)	35.25	1.12(9)
		32.70	1.00(10)
		29.86	0.84(9)
		27.12	0.88(10)
		23.97	0.54(7)
		20.09	0.60(7)
		15.71	0.40(7)
15	3.28(5)	34.81	0.75(9)
		32.22	0.68(9)
		29.30	0.69(9)
		26.49	0.79(7)
		23.22	0.42(8)
		19.07	0.42(7)
		15.01	0.26(10)
16	3.44(5)	34.36	0.44(8)
		31.71	0.41(8)
		28.73	0.47(6)
		25.83	0.44(6)
		22.42	0.28(8)
		17.43	0.29(6)
17	3.63(5)	33.80	0.66(8)
		31.09	0.54(6)
		28.02	0.60(6)
		25.01	0.51(6)
		21.40	0.39(6)
		18.34	0.43(7)
18	3.80(5)	33.29	0.85(8)

		30.52	0.80(7)
		27.36	0.53(6)
		24.23	0.56(6)
		20.40	0.35(6)
		17.04	0.49(7)
19	3.97(5)	32.76	0.59(7)
		29.92	0.60(7)
		26.67	0.47(6)
		23.41	0.32(6)
		19.31	0.14(3)
		15.48	0.21(6)

Table A.1: Cross sections measured from the $d(^{212}\mathrm{Rn},p)^{213}\mathrm{Rn}$ reaction at 7.63 MeV/u. Statistical uncertainties of cross sections are also given.

Blank page

Bibliography

[1] T. Otsuka, A. Gade, O. Sorlin, T. Suzuki and Y. Utsuno, Rev. Mod. Phys. **92**, 015002 (2020).

[2] M. G. Mayer, Phys. Rev. **74**, 235 (1948).

[3] M. G. Mayer, Phys. Rev. **75**, 1969 (1949).

[4] O. Haxel, J. H. D. Jensen and H. E. Suess, Phys. Rev. **75**, 1766 (1949).

[5] C. A. Bertulani, *Nuclear physics in a nutshell* (Princeton University Press, Princeton, N.J, 2007).

[6] R. D. Woods and D. S. Saxon, Phys. Rev. **95**, 577 (1954).

[7] S. Flügge, *Practical Quantum Mechanics*, Classics in Mathematics (Springer Berlin Heidelberg, Berlin, Heidelberg, 1999).

[8] K. S. Krane, *Introductory nuclear physics* (Wiley, New York, 1988).

[9] K. L. G. Heyde, *Basic ideas and concepts in nuclear physics : an introductory approach*, second edition. ed., Graduate student series in physics (Institute of Physics Pub., Bristol, 1999).

[10] K. L. Heyde, *The Nuclear Shell Model*, 1st ed., Springer Series in Nuclear and Particle Physics (Springer Berlin Heidelberg, Berlin, Heidelberg, 1990).

[11] A. Bohr and B. Mottelson, *Nuclear Structure* (World Scientific, 1998).

[12] R. Liboff, *Introductory Quantum Mechanics* (Holden-Day, 1980).

[13] R. F. Casten, *Nuclear structure from a simple perspective*, 2nd ed., Oxford studies in nuclear physics (Oxford University Press, Oxford, 2000).

[14] P. T. MacGregor, *Single-Particle Structure of 29Mg on the Approach to the N = 20 Island of Inversion* (Springer International Publishing, 2022).

[15] D. K. Sharp, *Trends in single-particle energies in N=51 nuclei*, Ph.D. thesis, The University of Manchester (2012).

[16] T. Otsuka, T. Suzuki, R. Fujimoto, H. Grawe and Y. Akaishi, Phys. Rev. Lett. **95**, 232502 (2005).

[17] J. M. B. Kellogg, I. I. Rabi, N. F. Ramsey and J. R. Zacharias, Phys. Rev. **56**, 728 (1939).

[18] J. M. Blatt and V. F. Weisskopf, *Theoretical nuclear physics* (Wiley, New York, 1952).

[19] A. J. Mitchell, *Investigating high-j single-particle energies in* $Z = 51$ *nuclei*, Ph.D. thesis, The University of Manchester (2012).

[20] A. Ozawa, T. Kobayashi, T. Suzuki, K. Yoshida and I. Tanihata, Phys. Rev. Lett. **84**, 5493 (2000).

[21] C. Hoffman, T. Baumann, D. Bazin, J. Brown, G. Christian, D. Denby, P. DeYoung, J. Finck, N. Frank, J. Hinnefeld *et al.*, Physics Letters B **672**, 17 (2009).

[22] Y. Kondo, T. Nakamura, R. Tanaka, R. Minakata, S. Ogoshi, N. A. Orr, N. L. Achouri, T. Aumann, H. Baba, F. Delaunay *et al.*, Phys. Rev. Lett. **116**, 102503 (2016).

[23] J. S. Randhawa, R. Kanungo, M. Holl, J. D. Holt, P. Navrátil, S. R. Stroberg, G. Hagen, G. R. Jansen, M. Alcorta, C. Andreoiu *et al.*, Phys. Rev. C **99**, 021301 (2019).

[24] A. Huck, G. Klotz, A. Knipper, C. Miehé, C. Richard-Serre, G. Walter, A. Poves, H. L. Ravn and G. Marguier, Phys. Rev. C **31**, 2226 (1985).

[25] A. Gade, R. V. F. Janssens, D. Bazin, R. Broda, B. A. Brown, C. M. Campbell, M. P. Carpenter, J. M. Cook, A. N. Deacon, D.-C. Dinca *et al.*, Phys. Rev. C **74**, 021302 (2006).

[26] D. Steppenbeck, S. Takeuchi, N. Aoi, P. Doornenbal, M. Matsushita, H. Wang, H. Baba, N. Fukuda, S. Go, M. Honma *et al.*, Nature **502**, 207 (2013).

[27] D. Steppenbeck, S. Takeuchi, N. Aoi, P. Doornenbal, M. Matsushita, H. Wang, Y. Utsuno, H. Baba, S. Go, J. Lee *et al.*, Phys. Rev. Lett. **114**, 252501 (2015).

[28] H. N. Liu, A. Obertelli, P. Doornenbal, C. A. Bertulani, G. Hagen, J. D. Holt, G. R. Jansen, T. D. Morris, A. Schwenk, R. Stroberg *et al.*, Phys. Rev. Lett. **122**, 072502 (2019).

[29] B. Bastin, S. Grévy, D. Sohler, O. Sorlin, Z. Dombrádi, N. L. Achouri, J. C. Angélique, F. Azaiez, D. Baiborodin, R. Borcea *et al.*, Phys. Rev. Lett. **99**, 022503 (2007).

[30] T. Motobayashi, Y. Ikeda, K. Ieki, M. Inoue, N. Iwasa, T. Kikuchi, M. Kurokawa, S. Moriya, S. Ogawa, H. Murakami *et al.*, Physics Letters B **346**, 9 (1995).

[31] J. P. Schiffer, S. J. Freeman, J. A. Caggiano, C. Deibel, A. Heinz, C.-L. Jiang, R. Lewis, A. Parikh, P. D. Parker, K. E. Rehm *et al.*, Phys. Rev. Lett. **92**, 162501 (2004).

[32] T. Otsuka, A. Gade, O. Sorlin, T. Suzuki and Y. Utsuno, Rev. Mod. Phys. **92**, 015002 (2020).

[33] S. V. Szwec, D. K. Sharp, B. P. Kay, S. J. Freeman, J. P. Schiffer, P. Adsley, C. Binnersley, N. de Séréville, T. Faestermann, R. F. Garcia Ruiz *et al.*, Phys. Rev. C **104**, 054308 (2021).

[34] B. Kay, S. Freeman, J. Schiffer, J. Clark, C. Deibel, A. Heinz, A. Parikh and C. Wrede, Physics Letters B **658**, 216 (2008).

[35] B. H. Wildenthal, E. Newman and R. L. Auble, Phys. Rev. C **3**, 1199 (1971).

[36] D. K. Sharp, B. P. Kay, J. S. Thomas, S. J. Freeman, J. P. Schiffer, B. B. Back, S. Bedoor, T. Bloxham, J. A. Clark, C. M. Deibel *et al.*, Phys. Rev. C **87**, 014312 (2013).

[37] A. Pfeiffer, G. Mairle, K. Knöpfle, T. Kihm, G. Seegert, P. Grabmayr, G. Wagner, V. Bechtold and L. Friedrich, Nuclear Physics A **455**, 381 (1986).

[38] A. M. Howard, S. J. Freeman, D. K. Sharp, T. Bloxham, J. A. Clark, C. M. Deibel, B. P. Kay, P. D. Parker, J. P. Schiffer and J. S. Thomas, Phys. Rev. C **101**, 034309 (2020).

[39] J. P. Entwisle, B. P. Kay, A. Tamii, S. Adachi, N. Aoi, J. A. Clark, S. J. Freeman, H. Fujita, Y. Fujita, T. Furuno *et al.*, Phys. Rev. C **93**, 064312 (2016).

[40] G. Muehllehner, A. S. Poltorak, W. C. Parkinson and R. H. Bassel, Phys. Rev. **159**, 1039 (1967).

[41] G. Crawley, B. Rao and D. Powell, Nuclear Physics A **112**, 223 (1968).

[42] C. Ellegaard, J. Kantele and P. Vedelsby, Nuclear Physics A **129**, 113 (1969).

[43] A. Jeans, W. Darcey, W. Davies, K. Jones and P. Smith, Nuclear Physics A **128**, 224 (1969).

[44] J. J. van der Merwe and G. Heymann, Zeitschrift für Physik A Hadrons and nuclei **220**, 130 (1969).

[45] R. Casten, E. Cosman, E. Flynn, O. Hansen, P. Keaton, N. Stein and R. Stock, Nuclear Physics A **202**, 161 (1973).

[46] D. Kovar, N. Stein and C. Bockelman, Nuclear Physics A **231**, 266 (1974).

[47] K. Hirota, Y. Aoki, N. Okumura and Y. Tagishi, Nuclear Physics A **628**, 547 (1998).

[48] T. Bhatia, T. Canada, P. Barnes, R. Eisenstein and C. Ellegaard, Nuclear Physics A **314**, 101 (1979).

[49] T. L. Tang, B. P. Kay, C. R. Hoffman, J. P. Schiffer, D. K. Sharp, L. P. Gaffney, S. J. Freeman, M. R. Mumpower, A. Arokiaraj, E. F. Baader *et al.*, Phys. Rev. Lett. **124**, 062502 (2020).

[50] A. Stuchbery, G. Dracoulis, A. Byrne, S. Poletti and A. Poletti, Nuclear Physics A **482**, 692 (1988).

[51] P. Kakker, A. Y. Deo, Z. Podolyák, P. M. Walker, A. Algora, B. Rubio, J. Agramunt, L. M. Fraile, N. Al-Dahan, N. Alkhomashi *et al.*, Phys. Rev. C **94**, 064316 (2016).

[52] G. Satchler, *Introduction to Nuclear Reactions*, 2nd ed. (Macmillan Education UK, London, 1990).

[53] N. K. Glendenning, *Direct nuclear reactions* (World Scientific Publishing Co., River Edge, N.J, 2004).

[54] P. E. Hodgson, Nature **292**, 671 (1981).

[55] W. N. Catford, What can we learn from transfer, and how is best to do it?, in *Lecture Notes in Physics* (Springer Berlin Heidelberg, 2014) p. 67–122.

[56] C. A. Bertulani and P. Danielewicz, *Introduction to nuclear reactions*, second edition. ed., Graduate student series in physics (CRC Press, Boca Raton, 2021).

[57] S. T. Butler, Proceedings of the Royal Society of London. Series A, Mathematical and Physical Sciences **208**, 559 (1951).

[58] M. MacFarlane and S. C. Pieper, *PTOLEMY: a program for heavy-ion direct-reaction calculations* (Argonne National Laboratory, Argonne, IL, 1978).

[59] P. D. Kunz, DWUCK, URL: https://www.oecd-nea.org/tools/abstract/detail/nesc9872/ (Accessed 27/06/2024).

[60] I. Thompson, FRESCO, URL: https://www.fresco.org.uk/ (Accessed 27/06/2024).

[61] M. Igarashi, TWOFNR, URL: https://people.nscl.msu.edu/~brown/reaction-codes/twofnr/twofnr.pdf (Accessed 27/06/2024).

[62] A. Koning and J. Delaroche, Nuclear Physics A **713**, 231 (2003).

[63] B. P. Kay, J. P. Schiffer and S. J. Freeman, Phys. Rev. Lett. **111**, 042502 (2013).

[64] R. B. Wiringa, V. G. J. Stoks and R. Schiavilla, Phys. Rev. C **51**, 38 (1995).

[65] J. P. Schiffer, C. R. Hoffman, B. P. Kay, J. A. Clark, C. M. Deibel, S. J. Freeman, M. Honma, A. M. Howard, A. J. Mitchell, T. Otsuka *et al.*, Phys. Rev. C **87**, 034306 (2013).

[66] B. P. Kay, *High-j Single-particle Strength Outside the Z=50 and N=82 Cores*, Ph.D. thesis, The University of Manchester (2007).

[67] M. H. Macfarlane and J. B. French, Rev. Mod. Phys. **32**, 567 (1960).

[68] J. P. Schiffer, C. R. Hoffman, B. P. Kay, J. A. Clark, C. M. Deibel, S. J. Freeman, A. M. Howard, A. J. Mitchell, P. D. Parker, D. K. Sharp *et al.*, Phys. Rev. Lett. **108**, 022501 (2012).

[69] V. R. Pandharipande, I. Sick and P. K. A. d. Huberts, Rev. Mod. Phys. **69**, 981 (1997).

[70] R. Catherall, W. Andreazza, M. Breitenfeldt, A. Dorsival, G. J. Focker, T. P. Gharsa, T. J. Giles, J.-L. Grenard, F. Locci, P. Martins *et al.*, Journal of Physics G: Nuclear and Particle Physics **44**, 094002 (2017).

[71] A. Gottberg, Nuclear Instruments and Methods in Physics Research Section B: Beam Interactions with Materials and Atoms **376**, 8 (2016).

[72] CERN, ISOLDE, Targets and Separators, URL: `isolde.cern/targets-and-separators` (Accessed 30/10/2023).

[73] J. R. Rumble, ed., *CRC Handbook of Chemistry and Physics*, 104th ed. (CRC Press/Taylor & Francis, Boca Raton, FL, 2023).

[74] L. Penescu, R. Catherall, J. Lettry and T. Stora, Review of Scientific Instruments **81**, 02A906 (2010).

[75] S. Sundell and H. Ravn, Nuclear Instruments and Methods in Physics Research Section B: Beam Interactions with Materials and Atoms **70**, 160 (1992).

[76] E. Kugler, D. Fiander, B. Johnson, H. Haas, A. Przewloka, H. Ravn, D. Simon and K. Zimmer, Nuclear Instruments and Methods in Physics Research Section B: Beam Interactions with Materials and Atoms **70**, 41 (1992).

[77] A. Lavrukhina and A. Pozdnĭakov, *Analytical Chemistry of Technetium, Promethium, Astatine and Francium*, Analytical chemistry of elements (Ann Arbor-Humphrey Science Publishers, 1970).

[78] J. A. Dean and N. A. Lange, *Lange's Handbook of Chemistry*, 15th ed., edited by J. A. Dean (McGraw-Hill, London, 1999).

[79] The ISOLDE Yield Database, Version 0.2, URL: `https://cern.ch/isolde-yields` (Accessed 20/02/2024).

[80] J. Ballof, J. Ramos, A. Molander, K. Johnston, S. Rothe, T. Stora and C. Düllman, Nuclear Instruments and Methods in Physics Research Section B: Beam Interactions with Materials and Atoms **463**, 211 (2020).

[81] F. Ames, J. Cederkäll, T. Sieber and F. J. C. Wenander, *The REX-ISOLDE Facility: Design and Commissioning Report*, CERN Yellow Reports: Monographs (CERN, Geneva, 2005).

[82] M. J. G. Borge and K. Riisager, The European Physical Journal. A, Hadrons and nuclei **52**, 1 (2016).

[83] CERN, ISOLDE, HIE-ISOLDE, URL: https://hie-isolde-project.web.cern.ch/hie-isolde-project/node/35217.html (Accessed 07/12/2023).

[84] O. Forstner, *Beam-Preparation with REXTRAP for the REX-ISOLDE Experiment*, Ph.D. thesis, Vienna, Tech. U. (2001).

[85] P. Schmidt, F. Ames, G. Bollen, O. Forstner, G. Huber, M. Oinonen and J. Zimmer, Nuclear Physics A **701**, 550 (2002), 5th International Conference on Radioactive Nuclear Beams.

[86] F. Ames, G. Bollen, P. Delahaye, O. Forstner, G. Huber, O. Kester, K. Reisinger and P. Schmidt, Nucl. Instrum. Methods Phys. Res., A **538**, 17 (2005).

[87] S. Mataguez, IS689: $^{212}Rn^{50+}$ beam delivered to the ISS experimental ($^{212}Rn^{50+}$ at 7.61 MeV/u), URL: https://edms.cern.ch/document/2683456/1 (Jan 2022).

[88] F. Wenander, B. Jonson, L. Liljeby and G. H. Nyman (REX-ISOLDE), *REXEBIS the Electron Beam Ion Source for the REX-ISOLDE project*, Tech. Rep. (CERN, Geneva, 1998).

[89] F. Wenander, Journal of Instrumentation **5** (10), C10004.

[90] N. Bidault, J. A. Rodriguez, M. Lozano and S. Sadovich, AIP Conference Proceedings **2011**, 070009 (2018).

[91] H. Podlech, M. Grieser, R. von Hahn, S. Papureanu, R. Repnow and D. Schwalm, Nuclear Instruments and Methods in Physics Research Section B: Beam Interactions with Materials and Atoms **139**, 447 (1998).

[92] Y. Kadi, Y. Blumenfeld, W. V. Delsolaro, M. A. Fraser, M. Huyse, A. P. Koufidou, J. A. Rodriguez and F. Wenander, Journal of Physics G: Nuclear and Particle Physics **44**, 084003 (2017).

[93] M. Borge, Nuclear Instruments and Methods in Physics Research Section B: Beam Interactions with Materials and Atoms **47** (2016).

[94] M. Borge and K. Riisager, The European Physical Journal A **52** (2016).

[95] Y. Kadi, Y. Blumenfeld, R. Catherall, W. D. Venturini, M. J. G. Borge, M. Huyse and P. V. Duppen, *Challenges and Goals for Accelerators in the XXI Century* (World Scientific, 2015).

[96] C. M. Perey and F. G. Perey, Phys. Rev. **132**, 755 (1963).

[97] F. G. Perey, Phys. Rev. **131**, 745 (1963).

[98] L. P. Gaffney, *Octupole collectivity in ^{220}Rn and ^{224}Ra*, Ph.D. thesis, The University of Liverpool (2012).

[99] A. M. Baldin, V. I. Goldanskiĭ and I. L. Rozental', *Kinematics of nuclear reactions* (Oxford University Press, Oxford, 1961).

[100] J. Lighthall, *Commissioning of the Helical Orbit Spectrometer: A new device for measuring nuclear reactions in inverse kinematics*, Ph.D. thesis, Western Michigan University (2011).

[101] P. Butler, K. Blaum, T. Davinson, K. Flanagan, S. Freeman, M. Grieser, I. Lazarus, Y. Litvinov, G. Lotay, R. Page *et al.*, Nuclear Instruments and Methods in Physics Research Section B: Beam Interactions with Materials and Atoms **376**, 270 (2016).

[102] G. F. Knoll, *Radiation detection and measurement*, 4th ed. (Wiley, Hoboken, N.J, 2010).

[103] J. M. Ordan, CERN, The ISOLDE Solenoidal Spectrometer (ISS) (2022).

[104] Micron Semiconductor Ltd, S1, URL:https://www.micronsemiconductor.co.uk/multi-element-detectors-double-sided (Accessed 06/07/2024).

[105] D. K. Sharp, Private Communication (2023).

[106] W. Powell, *Development of a Silicon Tracker and Front-end Electronics for R3B*, Ph.D. thesis, The University of Liverpool (2016).

[107] Mesytec, Mesytec MSI-8, URL: https://www.mesytec.com/products/nuclear-physics/MSI-8.html (Accessed 20/07/2024).

[108] CAEN, V1725, URL: https://www.caen.it/products/v1725/ (Accessed 20/07/2024).

[109] M. Febbraro, D. Walter, S. Shadrick, S. Pain, K. Chipps, C. Thornsberry and E. Lesser, Nuclear Instruments and Methods in Physics Research Section B: Beam Interactions with Materials and Atoms **410**, 53 (2017).

[110] L. P. Gaffney, A. Ceulemans, D. J. Clarke, A. Dolan, H. Johansson, B. R. Jones, P. T. MacGregor, S. B. Reeve and H. T. Törnqvist, Isoldesolenoidal-spectrometer/isssort: Isssort v2.4 (2023).

[111] J. Orear, American Journal of Physics **50**, 912 (1982).

[112] Y. Akovali, Nuclear Data Sheets **84**, 1 (1998).

[113] E. Browne and J. Tuli, Nuclear Data Sheets **122**, 205 (2014).

[114] M. Basunia, Nuclear Data Sheets **107**, 2323 (2006).

[115] B. Singh and E. Browne, Nuclear Data Sheets **109**, 2439 (2008).

[116] J. F. Ziegler, M. Ziegler and J. Biersack, Nuclear Instruments and Methods in Physics Research Section B: Beam Interactions with Materials and Atoms **268**, 1818 (2010), 19th International Conference on Ion Beam Analysis.

[117] W. Lennard, H. Geissel, K. Winterbon, D. Phillips, T. Alexander and J. Forster, Nuclear Instruments and Methods in Physics Research Section A: Accelerators, Spectrometers, Detectors and Associated Equipment **248**, 454 (1986).

[118] P. Bauer and G. Bortels, Nuclear Instruments and Methods in Physics Research Section A: Accelerators, Spectrometers, Detectors and Associated Equipment **299**, 205 (1990).

[119] W. Lennard and G. Massoumi, Nuclear Instruments and Methods in Physics Research Section B: Beam Interactions with Materials and Atoms **48**, 47 (1990).

[120] W. Lennard and K. Winterbon, Nuclear Instruments and Methods in Physics Research Section B: Beam Interactions with Materials and Atoms **24-25**, 1035 (1987).

[121] B. R. Jones, Private Communication (2024).

[122] M. Wang, W. Huang, F. Kondev, G. Audi and S. Naimi, Chinese Physics C **45**, 030003 (2021).

[123] J. Mayer, HDTV, URL: `https://github.com/janmayer/hdtv` (Accessed 05/04/2024).

[124] H. An and C. Cai, Phys. Rev. C **73**, 054605 (2006).

[125] J. Bojowald, H. Machner, H. Nann, W. Oelert, M. Rogge and P. Turek, Phys. Rev. C **38**, 1153 (1988).

[126] W. W. Daehnick, J. D. Childs and Z. Vrcelj, Phys. Rev. C **21**, 2253 (1980).

[127] Y. Han, Y. Shi and Q. Shen, Phys. Rev. C **74**, 044615 (2006).

[128] J. Lohr and W. Haeberli, Nuclear Physics A **232**, 381 (1974).

[129] F. D. Becchetti and G. W. Greenlees, Phys. Rev. **182**, 1190 (1969).

[130] J. J. H. Menet, E. E. Gross, J. J. Malanify and A. Zucker, Phys. Rev. C **4**, 1114 (1971).

[131] R. Varner, W. Thompson, T. McAbee, E. Ludwig and T. Clegg, Physics Reports **201**, 57 (1991).

[132] A. Rohatgi, WebPlotDigitizer, v4 (Accessed 13/09/2024).

[133] J. P. Schiffer, C. R. Hoffman, B. P. Kay, J. A. Clark, C. M. Deibel, S. J. Freeman, A. M. Howard, A. J. Mitchell, P. D. Parker, D. K. Sharp *et al.*, Phys. Rev. Lett. **108**, 022501 (2012).

[134] D. K. Sharp, B. P. Kay, J. S. Thomas, S. J. Freeman, J. P. Schiffer, B. B. Back, S. Bedoor, T. Bloxham, J. A. Clark, C. M. Deibel *et al.*, Phys. Rev. C **87**, 014312 (2013).

[135] A. Etchegoyen, M. Etchegoyen and E. Vergini, Computer Physics Communications **55**, 227 (1989).

[136] A. Hosaka, K.-I. Kubo and H. Toki, Nuclear Physics A **444**, 76 (1985).

[137] B. A. Brown, Private Communication (2020).

[138] E. K. Warburton and B. A. Brown, Phys. Rev. C **43**, 602 (1991).